Study of the lattice Boltzmann method application to cerebral aneurysm segmentation

Yan Wang

Année 2014

THÈSE

présentée devant

L'Institut National des Sciences Appliquées de Lyon

pour obtenir

LE GRADE DE DOCTEUR

ÉCOLE DOCTORALE: ÉLECTRONIQUE, ÉLECTROTECHNIQUE, AUTOMATIQUE
FORMATION DOCTORALE: SCIENCES DE L'INFORMATION, DES DISPOSITIFS ET DES SYSTÈMES

par

WANG Yan

Etude de la méthode de Boltzmann sur réseau pour la segmentation d'anévrismes cérébraux

Study of the lattice Boltzmann method application to cerebral aneurysm segmentation

Soutenue le 25 Juillet 2014

Jury :

Bastien CHOPARD	Professeur associé Université de Genève	Rapporteur
Jean-Philippe THIRAN	Professeur associé EPFL	Rapporteur
Alain BONAFE	Professeur CHU Montpellier	Examinateur
Patrick CLARYSSE	Directeur de Recherche CNRS	Examinateur
Thierry FOURNEL	Professeur d'Université UJM	Examinateur
Guy COURBEBAISSE	Ingénieur de Recherche HDR INSA Lyon	Directeur de thèse
Yue-Min ZHU	Directeur de Recherche CNRS	Co-directeur de thèse
Laurent NAVARRO	Chargé de Recherche ENSM-SE	Co-directeur de thèse

INSA Direction de la Recherche

SIGLE	ECOLE DOCTORALE	NOM ET COORDONNEES DU RESPONSABLE
CHIMIE	**CHIMIE DE LYON** **http://www.edchimie-lyon.fr** Insa : R. GOURDON	M. Jean Marc LANCELIN Université de Lyon – Collège Doctoral Bât ESCPE 43 bd du 11 novembre 1918 69622 VILLEURBANNE Cedex Tél : 04.72.43 13 95 directeur@edchimie-lyon.fr
E.E.A.	**ELECTRONIQUE, ELECTROTECHNIQUE, AUTOMATIQUE** **http://edeea.ec-lyon.fr** Secrétariat : M.C. HAVGOUDOUKIAN eea@ec-lyon.fr	M. Gérard SCORLETTI Ecole Centrale de Lyon 36 avenue Guy de Collongue 69134 ECULLY Tél : 04.72.18 60 97 Fax : 04 78 43 37 17 Gerard.scorletti@ec-lyon.fr
E2M2	**EVOLUTION, ECOSYSTEME, MICROBIOLOGIE, MODELISATION** **http://e2m2.universite-lyon.fr** Insa : H. CHARLES	Mme Gudrun BORNETTE CNRS UMR 5023 LEHNA Université Claude Bernard Lyon 1 Bât Forel 43 bd du 11 novembre 1918 69622 VILLEURBANNE Cédex Tél : 04.72.43.12.94 e2m2@biomserv.univ-lyon1.fr
EDISS	**INTERDISCIPLINAIRE SCIENCES-SANTE** **http://ww2.ibcp.fr/ediss** Sec : Safia AIT CHALAL Insa : M. LAGARDE	M. Didier REVEL Hôpital Louis Pradel Bâtiment Central 28 Avenue Doyen Lépine 69677 BRON Tél : 04.72.68 49 09 Fax : 04 72 35 49 16 Didier.revel@creatis.uni-lyon1.fr
INFOMATHS	**INFORMATIQUE ET MATHEMATIQUES** **http://infomaths.univ-lyon1.fr**	M. Johannes KELLENDONK Université Claude Bernard Lyon 1 INFOMATHS Bâtiment Braconnier 43 bd du 11 novembre 1918 69622 VILLEURBANNE Cedex Tél : 04.72. 44.82.94 Fax 04 72 43 16 87 infomaths@univ-lyon1.fr
Matériaux	**MATERIAUX DE LYON** Secrétariat : M. LABOUNE PM : 71.70 –Fax : 87.12 Bat. Saint Exupéry **Ed.materiaux@insa-lyon.fr**	M. Jean-Yves BUFFIERE INSA de Lyon MATEIS Bâtiment Saint Exupéry 7 avenue Jean Capelle 69621 VILLEURBANNE Cédex Tél : 04.72.43 83 18 Fax 04 72 43 85 28 Jean-yves.buffiere@insa-lyon.fr
MEGA	**MECANIQUE, ENERGETIQUE, GENIE CIVIL, ACOUSTIQUE** Secrétariat : M. LABOUNE PM : 71.70 –Fax : 87.12 Bat. Saint Exupéry **mega@insa-lyon.fr**	M. Philippe BOISSE INSA de Lyon Laboratoire LAMCOS Bâtiment Jacquard 25 bis avenue Jean Capelle 69621 VILLEURBANNE Cedex Tél :04.72.43.71.70 Fax : 04 72 43 72 37 Philippe.boisse@insa-lyon.fr
ScSo	**ScSo*** M. OBADIA Lionel Sec : Viviane POLSINELLI Insa : J.Y. TOUSSAINT	M. OBADIA Lionel Université Lyon 2 86 rue Pasteur 69365 LYON Cedex 07 Tél : 04.78.69.72.76 Fax : 04.37.28.04.48 Lionel.Obadia@univ-lyon2.fr

Abstract:

Cerebral aneurysm is a fragile area on the wall of a blood vessel in the brain, which can rupture and cause major bleeding and cerebrovascular accidents. The segmentation of cerebral aneurysm is a primordial step for diagnosis assistance, treatment and surgery planning. Unfortunately, manual segmentation is still an important part in clinical angiography but has become a burden given the huge amount of data generated by medical imaging systems. Automatic image segmentation techniques provides an essential way to simplify and speed up clinical examinations, reduce the amount of manual interaction and lower inter operator variability.

The main purpose of this PhD work is to develop automatic methods for cerebral aneurysm segmentation and measurement. The present work consists of three main parts. The first part deals with giant aneurysm segmentation containing lumen and thrombus. The methodology consists of first extracting the lumen and thrombus using a two-step procedure based on the LBM, and then refining the shape of the thrombus using level set technique. In this part the proposed method is also compared with manual segmentation, demonstrating its good segmentation accuracy. The second part concerns a LBM approach to vessel segmentation in 2D+t images and to cerebral aneurysm segmentation in 3D medical images through introducing a LBM D3Q27 model, which allows achieving a good segmentation and high robustness to noise. The last part investigates a true 4D segmentation model by considering the 3D+t data as a 4D hypervolume and using a D4Q81 lattice in LBM where time is considered in the same manner as for other three dimensions for the definition of particle moving directions in the LBM model.

Keywords: thrombus segmentation, lattice Boltzmann method, aneurysm segmentation, movement detection, 4-D segmentation.

Résumé:

L'anévrisme cérébral est une région fragile de la paroi d'un vaisseau sanguin dans le cerveau, qui peut se rompre et provoquer des saignements importants et des accidents vasculaires cérébraux. La segmentation de l'anévrisme cérébral est une étape primordiale pour l'aide au diagnostic, le traitement et la planification chirurgicale. Malheureusement, la segmentation manuelle prend encore une part importante dans l'angiographie clinique et elle est devenue couteuse en temps de traitement étant donné la gigantesque quantité de données générées par les systèmes d'imagerie médicale. Les méthodes de segmentation automatique d'image constituent un moyen essentiel pour faciliter et accélérer l'examen clinique et pour réduire l'interaction manuelle et la variabilité inter-opérateurs.

L'objectif principal de ce travail de thèse est de développer des méthodes automatiques pour la segmentation et la mesure des anévrismes. Le présent travail de thèse est constitué de trois parties principales. La première partie concerne la segmentation des anévrismes géants qui contiennent à la fois la lumière et le thrombus. La méthode consiste d'abord à extraire la lumière et le thrombus en utilisant une procédure en deux étapes, puis à affiner la forme du thrombus à l'aide de la méthode des courbes de niveaux. Dans cette partie, la méthode proposée est également comparée à la segmentation manuelle, démontrant sa bonne précision. La deuxième partie concerne une approche LBM pour la segmentation des vaisseaux dans des images 2D+t et de l'anévrisme cérébral dans les images en 3D. La dernière partie étudie un modèle de segmentation 4D en considérant les images 3D+t comme un hypervolume 4D et en utilisant un réseau LBM D4Q81, dans lequel le temps est considéré de la même manière que les trois autres dimensions pour la définition des directions de mouvement des particules dans la LBM, considérant les données 3D+t comme un hypervolume 4D et en utilisant un réseau LBM D4Q81. Des expériences sont réalisées sur des images synthétiques d'hypercube 4D et d'hypersphere 4D. La valeur de Dice sur l'image de l'hypercube avec et sans bruit montre que la méthode proposée est prometteuse pour la segmentation 4D et le débruitage.

Mots clé: segmentation du thrombus, méthode de Boltzmann sur réseau, anévrisme cérébral, détection du mouvement, segmentation 4D.

Contents

List of Figures

List of Tables

Synthèse

Introduction

Un anévrisme est un point faible de la paroi d'un vaisseau sanguin dans le cerveau, qui peut se rompre et provoquer des saignements importants et des accidents vasculaires cérébraux. La segmentation de l'anévrisme cérébral est importante pour l'aide au diagnostic et le traitement. Développer des méthodes automatiques pour la segmentation d'anévrismes cérébraux est l'objectif principal de cette thèse.

La méthode de Boltzmann sur réseau a été utilisée pour des simulations en hydrodynamique. Mais, dans cette thèse la stratégie mise en oeuvre consiste a adapter cette méthode pour l'élaboration d'algorithmes de traitement d'image. Nous proposons une série de modèles de segmentation basée sur l'utilisation de la méthode de Boltzmann sur réseau. En plus, les applications à la segmentation d'anévrisme sont présentées.

La première partie de cette thèse présente la problématique médicale et aborde la forme des anévrismes, l'imagerie des anévrismes et les résultats de la segmentation d'anévrismes sur les méthodes existantes.

La deuxième partie de cette thèse introduit brièvement la méthode de Boltzmann sur réseau et son utilisation pour la segmentation 2D, 3D et 4D.

La troisième partie rassemble les conclusions et les perspectives.

Contexte

Anévrisme cérébral

Un anévrisme est un point faible de la paroi d'un vaisseau sanguin, plus couramment d'une artère. La pression sanguine tend à pousser la section affaiblie d'une paroi artérielle vers l'extérieur, formant une saillie similaire à un ballon. Les anévrismes peuvent se former à différents endroits. Les types les plus courants d'anévrismes sont l'anévrisme de l'aorte abdominale, l'anévrisme cérébral et l'anévrisme de l'aorte thoracique.

Les anévrismes cérébraux sont classés à la fois par rapport à leur taille et à leur forme. Les petits anévrismes ont un diamètre inférieur à 15 mm. Les plus grands anévrismes sont classés comme grand (15 à 25mm), géant (25 à 50mm), et super géant (plus de 50mm). Pour les petits anévrismes, seule la lumière est présente. En revanche, les anévrismes géants sont formés d'une lumière et d'un thrombus (Figure 1).

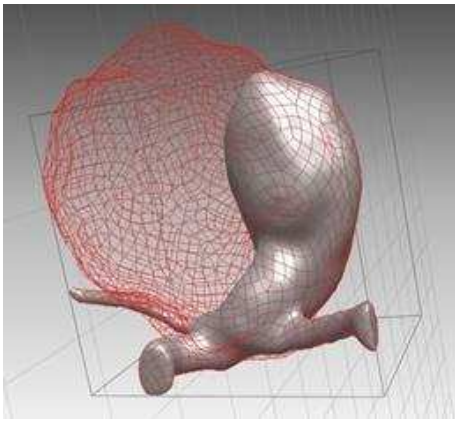

FIGURE 1: Lumière (en gris) et thrombus (en rouge).

Les anévrismes cérébraux se produisent habituellement dans les bifurcations et les branches des grandes artères situées dans le cercle de Willis. Environ 85% des anévrismes se développent dans la partie antérieure du cercle de Willis, et impliquent les artères carotides internes et leurs branches principales qui alimentent la partie antérieure et les sections centrales du cerveau. Sur le cercle de Willis, les sites les plus communs comprennent: l'artère communicante antérieure, l'artère carotide interne, l'artère communicante postérieure, l'artère cérébrale moyenne, l'artère basilaire et l'artère cérébrale postérieure.

Causes, rupture et traitement de l'anévrisme cérébral

Actuellement, la cause des anévrismes cérébraux n'est pas clairement définie. La formation de l'anévrisme cérébral sacculaire a été associée à deux facteurs essentiellement: une anomalie dégénérative (décomposition) de changement dans la paroi d'une artère, et les effets de la pression des pulsations de sang pompé vers l'avant à travers les artères dans le cerveau. A certains endroits d'un anévrisme il peut se créer une plus grande pression sur la paroi, comme lors d'une bifurcation (où l'artère se divise). La formation d'un anévrisme cérébral est également liée à des facteurs de risque qui sont hérités, ou peut se développer plus tard dans la vie.

La première conséquence d'un anévrisme cérébral peut être une hémorragie méningée (HSA), due à la rupture de l'anévrisme. Les ruptures d'anévrismes cérébraux sont mortelles dans environ 40% des cas. Parmi les personnes qui survivent, environ 66% souffrent par la suite d'un déficit neurologique permanent.

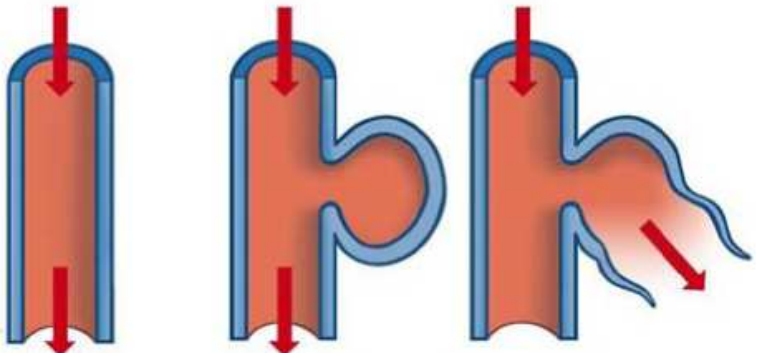

FIGURE 2: De gauche à droite: artère saine, artère présentant un anévrisme, rupture de l'anévrisme.

De nombreux facteurs sont pris en compte lors des décisions de traitement d'un anévrisme cérébral. La taille et la localisation de l'anévrisme sont très importantes. Ensuite, la présence ou l'absence de symptômes, l'âge du patient et son état de santé, et la présence ou l'absence d'autres facteurs de risque pour une rupture d'anévrisme sont pris en compte. Dans certains cas, l'anévrisme ne peut pas être traité, mais le patient sera suivi de près par un médecin. Dans d'autres cas, le traitement chirurgical peut être indiqué.

Pour déterminer les cas, il faut connaître la taille et le ratio dôme-collet de l'anévrisme. Ceci implique d'effectuer une mesure quantitative. Pour traiter un

anévrisme il existe deux stratégie, l'une chirurgicale et l'autre par traitement endovasculaire:

1) Une craniotomie: cette procédure implique l'ablation chirurgicale d'une partie du crâne. Le médecin expose l'anévrisme et met un clip en métal à travers le collet de l'anévrisme pour empêcher l'écoulement du sang dans le sac anévrismal. Une fois le découpage terminé, le crâne est suturé.

2) Enroulement endovasculaire ou embolisation par coils: c'est une technique mini-invasive, ce qui signifie qu'une incision dans le crâne n'est pas nécessaire pour traiter l'anévrisme cérébral. A la place, un cathéter est introduit par un vaisseau sanguin situé à l'aine jusque dans les vaisseaux sanguins situés dans le cerveau et le coil y est déposé. L'anévrisme coagule ensuite (embolisation), ce qui prévient la rupture. Cette procédure est réalisée sous anesthésie générale ou locale.

3) Stent: un cathéter est introduit de la même façon que dans le cas du traitement par coils. Le cathéter en place, le stent est acheminé à travers le cathéter dans l'anévrisme. Dans ce cas, le stent change la pression dans le cerveau et l'anévrisme peut thromboser ou se résorber.

FIGURE 3: Traitment chirurgical par stent.

Imagerie de l'anévrisme cérébral

L'imagerie angiographique par résonance magnétique (ARM) et l'angioscanner permettent de mettre en évidence des anomalies des vaisseaux comme les anévrismes cérébraux.

Angioscanner

L'angioscanner est un test radiologique qui combine la technologie d'un scanner conventionnel avec l'angiographie traditionnelle pour créer des images détaillées de l'intérieur du corps. Il présente quelques avantages :

1) L'angioscanner est capable de détecter un rétrécissement ou une obstruction des vaisseaux sanguins dans un temps très court. Le procédé permet de détecter les plus infimes changements dans la structure du vaisseau et de l'anatomie.

2) L'angioscanner peut donner des détails anatomiques plus précis que l'échographie ou l'IRM, en particulier pour les petits vaisseaux sanguins. Il est en passe de devenir le test radiologique de premier choix pour diagnostiquer des maladies des vaisseaux sanguins.

Mais, en raison de l'utilisation d'un produit de contraste contenant de l'iode, il existe un risque de réaction allergique qui peut être grave. Pour les personnes souffrant de dysfonction rénale, les femmes enceintes et les personnes qui présentent un surpoids, il y a également un risque.

Le diagnostic des anévrismes cérébraux est réalisé à l'aide de l'angiographie classique et de l'angiographie par résonance magnétique. Cependant, les progrès récents de la technologie de l'angiographie par tomodensitométrie fournissent maintenant une modalité alternative pour le diagnostic de la plupart des anévrismes.

De plus, comme l'angioscanner fournit des images plus détaillées, et il peut être utilisé pour examiner presque tous les vaisseaux sanguins dans le corps et plus particulièrement il peut donner une excellente vue du cerveau, de l'abdomen, du coeur, des poumons.

La plupart des images angiographiques d'anévrismes géants présente la particularité de présenter non seulement une lumière (apparaissant en tant qu'objet central), mais aussi un thrombus qui s'apparente à un objet diffus (à faible contraste par rapport aux tissus voisins, ce qui rend leur délimitation manuelle ou automatique difficile) relié à la lumière.

ARM

L'imagerie angiographie par résonance magnétique (ARM) permet de mettre en évidence des anomalies des vaisseaux comme les anévrismes cérébraux. Dans la plupart des cas, un produit de contraste (à base de Gadolinium) est injecté par voie intraveineuse pour améliorer la qualité des images obtenues. Cet examen présente l'avantage de donner des informations très précises. L'ARM peut être employé notamment pour :

1) Évaluer la perméabilité des vaisseaux,

2) Effectuer un bilan de dilatation (anévrisme) ou de rétrécissement de l'aorte thoracique et de ses branches, rechercher des malformations congénitales des vaisseaux.

3) Les structures vasculaires explorées incluent les artères cervicales, l'aorte, les artères digestives, les artères des membres supérieurs et inférieurs et les artères pulmonaires.

Avantages et inconvénients de ces deux types d'imagerie

L'ARM nécessite un champ magnétique puissant et stable produit par un aimant supraconducteur qui crée une magnétisation des tissus par alignement des moments magnétiques de spin. D'excellentes images du cerveau ainsi que de bonnes images des grandes artères peuvent être obtenues. C'est un bon moyen de faire un état de la situation. Ce sont des tests très sûrs car aucun rayonnement n'est utilisé, mais la qualité et le détail des images ne sont pas aussi bons que pour l'angioscanner. En outre, il peut durer jusqu'à 40 minutes et les patients souffrant de claustrophobie ont souvent besoin d'une sédation, car les dimensions de la machine induisent un sentiment de claustrophobie.

Les images d'angioscanner sont créées par injection d'un agent de contraste à base d'iode dans la veine du bras. Lors de son passage dans le cœur, cet agent de contraste est alors pompé vers le cerveau, et l'imagerie scanner est favorisée par l'agent de contraste. Ceci est un test très rapide qui ne prend que quelques minutes à réaliser et la qualité et le détail des images sont excellents. L'inconvénient est qu'il expose le patient à un rayonnement de rayons X et à de l'iode qui, chez certains patients, peut conduire à une réaction allergique. Habituellement, l'angioscanner

est réalisé suite à une ARM si un anévrisme est détecté, afin de recueillir plus d'informations sur ce dernier. Cette information supplémentaire doit permettre aux médecins de prendre la meilleure décision sur le traitement.

La segmentation d'anévrisme par des méthodes existantes

La méthode d'Otsu

Le but de la méthode d'Otsu [Otsu 1975] est la binarisation d'images à niveaux de gris. Ceci revient à séparer les pixels de l'image en deux classes, la première ayant un niveau maximal et la seconde un niveau minimal. La séparation en deux classes est effectuée par calculer l'histogramme.

Dans la méthode d'Otsu, le seuil qui minimise la variance est recherché à partir de tous les seuillages possibles

$$\sigma_{\omega}^{2}(t) = \omega_1(t)\,\sigma_1^2(t) + \omega_2(t)\,\sigma_2^2(t)\,. \tag{1}$$

Les poids ω_i représentent la probabilité d'être dans la i ème classe, chacune étant séparée par un seuil t. σ_i^2 sont les variances de ces classes.

Otsu montre que minimiser la variance intra-classe revient à maximiser la variance inter-classe

$$\sigma_b^2(t) = \sigma^2(t) - \sigma_{\omega}^2(t) = \omega_1(t)\,\omega_2(t)\,[\mu_1(t) - \mu_2(t)]^2 \tag{2}$$

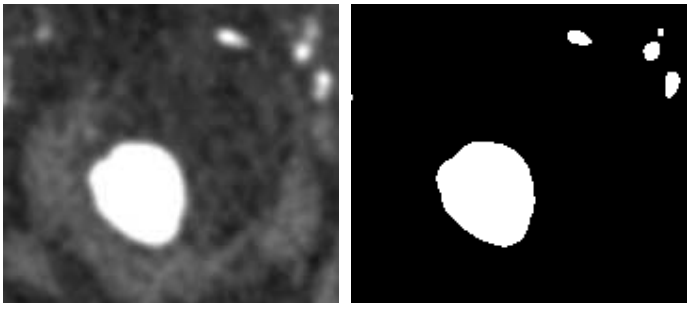

FIGURE 4: L'image originale et le résultat par utiliser la méthode d'Otsu.

Le contour actif géométrique

Dans le but d'utiliser l'évolution de courbes dans la détection d'objets, [Caselles 1997] propose le contour actif géométrique. L'équation d'évolution est

$$\frac{\partial \rho}{\partial t} = \mu \left[\Delta \rho - div \left(\frac{\nabla \rho}{|\nabla \rho|} \right) \right] + \delta(\rho) \left[\lambda div \left(g \frac{\nabla \rho}{|\nabla \rho|} \right) + \nu g \right] \tag{3}$$

où, La fonction ρ est initialement la distance signée au contour et g représente une fonction d'arrêt. Le terme $\nu g \delta(\rho)$ nécessite la sélection du paramètre ν. D'autre part, la courbe s'arrête quand $g = 0$, ce qui correspond à un contour idéal.

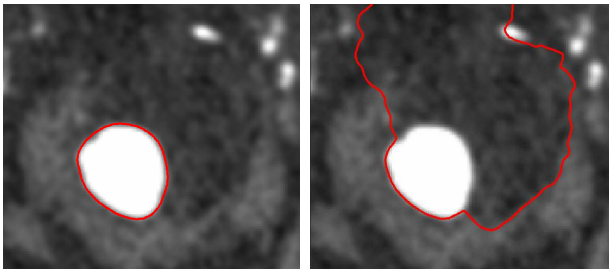

FIGURE 5: Les résultats de la méthode de GAC.

La méthode de "Chan-Vese" (CV)

La méthode de Chan-Vese [Chan 2001] est généralement utilisée pour détecter les contours dans l'image. L'équation d'évolution est

$$\frac{\partial \phi}{\partial t} = \delta(\phi) \left[\mu div \left(\frac{\nabla \phi}{|\nabla \phi|} \right) - \nu - \lambda_1 (I - c_1)^2 + \lambda_2 (I - c_2)^2 \right] \tag{4}$$

C est le contour, avec c1 et c2 les moyennes d'intensité à l'intérieur et à l'extérieur de l'image.

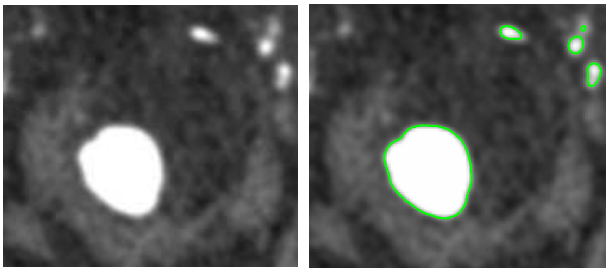

FIGURE 6: Les résultats de la méthode de CV.

Contributions

Les modèles basés sur la méthode de Boltzmann sur réseau

Quand une particule se déplace vers des noeuds voisins, elle peut passer à travers le milieu avec un probabilité g_i. Pour bien utiliser la méthode de Boltzmann sur réseau pour le traitement d'image, une probabilité g_i et un terme de diffusion sont ajouté à l'équation de Boltzmann traditionnelle afin de l'adapter à la segmentation d'image aussi. L'équation d'évolution est

$$\begin{aligned} f_i(\vec{x}+\Delta t\vec{e}_i, t+\Delta t) = {} & g_i(\vec{x})\{f_i(\vec{x},t)+\frac{1}{\tau}[f_i^{eq}(\vec{x},t)-f_i(\vec{x},t)]\} \\ & +[1-g_i(\vec{x})]\{f_i(\vec{x}+\Delta t\vec{e}_i,t) \\ & +\frac{1}{\tau}[f_i^{eq}(\vec{x}+\Delta x\vec{e}_i,t)-f_i(\vec{x}+\Delta t\vec{e}_i,t)]\} \\ & +a\Delta t[\rho(\vec{x})-T] \end{aligned} \tag{5}$$

où f_i est la fonction de distribution d'une particule, f_i^{eq} est la fonction de distribution à l'équilibre locale. τ est le temps de relaxation, x le nœud où se trouve la particule à l'instant t. $a\Delta t[\rho(\vec{x})-T]$ est le terme de diffusion.

L'algorithme de la segmentation d'image est donné
1) Initialisez la fonction de distribution à l'équilibre locale f_i^{eq}.
2) Définissez la valeur f_i: $f_i = f_i^{eq}$.
3) Réglez le maximum de l'itération N.
4) Quand n<N faire 5), ou non faire 9).
5) Collision et propagation pour obtenir un nouvel f_i.
6) Mettre à jour l'état de ρ.
7) Calculer la fonction de distribution à l'équilibre locale.
8) n=n+1 tourner à 4).
9) Fin.

La segmentation en 2D

La segmentation des anévrismes cérébraux géants à partir d'imagerie scanner angiographique reste un problème. Ceci est principalement dû au fait que les anévrismes géants sont constitués de deux parties : la lumière apparaissant comme

un objet focal et le thrombus qui possède un faible contraste par rapport aux tissus voisins et qui rend la segmentation manuelle ou automatique difficile. Nous proposons une méthodologie de segmentation basée sur l'utilisation combinée de la méthode de Boltzmann sur réseau et de la méthode des courbes de niveaux.

La méthodologie consiste d'abord à extraire l'ensemble constitué de la lumière et du thrombus en utilisant une procédure en deux étapes, puis à affiner la forme du thrombus en utilisant la méthode des courbes de niveaux. Plus précisément, nous utilisons la méthode de Boltzmann sur réseau (LBM - Lattice Boltzmann Method) pour la segmentation de la lumière directement à partir de l'image originale. Puis, nous proposons la méthodologie à extraire l'anévrisme qui a été présenté comme un cercle. Après cela, nous utilisons la méthode des courbes de niveaux avec une ellipse comme contour initial pour obtenir le contour de l'anévrisme final.

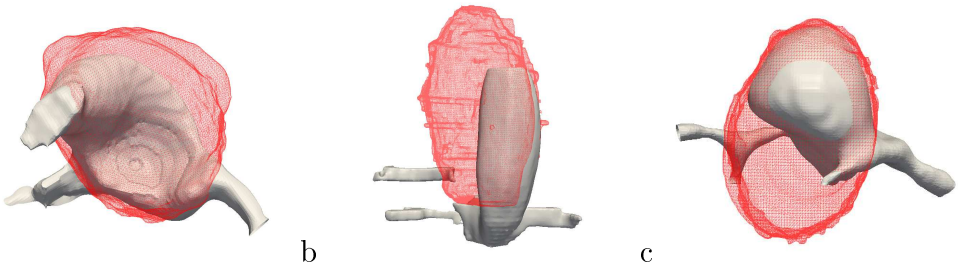

FIGURE 7: Des exemples de visualisation 3D à l'aide de la méthode de segmentation proposée.

La segmentation en 3D

La segmentation automatique des images médicales en 3D reste une tâche difficile en raison du bruit et de l'inhomogénéité dans l'image. Bien que la méthode de Boltzmann sur réseau soit un outil mathématique performant pour résoudre des problèmes de mécanique des fluides, son utilisation pour segmenter des images médicales en 3D est nouvelle et reste un défi. Dans cette section, nous introduisons le modèle LBM D3Q27 pour segmenter les anévrismes 3D et quelque résultats sont donnés Figure 8.

La segmentation en 4D

Des images 4D sous forme de 3D+t deviennent de plus en plus populaires. Des méthodes classiques de segmentation pour ces images 4D consistent souvent en la

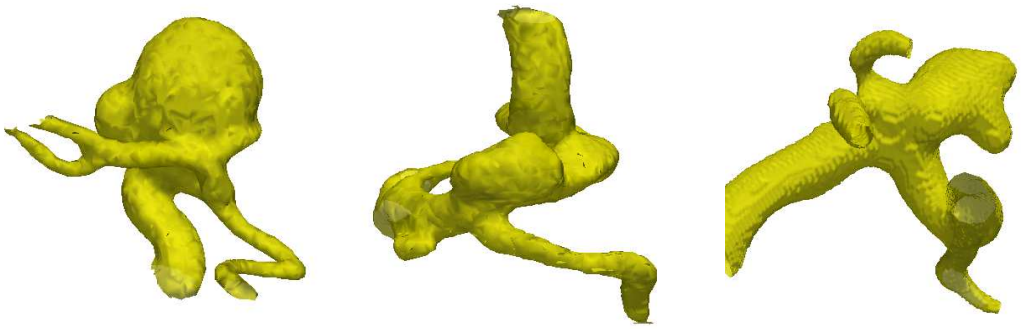

FIGURE 8: Des exemples de visualisation en utilisant la méthode de segmentation 3D proposée.

segmentation d'une série d'images 3D. Nous proposons ici une 'vraie' segmentation 4D en utilisant un réseau LBM D4Q81 et prendrons le temps de même que les trois autres dimensions. La méthode proposée consiste à effectuer la segmentation 4D et l'estimation du mouvement.

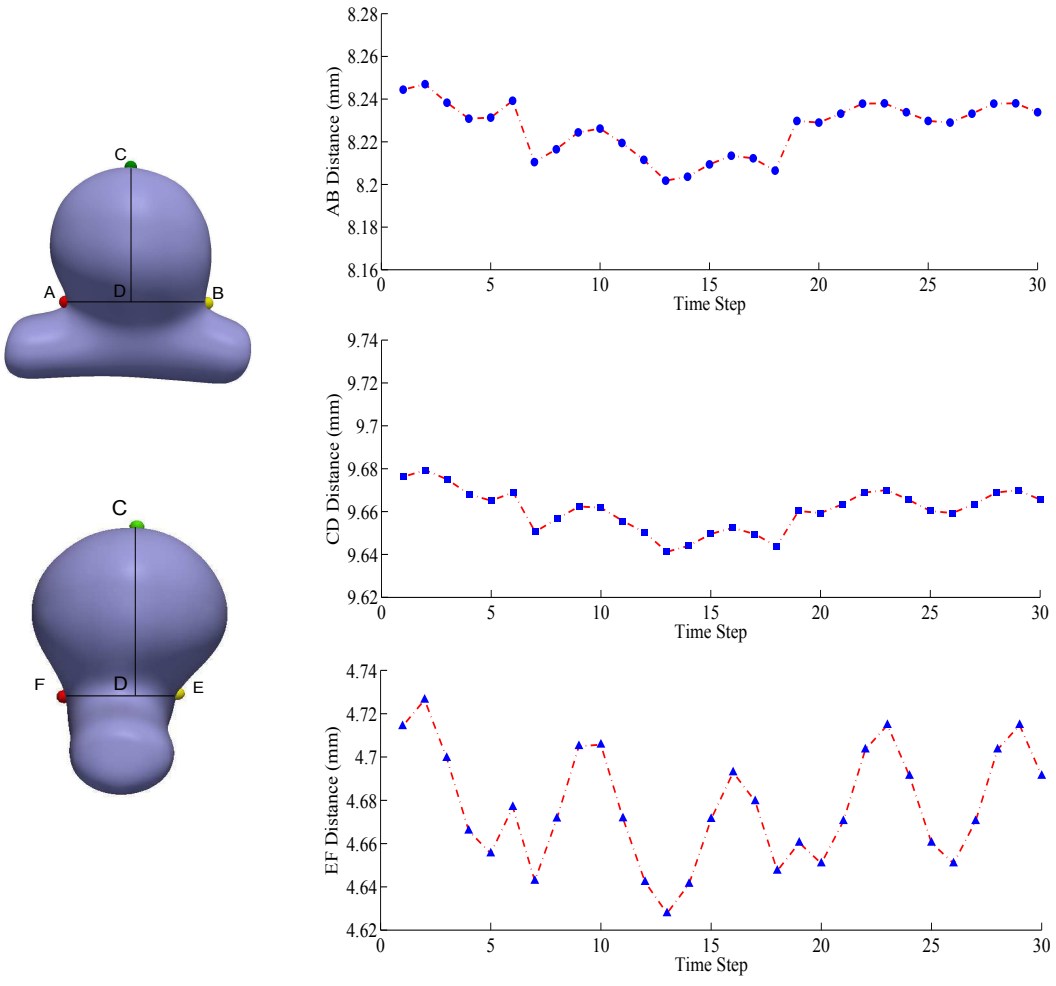

FIGURE 9: Estimation du mouvement d'anévrisme.

Nous souhaitons quantifier le mouvement. Nous avons choisi six points [Oubel 2010] et marqué ces six points comme A, B, C, D, E et F. Pour AB et EF, le mouvement pendant le temps est plus grand que CD. Le mouvement à la direction EF est plus grand que AB dans ce cas (Figure 9).

Conclusions et perspectives

L'étude de la méthode de Boltzmann sur réseau pour la segmentation des images d'anévrismes cérébraux est le but de cette thèse. Les contributions sont:

1) Une série de méthodes de segmentation est proposée basée sur la méthode de Boltzmann sur réseau. Les modèles de D2Q9, D3Q27, D4Q81 ont été utilisés pour la segmentation d'anévrisme.

2) La segmentation des anévrismes géants qui contiennent à la fois la lumière et le thrombus a été présentée.

3) Nous avons étudié les avantages de la description 4D pour la segmentation et proposé un cadre basé sur la méthode de Boltzmann sur réseau 4D pour la segmentation des images d'anévrismes cérébraux.

Dans le futur, il serait intéressant de développer plus profondément le modèle LBM 4D, non seulement pour la segmentation mais aussi pour d'autres opérations de traitement des images 3D+t.

Une autre perspective des méthodes développées dans cette thèse serait d'envisager d'autres techniques de segmentation, couplées à la simulation numérique, étant donné les capacités du modèle LBM dans le domaine des simulations en hydrodynamique.

Introduction

Cerebral aneurysms are formed in approximately 5% people, but most of them are asymptomatic and never detected. The annual rate of brain aneurysm rupture is between 8 to 10 per 100,000 people. There is a cerebral aneurysm rupturing every 18 minutes and the ruptured cerebral aneurysms are fatal in about 40% of cases. Of those who survive, about 66% patients suffer some permanent neurological deficit. Approximately 15% of patients with aneurysmal subarachnoid hemorrhage (SAH) die before reaching the hospital. Most of the deaths from subarachnoid hemorrhage are due to rapid and massive brain injury from the initial bleeding which is not correctable by medical and surgical interventions. 4 out of 7 people who recover from a ruptured brain aneurysm will have disabilities.

In order to study and understand aneurysms, we need to develop better methods for segmentation and analysis. Research in aneurysm segmentation has been studied for more than ten years. [Wilson 1999] established a new automatic algorithm for extracting the 3D vessel information from MRA data. [Hernandez 2007] presented a geometric deformable model and applied it to the segmentation of cerebral aneurysms in RA and CTA. An automated computerized scheme is developed by [Aoyama 2003] for cerebral artery segmentation and diameter measurement of aneurysm from MRA.

There are two major problems. The first problem is that most of aneurysm segmentation methods view the lumen part as the whole aneurysm. However, the segmentation of giant aneurysms is not just the focal lumen part, but also its associated thrombus having irregular and diffuse boundary. The second problem is that a few work takes the time into account in 3D+t sequences and the most commonly used methods are the 2D and 3D methods.

The main objective of this thesis is studying the cerebral aneurysm segmentation in 2D, 3D and 3D+t with lattice Boltzmann method (LBM). The application of LBM

to image processing was reported in the literature. The authors of [Jawerth 1999] firstly applied the LBM to image processing, especially to nonlinear anisotropic diffusion images. In [Zhao 2008], the authors proposed the GPU-accelerated LBM to solve the diffusion [Wolf-Gladrow 1995] lattice problems including volume smoothing, surface fairing, image editing. Also, a LBM for image denoising was mentioned in [Chang 2009]. [Chen 2008] suggested an anisotropic diffusion model based on the LBM to make medical images smooth. A review of nonlinear diffusion filtering can be found in [Y.Chen 2009]. More recently, [Chen 2014] used LBM as a technique to solve GAC equation. In the present study, we adapted the LBM-based anisotropic diffusion model proposed in [Wang 2011] to segment the lumen and the thrombus.

The first part of this thesis presents the context of cerebral aneurysm and general segmentation methods. Also, general LBM method is introduced.

Chapter 1 presents the concept of aneurysm, aneurysm physiology, the basic information of computed tomography angiography (CTA), magnetic resonance angiography (MRA), digital subtraction angiography (DSA) and rotational angiography (RA).

Chapter 2 introduces a state of the art review on the general segmentation methods.

Chapter 3 presents the fundamentals of the general lattice gas automata and LBM.

The second part presents contributions:

In chapter 4, a class of methods using an anisotropic diffusion model based on the LBM for image segmentation is proposed and the parameters corresponding to D2Q9, D3Q27 and D4Q81 models are introduced. Also, tests are performed on synthetic images, such as a 2D circle, a 3D sphere and a 4D hypersphere.

In chapter 5, a segmentation methodology based on the combined use of the LBM and the level set method is proposed. The methodology consists in extracting the group consisting of lumen and thrombus using a procedure in two steps and refining the shape of the thrombus using the level set method.

In chapter 6, the LBM D3Q27 model for segmenting 2D+t vessels images and 3D aneurysm RA and DSA images are introduced.

In chapter 7, a D4Q81 lattice is used in 3D+t aneurysm images and 4D hyper object images.

In the third part, the conclusions and perspectives are presented.

Introduction

Les anévrismes intracrâniens sont présents chez environ 5% des personnes, mais la plupart sont souvent asymptomatiques et ne sont jamais détectés [Rinkel 1998]. Le taux annuel de rupture est d'environ 8 à 10 par 100 000 personnes présentant un anévrisme cérébral. Cela représente une rupture d'anévrisme du cerveau toutes les 18 minutes. Les ruptures d'anévrismes cérébraux sont mortelles dans environ 40% des cas. Parmi les personnes qui survivent, environ 66% souffrent par la suite d'un déficit neurologique permanent.

Environ 15% des patients dont la rupture d'anévrisme déclenche une hémorragie méningée meurent avant d'atteindre l'hôpital. La plupart des décès dus à ces hémorragies font suite à des blessures rapides et massives du cerveau elles-mêmes dues à l'hémorragie initiale qui n'est pas corrigée par intervention médicale et chirurgicale. 4 personnes sur 7 qui se rétablissent d'une rupture d'anévrisme cérébral seront handicapées. Aujourd'hui la segmentation des images d'anévrismes cérébraux est fondamentale pour la mesure quantitative et de l'évaluation des anévrismes. En outre, la segmentation des images d'anévrismes est indispensable au médecin pour sa décision quant au traitement à adopter. L'imagerie par résonance magnétique (IRM) et le scanner conventionnel (CTA) associé à l'angiographie sont les moyens les plus rapides et sûrs pour dépister les anévrismes. Les images obtenus avec ces modalités d'imageie permettent de détecter de manière fiable des anévrismes jusqu'à 2 mm.

Ce constat motive le besoin de développement de meilleures méthodes d'analyse pour étudier et comprendre les anévrismes. La recherche en traitement des images d'anévrisme existe déjà depuis plus de dix ans. [Wilson 1999] ont établi un algorithme entièrement automatique pour segmenter l'information à partir des données IRM. [Hernandez 2007] présentent un algorithme pour la segmentation des structures vasculaires et qui s'applique avec succès à la segmentation des anévrismes

cérébraux dans les images 3DRA et CTA. Un système informatisé automatisé pour la segmentation des artères cérébrales et la mesure du diamètre de l'anévrisme a été développé par [Aoyama 2003].

Cependant, les méthodes mentionnées ci-dessus traitent de la segmentation des anévrismes, considérant la lumière comme faisant partie de l'anévrisme. Ceci pose deux problèmes majeurs. Le premier problème est que les anévrismes géants sont constitués de deux parties, la lumière (non thrombosée) et le thrombus (thrombosé, par définition). Le deuxième problème est que peu de travaux prennent en compte le temps dans les séquences 3D+t et les méthodes les plus utilisées restent les méthodes 2D et 3D.

L'objectif principal de cette thèse est d'étudier la segmentation des images d'anévrismes cérébraux 2D, 3D et 3D+t avec la méthode de Boltzmann sur réseau (LBM). L'application de la méthode de Boltzmann sur réseau au traitement d'image n'est pas nouvelle dans la littératures. Les auteurs de [Jawerth 1999] ont appliqué la LBM au traitement d'image, en particulier à la diffusion anisotrope non linéaire des images. Dans [Zhao 2008], les auteurs ont proposé l'accélération sur GPU de la méthode de Boltzmann sur réseau pour résoudre les problèmes diffusion de réseaux, y compris le lissage de volume, carénage de surface, et retouche d'image. En outre, un débruitage par LBM a été mentionné dans [Chang 2009]. Enfin, [Chen 2008] a suggéré un modèle de diffusion anisotrope sur la base de la LBM pour lisser les images médicales. Des essais de filtrage non linéaire à bas de diffusion peuvent être trouvées dans [Y.Chen 2009]. Plus récemment, [Chen 2014]a utilisé la LBM comme technique pour résoudre l'équation des contours actifs (GAC). En outre, [Wang 2011] a proposé un modèle de diffusion anisotrope basé sur la LBM pour segmenter la lumière et le thrombus de l'anévrisme.

La première partie de cette thèse est la présentation des fondements médicaux de l'imagerie des anévrismes et la méthodologie de notre travail:

Le chapitre 1 présente les principales données concernant les anévrismes, la physiologie de l'anévrisme et décrit les principes de l'imagerie scanner conventionnel couplé à l'angiographie (CTA) et l'imagerie par résonance magnétique (IRM).

Le chapitre 2 résume un état de l'art sur les méthodes existantes de segmentation.

Le chapitre 3 introduit brièvement la méthode de Boltzmann sur réseau.

La seconde partie de ce manuscrit est dédiée aux contributions méthodologiques:

Dans le chapitre 5, la méthode de Boltzmann sur réseau basée sur les niveaux de gris des images 2D est proposée. Une application à la segmentation de la lumière et du thrombus d'un anévrisme intracrânien à l'aide de la LBM est présentée. La méthode consiste d'abord à extraire la lumière et le thrombus en utilisant une procédure en deux étapes basées sur la LBM, puis d'affiner la forme du thrombus en utilisant la méthode des courbes de niveaux.

Dans le chapitre 6, la méthode de Boltzmann sur des réseaux 3D et 4D basée sur les niveaux de gris des images 3D et 3D+t est proposée.

Dans le chapitre 7, Le modèle 4D est utilisé dans la détection de mouvement de la paroi de l'anévrisme.

La troisième partie rassemble les conclusions et les perspectives.

Part I

MEDICAL CONTEXT AND METHODOLOGY

Chapter 1

Context of cerebral aneurysm

Abstract

In order to understand the context of this thesis, the basic information of aneurysms is needed. In this first chapter, we describe briefly the concept of aneurysm and aneurysm physiology. Furthermore, we also introduce the basic information of computed tomography angiography (CTA), magnetic resonance angiography (MRA), digital subtraction angiography (DSA) and rotational angiography (RA).

Résume

Dans le cadre de l'étude des anévrismes, un minimum de connaissances sur ce sujet est nécessaire. Pour comprendre le contexte de cette thèse, nous allons décrire brièvement dans ce premier chapitre le concept d'anévrisme, la physiologie de l'anévrisme et présenter les informations de l'imagerie scanner angiographique, l'angiographie par résonance magnétique, l'angiographie numérique avec soustraction et l'angiographie rotationnelle.

1.1 Cerebral aneurysm

An aneurysm is a weak part of the wall of a blood vessel, which normally occurs at an artery. The blood pressure tends to push the weakened arterial wall section outwardly, forming a projection which is similar to a balloon. Aneurysms can form in different places. The most common types of aneurysms are abdominal aortic aneurysms, cerebral aneurysms and thoracic aortic aneurysms.

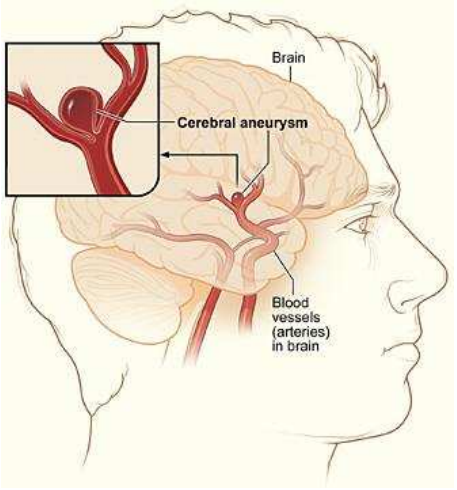

FIGURE 1.1: An example of cerebral aneurysm.

A cerebral aneurysm is a deformation of the membrane of the arteries of the brain as shown in Figure 1.1. The aneurysm is located in an area of the brain that is connected to cerebral arteries. Figure 1.2 is an example for detecting the cerebral aneurysm.

FIGURE 1.2: The medical image for detecting the cerebral aneurysm.

1.2 General formation

Cerebral aneurysms are classified both by their size and their shape. The small aneurysms have a diameter less than 15 mm. Larger aneurysms are classified as large (15 to 25mm), giant (25 to 50mm) and super giant (over 50mm). Normally, the small aneurysms only have the lumen part. However, the giant aneurysms are formed of a lumen and a thrombus (Figure 1.3).

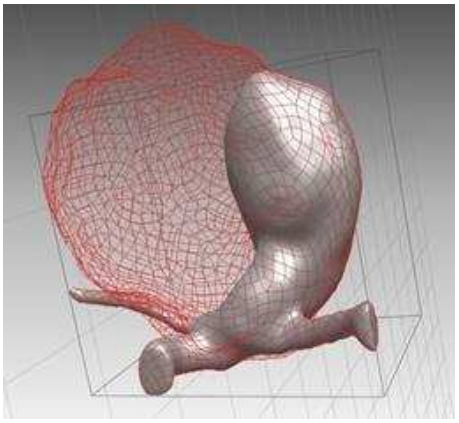

FIGURE 1.3: An example of giant aneurysm of lumen in gray and thrombus in red.

About 85 % cerebral aneurysms occur in branches of large arteries in the circle of Willis. Figure 1.4 is a brain diagram with the circle of Willis marked in red. On the circle of Willis, the most common sites to form aneurysms including:

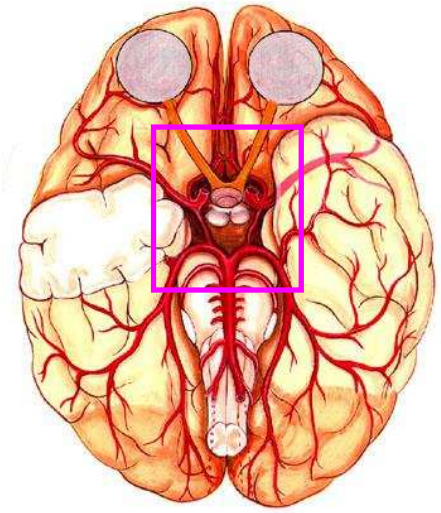

FIGURE 1.4: Format of the circle of Willis.

A: Middle cerebral artery.

B: Anterior cerebral artery.

C: Anterior communicating artery.

D: Anterior cerebral artery.

E: Internal carotid artery.

F: Posterior communicating artery.

G: Basilar artery.

J: Posterior cerebral artery.

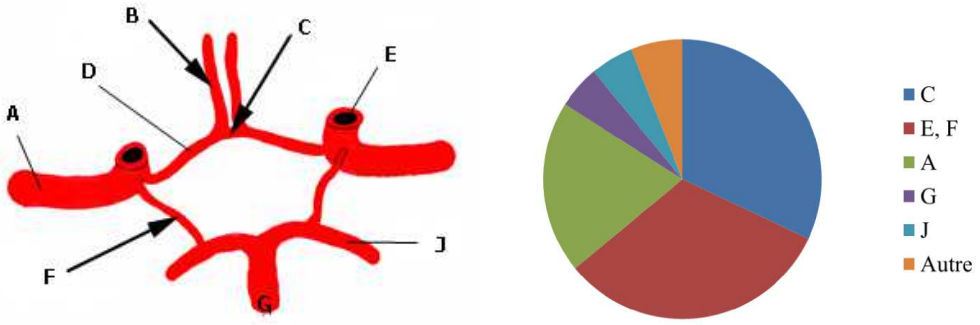

FIGURE 1.5: The common sites of aneurysms in circle of Willis.

1.3 Causes, symptoms and rupture of aneurysms

The causes of cerebral aneurysms are not clearly defined. But as we all know, the formation of cerebral aneurysm is linked to risk factors, which are inherited or can be developed later in life. Risk factors associated with the formation of an aneurysm may include (but are not limited to) the following

1) Smoking.

2) High blood pressure or hypertension.

3) Inborn abnormality in artery wall.

4) Family history of brain aneurysms.

5) Age over 40.

6) Gender, women compared with men have an increased incidence of aneurysms at a ratio of 3:2.

7) Other disorders: Ehlers-Danlos Syndrome, Polycystic Kidney Disease, Marfan Syndrome, and Fibromuscular Dysplasia(FMD).

8) Drug use (particularly cocaine), infection, tumors, traumatic head injury.

Smoking and high blood pressure or hypertension are risk factors, which are normally considered by doctors and researchers in contributing to the rupture of cerebral aneurysms.

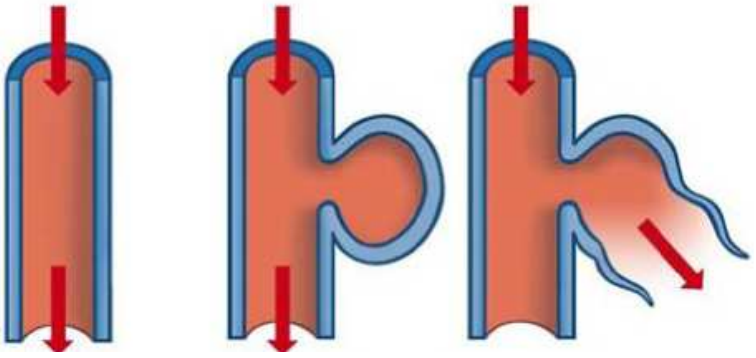

FIGURE 1.6: From left to right: artery, aneurysm, rupture of aneurysm.

The first consequence of the rupture of a cerebral aneurysm is subarachnoid hemorrhage (SAH). Symptoms may include (but are not limited to) the following

1) Headache.

2) Torticollis.

3) Nausea and vomiting.

4) Changes in mental status, such as drowsiness.

5) Pain in specific areas, such as eyes.

6) Dilated pupils.

7) Fainting.

8) Hypertension or high blood pressure.

9) Motor deficits (loss of balance or coordination).

10) Sensitivity to light.

11) Pain in back or leg.

12) Cranial nerve deficits.

1.4 Treatments of cerebral aneurysms

Many factors should be taken in consideration when the patients want to get their aneurysms treated. First, the size and the location of aneurysm are very important. Then, symptoms, age of the patient, health status and other risk factors should be considered. In some cases, the aneurysms can not be treated, but the patients need to be monitored closely by doctors. In other cases, the surgical procedure may be needed. There are three common surgical treatments

1) Craniotomy & clip: this treatment includes the surgical removal of part of the skull. A microscope is used to carefully identify the position of aneurysm and a permanent metallic clip is surgically placed across its neck, securing the aneurysm from further bleeding in the future.

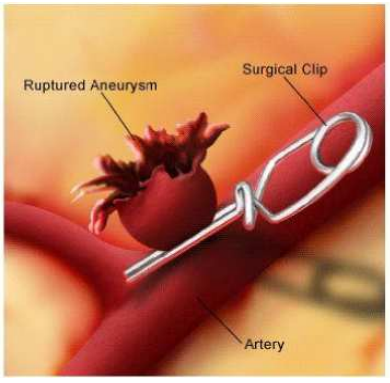

FIGURE 1.7: Surgical treatment by using craniotomy.

2) Coil: it is a minimally invasive technique, which means that craniotomy is not necessary to the treatment. Instead, a catheter is inserted through a blood vessel located in the groin up to the vessels in brain where the coil will be deposited. This procedure is performed under general or local anesthesia.

3) Stent: a catheter is inserted through the blood vessel, which is same as in the case of treatment with coils. When the catheter is in proper position, the stent is

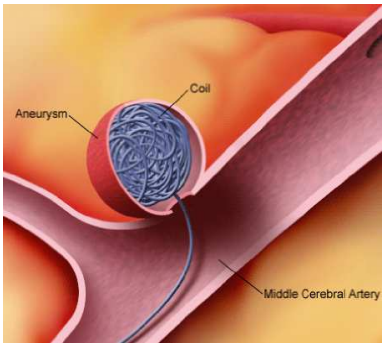

FIGURE 1.8: Surgical treatment by using colis.

delivered through the catheter into the parent artery of the aneurysm. In this case, the stent will change the blood flow pattern in the aneurysm to form thrombosis.

FIGURE 1.9: Surgical treatment by using stent.

1.5 Common medical imaging techniques

1.5.1 Computed tomography angiography

CTA is a radiological test that combines the technology of a conventional CT scan with traditional angiography to create image details of the blood vessels. An iodine-rich contrast material is usually injected through a small catheter placed in a vein of the arm.

With CT scanning, numerous X-ray beams rotate around the person and the examination table is moving through the scanner. A special computer program processes the large volume of data to create two dimensional cross-sectional image of body. When the image slices are reassemble by computer software, the result is a very detailed three dimensional view of the body's interior.

FIGURE 1.10: Computed tomography (CT) equipment.

There are some advantages of CTA, which include

1) CTA is able to detect a narrow or blockage of blood vessels in a very short time. This method allows to detect the smallest changes in the structure and the vessel anatomy.

2) Angiography can provide more precise anatomical details as ultrasound or MRI, especially for small vessels. It becomes a good option for diagnosing diseases of the blood vessels.

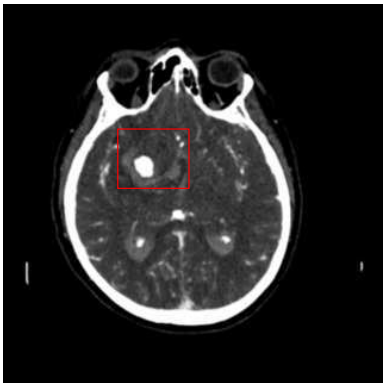

FIGURE 1.11: An example of 2D CTA slice with cerebral aneurysm.

But, due to the use of an material containing iodine, there is a risk of allergic reaction which may be severe. For people with kidney dysfunction, pregnant and overweight, the risk is also considerably big.

1.5.2 Magnetic resonance angiography

The traditional MRI unit is a large clinder-shaped tube surrounded by a circular magnet. Person will lie on a moveable examination table that slides into the center of the magnet. Unlike conventional CT scans, MRI does not depend on ionizing radiation. Instead, while in the magnet, radio waves rediect the axes of spinning protons.

FIGURE 1.12: Magnetic resonance (MR) equipment.

MRA can provide very accurate information and it can be used to

1) Examine the carotid arteries in the neck and the cerebral vessels in the brain.

2) Detect a cerebral aneurysm.

3) Assess vascular malformations.

4) Evaluate some types of headaches.

FIGURE 1.13: An example of MRA image with cerebral aneurysm.

There are some advantages of MRA, which include

1)MRA is a noninvasive imaging technique that does not involve exposure to ionizing radiation.

2) Detailed images of blood vessels and blood flow are obtained without having to insert a catheter into the blood vessels, so that there is no risk of damaging a major blood vessel.

3) Without contrast meterial, MRA can provide high quality images of blood vessels.

MRA are very safe tests as no radiation is used, but the quality and detail of the images are not so good as CTA. In addition, it might take as long as 40 minutes for a patient to complete one of these studies. On the contrary, CTA is a fast test that takes only a few minutes to perform and the quality and detail of the images are excellent. Usually, CTA is reserved as a follow-up study to a MRA study if an aneurysm is detected and there is a need to collect more information on the aneurysm.

1.5.3 Digital subtraction angiography

DSA is a type of fluoroscopy technique used in interventional radiology to clearly visualize blood vessels in a bony or dense soft tissue environment.

FIGURE 1.14: Digital subtraction angiography equipment.

It is useful in the diagnosis and treatment of

1) Arterial and venous occlusions.

2) Arterial stenosis, which is particularly useful for potential renal donors in detecting renal artery stenosis. DSA is the gold standard investigation for renal artery stenosis [Tortora 1976].

3) Cerebral aneurysms and arterio-venous malformations (AVM).

DSA has been the standard of reference for the detection and characterization of cerebral aneurysms [Yoon 2007]. It has several disadvantages, however, including the high skill level of performing the procedure and relatively high cost.

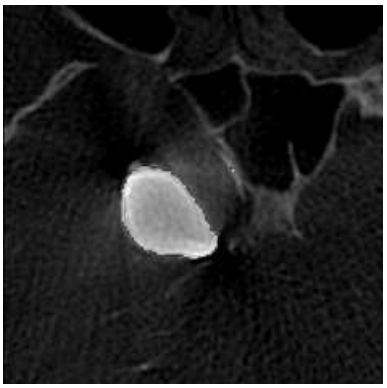

FIGURE 1.15: An example of DSA image with cerebral aneurysm.

1.5.4 Rotational angiography

RA is a medical imaging technique based on x-ray, which allows to acquire CT-like 3D volumes with a fixed C-Arm. The fixed C-Arm thereby rotates around the patient and acquires a series of x-ray images that are then reconstruced through software algorithms into a 3D image.

FIGURE 1.16: Rotational angiography equipment.

It has benefits in the visualization of ventricular systems, soft tissue and bone structures in the interventional suite, the detection of bleeding and unintended blockages of lumen.

Compared with DSA, 3D RA allows more exact depiction of anatomic details that are important in planning surgery and interventional therapy for cerebral aneurysms [Hochmuth 2002].

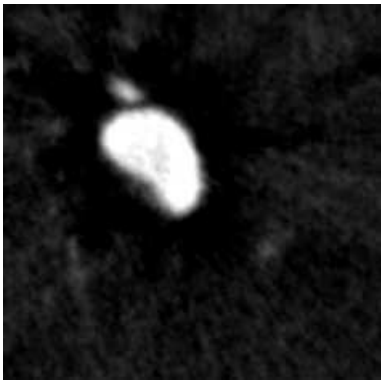

FIGURE 1.17: An example of RA image with cerebral aneurysm.

1.6 Conclusion

General information, such as formation, symptoms and treatments of aneurysms, is given in this chapter. We also introduced the widely used medical imaging techniques, including the advantages and disadvantages of each technique. All those above can provide the context for our following study.

Chapter 2

Context of segmentation method

Abstract

In this chapter, we introduce the general segmentation methods, meanwhile we describe a state of the art review on segmentation algorithms in cerebral aneurysm. The segmentation results obtained by using Ostu method [Otsu 1975], geodesic active contour method (GAC) [Caselles 1997], Chan-Vese method (CV) [Chan 2001] and lattice Boltzmann based GAC method [Chen 2014] are shown in this chapter. Also, advantages and disadvantages for these methods are presented.

Résume

Dans ce chapitre, nous présentons les méthodes de segmentation générales, en parallèle, nous décrivons l'état de art sur les algorithmes de segmentation dans l'anévrisme cérébral. Les résultats de la segmentation en utilisant la méthode d'Ostu, la méthode de contour actif géodésique (CAG), la méthode de Chan-Vese (CV) et la méthode de Boltzmann dédiée CAG ont été présentés dans ce chapitre. En plus, les avantages et les inconvénients des méthodes ont été proposés.

2.1 General segmentation methods

Segmentation is the process of partitioning an image into regions with similar properties such as intensity and texture. The goal of image segmentation is to find regions that represent objects or meaningful parts of objects. Meanwhile, segmentation plays an important role in medical image processing. It can help physicians and neurosurgeons to:

1. Investigate and diagnose.
2. Study of anatomical structure, e.g. cortical or subcortical structures, blood vessels, tumors etc.
3. Identify region of interest or detect abnormalities.
4. Measure growth or decrease in size of tumor.
5. Help in treatment planning prior to radiation therapy.
6. Computer-guided surgery.

By now, a number of algorithms have been proposed in image segmentation, and we divide such methods into eight categories [Pal 1993, Pham 2000, Zhang 2001, Petitjean 2011]: (1) thresholding approaches, (2) region-growing methods, (3) edge-based segmentation methods, (4) partial differential equation based methods, (5) Markov random field models, (6) neural networks segmentation methods, (7) clustering methods, also there are still some notable methods which do not belong to any of these categories.

2.1.1 Thresholding approaches

Thresholding approaches [Sahoo 1988] segment images by creating a binary partitioning of the image intensities. It is particularly suitable for an image with object of uniform brightness placed against a background of different gray level. A threshold is used to segment the object and background, which can be defined as follows:

$$R_{i,j} = \begin{cases} 1 & P_{i,j} \geq T \\ 0 & T_1 < P_{i,j} < T \end{cases} \tag{2.1}$$

where, $R_{i,j}$ is the resulting gray level at coordinate (i, j), $P_{i,j}$ is the gray level of original image at coordinate (i, j), and T is the value of threshold. Figure 2.1 in middle shows the histogram of a CTA (Computed Tomographie Angiographie)

image which we can see in Figure 2.1 in left. The segmentation result is shown in Figure 2.1 in right.

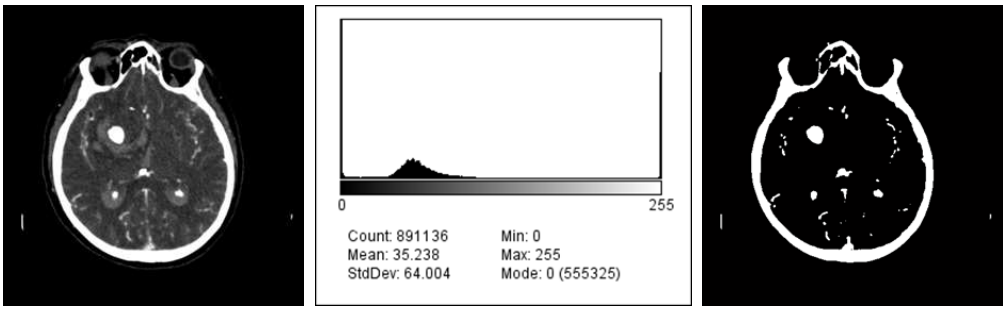

FIGURE 2.1: In left: original cerebral CTA image; in middle: image histogram; in right: result of thresholding method segmentation.

The simple thresholding operation does not work very well at segmentation of images with multiple thresholds. We can see two potential thresholds are shown in Figure 2.1 in middle, one is between 10 and 30, and the other is between 100 and 250. To solve this problem, multiple thresholding operation is applied as follows:

$$R_{i,j} = \begin{cases} 0 & P_{i,j} \leq T_1 \\ 1 & T_1 < P_{i,j} \leq T_2 \\ 2 & T_2 < P_{i,j} \leq T_3 \\ \ldots & \\ k & T_k < P_{i,j} \end{cases} \tag{2.2}$$

For application of thresholding approaches, it is required to use the correct threshold values in order to achieve proper segmentation results.

The major problem with thresholding is that we consider only the intensity, not any relationships between the pixels.

2.1.2 Region-growing methods

The region-growing methods [Hojjatoleslami 1998] take a set of seeds as input along with the image. The regions are iteratively grown by comparing all unallocated neighboring pixels. The difference between a pixel's intensity value and the average of the region is used as a measure of similarity. With the smallest difference the pixel is allocated to respective regions. The process continues until

all pixels are allocated to a region. Results of region-growing methods can be specified by following conditions:

$$R_1 \cup R_2 \cup R_3 \cup ... \cup R_k = I \tag{2.3}$$

$$R_1 \cap R_2 \cap R_3 \cap ... \cap R_k = 0 \tag{2.4}$$

Here, R_1, R_1, R_1...,R_k are the regions in the image .

2.1.3 Edge-based segmentation methods

These kind methods are normally based on image gradients [Caselles 1997]. The approaches which can produce object contours. The algorithm for these kind methods always has the following steps:
1. Apply the derivative operator to detect edges of the image.
2. Measure the strength of edges by measuring amplitude of the gradient.
3. Retain all edges having magnitude greater than threshold T.
4. Find the position of crack edges.
5. Repeat steps 3 and 4 with different values of threshold to find out the closed boundaries and then the segmentation of the image will be achieved.

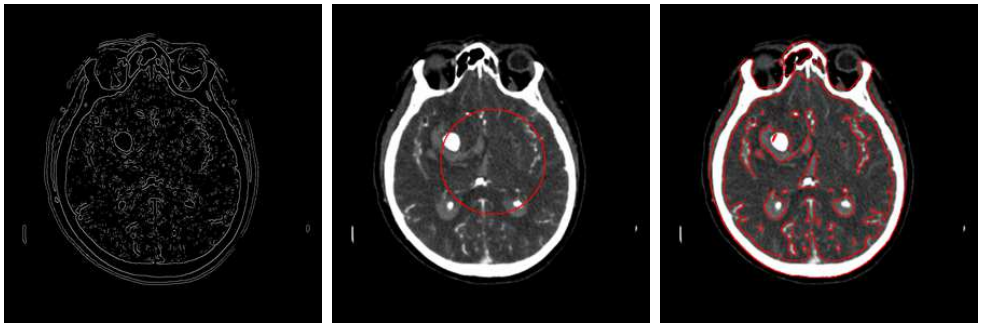

FIGURE 2.2: In left: result of edge based segmentation method; in middle: original image with an initial curve; in right: result of partial differential equation based method.

2.1.4 Partial differential equation based methods

The central idea of partial differential equation based methods is to evolve an initial curve towards to the lowest potential of a cost function, where its definition reflects

the task to be addressed. Mostly, the minimization of the cost functional can be expressed as geometrical constraints on the evolving curve. In this way, using partial differential equation based methods and solving the partial differential equation can segment the image.

The methods include parametric method, level set method, and fast marching method. Figure 2.2 in right shows the result obtained by using a simple level set method and Figure 2.2 in middle shows the original image with an initial curve.

2.1.5 Markov random filed models

There are many image segmentation methods using the spatial interactions models like Markov random filed [Li 1995]. At first, Markov random field has been introduced in the theory of probability. And this model itself is not a segmentation method but a statistical model which can be used within segmentation methods. In medical image processing, they are typically used to take into account the fact that most pixels belong to the same class as their neighboring pixels.

2.1.6 Neural networks segmentation methods

Neural networks segmentation methods [Egmont-Petersen 2002] rely on processing small areas of an image using an artificial neural network (ANN). The main advantages of ANN are as follows:
1. Ability to learn adaptively, using training data to solve complex problems.
2. Capability of self-organization; it can create its own organization depending on the information it receives during learning time.
3. Capability of performance in real time because of parallel configuration.
Also, ANN represents a paradigm for machine learning and can be used in a variety of ways for image segmentation. It can be specially used in medical image segmentation as a classifier, where the weights are determined using training date, and the artificial neural networks are used to segment new data.

2.1.7 Clustering methods

Image segmentation may be considered a clustering process in which the pixels are classified into the attribute regions based on the texture feature vector calculated around the pixel local neighborhood. Such methods do not require training data but they do require an initial segmentation.

Three commonly used clustering methods are the K-means method, the fuzzy c-means method, the expectation-maximization method.

2.2 Aneurysm segmentation methods and results

By now, there is a lot of literature about lumen segmentation and less literature about aneurysm segmentation. In this section we will show several lumen and aneurysm segmentation results by using Otsu method, geodesic active contour method (GAC) and Chan-Vese method (CV)and lattice Boltzmann based GAC method (LBGAC).

2.2.1 Otsu method

Ostu method [Otsu 1975] is one of threshold methods. It is used to automatically perform clustering based image thresholds. The algorithm assumes that the image contains two classed of pixels: background and object. Maximizing inter-class variance means that the difference between background and object is maximum.

We can define the inter-class variance as the weighted sum of the variances of each cluster:

$$\sigma_{\omega}^{2}(t) = \omega_1(t)\,\sigma_1^2(t) + \omega_2(t)\,\sigma_2^2(t)\,. \tag{2.5}$$

where ω_i is the probability in i class and σ_i^2 is the variance of the pixels in each class.

Otsu shows that minimizing the intra-class variance is the same as maximizing inter-class variance

$$\sigma_b^2(t) = \sigma^2(t) - \sigma_{\omega}^2(t) = \omega_1(t)\,\omega_2(t)\,[\mu_1(t) - \mu_2(t)]^2 \tag{2.6}$$

where μ_i is class means. So, for each potential threshold T we

1) Separate the pixels into two classes according to the threshold.
2) Find the mean of each class.
3) Square the difference between the means.
4) Multiply by the number of pixels in one class times the number in the other.

This method performs on aneurysm image and we can see the result in Figure 2.3.

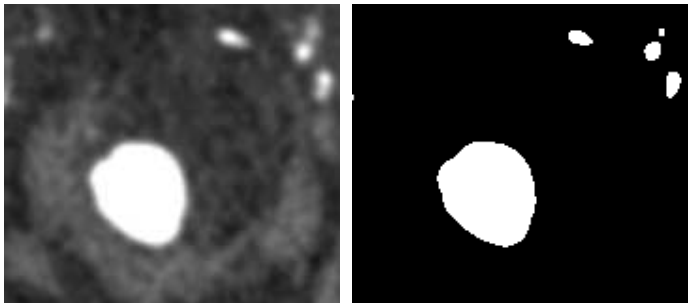

FIGURE 2.3: In left: Original image; in right: image result.

2.2.2 Level set method

Level set method was first introduced in [Dervieux 1980] and then devised by Osher and Sethian [Osher 1988]. The main idea of the level set method can be described as follows. In an open region Ω, C is a closed interface evolving with the velocity v. The goal is to analyze and compute the motion of the interface. Osher and Sethian's idea is to define an implicit smooth (Lipschitz continuous) function $\phi(\vec{x}, t)$ which represents the interface as the set where

$$\begin{cases} \phi(\vec{x}, t) < 0 & \vec{x} \in \Omega^-, \\ \phi(\vec{x}, t) = 0 & \vec{x} \in C, \\ \phi(\vec{x}, t) > 0 & \vec{x} \in \Omega^+. \end{cases} \tag{2.7}$$

where Ω^- shows the area inside the interface and Ω^+ shows the area outside.

The evolution could be described by convecting the ϕ with the velocity field v on the interface

$$\frac{\partial \phi}{\partial t} + v\delta(\phi) = 0 \tag{2.8}$$

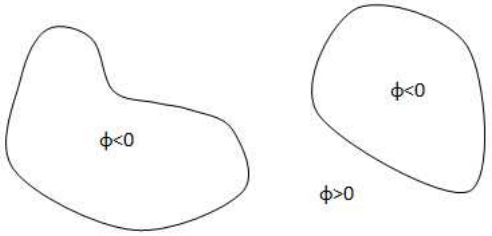

FIGURE 2.4: The construction of level set function.

Then we would like to introduce two classic level set method, geometric active contour (GAC) and Chan-Vese (CV) model.

2.2.2.1 GAC method

GAC method [Caselles 1997] is one of edge-based segmentation methods and the level set method without reinitialization GAC model is proposed by Li Chunming [Li 2010]. The GAC model is formulated by minimizing the following energy function

$$E^{GAC} = \int_0^1 g\left(\left|\nabla I\left(C\left(q\right)\right)\right|\right)\left|C'\left(q\right)\right| dq \tag{2.9}$$

$$g\left(\left|\nabla I\right|\right) = \frac{1}{1+\left|\nabla G_\sigma * I\right|^2} \tag{2.10}$$

where $G_\sigma * I$ denotes convolving image I with a Gaussian kernel whose standard deviation is σ.

The corresponding level set formulation is as follows

$$\frac{\partial \phi}{\partial t} = \mu\left[\Delta\phi - div\left(\frac{\nabla\phi}{|\nabla\phi|}\right)\right] + \delta\left(\rho\right)\left[\lambda div\left(g\frac{\nabla\phi}{|\nabla\phi|}\right) + \nu g\right] \tag{2.11}$$

where ϕ is the distance function, and g the edge indicator function. The first term in the right side is a penalty term used to penalize the deviation of ϕ from a signed distance function during its evolution, and the second term is the gradient flow of the energy function.

Figure 2.5 in left, the lumen part is segmented well. Figure 2.5 in right shows the boundary of the whole aneurysm which contains both lumen and thrombus part.

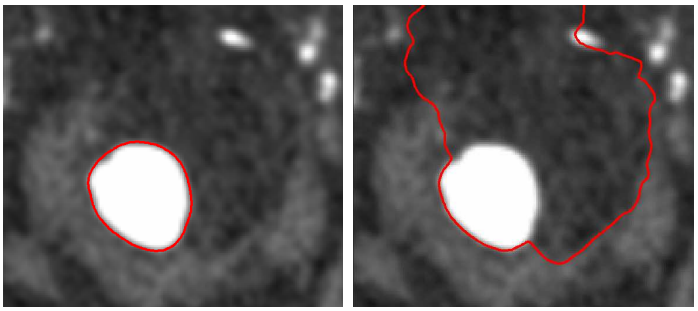

FIGURE 2.5: GAC results by choosing different initial contours.

We can observe clearly that the wall of the aneurysm is not well segmented with contour leakage in upper left area.

As a conclusion, the GAC model could have good performance on lumen segmentation if it's provided good initial contour. But it's really difficult to obtain the complete aneurysm segmentation by using GAC model.

2.2.2.2 CV method

CV method is one of region-based segmentation methods which proposed by Chan and Vese [Chan 2001]. For a given image I, the CV model is formulated by minimizing the following energy functional

$$E^{CV} = \lambda_1 \int_{inside(C)} |I(x) - c_1|^2 dx + \lambda_2 \int_{outside(C)} |I(x) - c_2|^2 dx \tag{2.12}$$

where C is the curve, c_1 and c_2 are two constants which are the average gray level inside and outside the contour, respectively, and I is the gray level of the image.

By incorporating the length and area energy term into energy function and minimizing them, we obtain the corresponding variational level set formulation as follows

$$\frac{\partial \phi}{\partial t} = \delta(\phi) \left[\mu div \left(\frac{\nabla \phi}{|\nabla \phi|} \right) - \nu - \lambda_1 (I - c_1)^2 + \lambda_2 (I - c_2)^2 \right] \tag{2.13}$$

where μ controls the smoothness of zero level set, ν increases the propagation speed, λ_1 and λ_1 control the image data driven force inside and outside the contour. ∇ is the gradient operator. $\delta(\phi)$ is the Dirac function.

As can be observed in Figure 2.6, the CV model just obtains a good lumen contour.

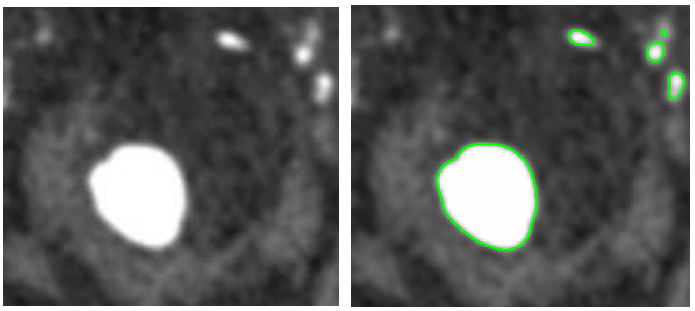

FIGURE 2.6: CV segmentation result.

2.2.3 LBGM

Lattice Boltzmann based GAC method (LBGM) [Chen 2014] is one of partial differential equation based methods. In this method, LBM is applied to solve the GAC evolution equation (2.11).

The first part of equation (2.11) can be written as

$$A_1 = \frac{\rho\left(t+\sigma_t\right)-\rho\left(t\right)}{\sigma_t} \approx \frac{\lambda {\sigma_h}^2}{3\sigma_t} div\left(g\frac{\nabla\rho}{\left|\nabla\rho\right|}\right)+\nu g \tag{2.14}$$

with $\tau = c+\lambda g/\left|\nabla\rho\right|,\ c \geq 0.5$ in LBM.

The second part of equation (2.11) can be written as

$$A_2 \approx div\left(\mu\left(1-\frac{1}{\left|\nabla\rho\right|}\right)\nabla\rho\right) \tag{2.15}$$

Thereby, the idea of solving equation (2.11) can be divided into 3 steps:

1) Apply LBM to simulate the gradient flow of the energy function.
2) Discretize the penalty term by central difference scheme.
3) Update and go to step 1.

We perform the lattice Boltzmann based GAC method on Figure 2.7 in left. The original image with initial contour and the result are shown in middle and in right of Figure 2.7, respectively.

Then we can find lattice Boltzmann based GAC method can segment aneurysm by choosing an initial contour near the aneurysm contour.

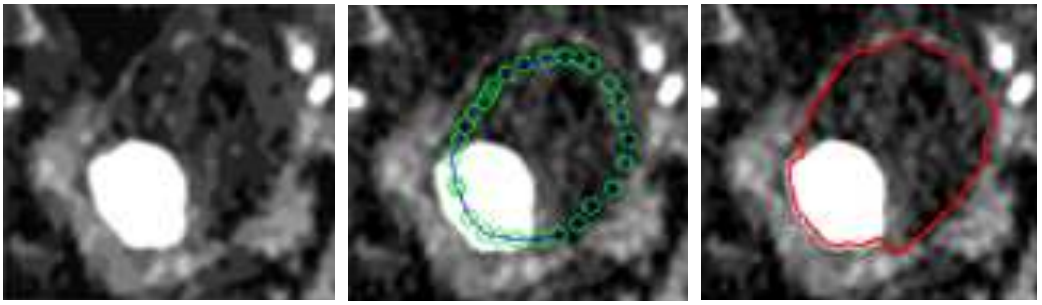

FIGURE 2.7: In left: the original image; in middle: initial contour; in right: the result.

All these methods are the recently research about aneurysm segmentation and we can see there are still a lot of work to do. In other words, aneurysm segmentation is still a challenge.

2.3 Conclusion

Widely used segmentation methods are shown in this chapter. Furthermore, we present the performance of these methods working on aneurysm segmentation. Generally, they work well on lumen segmentation but few methods could have good performance on thrombus segmentation. The limitation of these methods makes thrombus segmentation still an open question. And segmenting thrombus becomes the first objective of this thesis.

Chapter 3

General lattice Boltzmann method

Abstract

Lattice Boltzmann method (LBM) is developed from lattice gas automata (LGA) which was first proposed in 1973 [Hardy 1973]. In one way, LBM is a model that can describe the fluid flow. Also, LBM could be viewed as the discrete format of the continuous Boltzmann equation. In another way LBM is a mesoscopic mathematical method. In this chapter, we present the general HPP, FHP and LBM models which include the collision step, streaming step and boundary conditions.

Résume

La méthode de Boltzmann sur réseau (LBM) est développée à partir de la méthode de gaz sur réseaux, qui a été proposée en 1973 [Hardy 1973]. Dans ce chapitre, la méthode de gaz sur réseaux (HPP et FHP) et LBM ont été présenté en détail. LBM comprend l'étape de collision et l'étape de propagation, également le choix des conditions aux limites est une partie essentielle de LBM.

3.1 Lattice gas automata

LGA and its later derivative, LBM, are approaches that use simple microscopic models to simulate macroscopic behavior of fluid flow.

3.1.1 HPP

The first LGA model is named HPP which was proposed in 1973 by Hardy, de Pazzis and Pomeau. HPP is a two-dimensional LGA model over a square lattice. It is assumed that 1) the lattice is composed of squares with a unit length between neighboring sites. 2) particles of unit mass and unit velocity move along the lattice links and reside at the nodes at integer time. 3) just one particle is allowed at a time and a node, moving in a given direction. Let $n_i(x,t)$ denote the Boolean

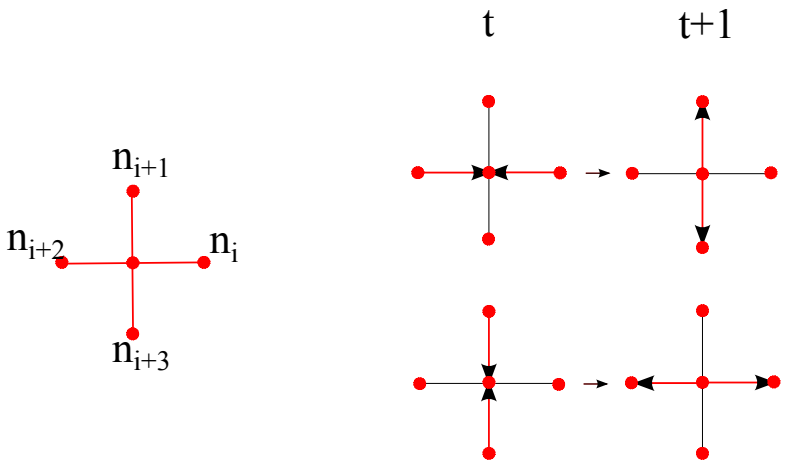

FIGURE 3.1: Example of HPP model: the four directions of an HPP node were shown in left and collision rules for HPP model in right.

field at the discrete position r and time t with i, i+1, i+2, i+3 labeling the four directions of an HPP node. The collision rules for HPP model is shown in Figure 3.1. For a two-particle collision with input channels (n_i, n_{i+2}), the output channels are (n_{i+1}, n_{i+3}), which conserve mass and momentum. Also, for input channels (n_{i+1}, n_{i+3}), the output are (n_i, n_{i+2}). In this way, the state of n_i of node $x+\vec{e}_i$ at time $t+1$ depends on the states of node r at time t and collisions. The condition $n_i(x+\vec{e}_i, t+1) = 1$ exists either 1) $n_i(r,t) = 1$ and without collision, or 2) $n_i(r,t) = 0$ but with collision. The updating of this Boolean field can be written as

$$n_i(\vec{x}+\vec{e}_i, t+1) = n_i\left[1 - n_{i+2}(1-n_{i+1})(1-n_{i+3})\right] + n_{i+1}n_{i+3}(1-n_i)(1-n_{i+2}) \quad (3.1)$$

or

$$n_i(\vec{x} + \vec{e}_i, t + 1) = n_i(\vec{x}, t) + \Delta_i \tag{3.2}$$

where $\vec{e}_i$ is the unit lattice velocity vectors, Δ_i is collision function, describes the change in $n_i(x, t)$ due to collisions. The collision function can be written as

$$\Delta_i = n_{i+1}n_{i+3}(1 - n_i)(1 - n_{i+2}) - n_i n_{i+2}(1 - n_{i+1})(1 - n_{i+3}). \tag{3.3}$$

3.1.2 FHP

Frisch, Hasslacher and Pomeau (FHP) proposed another lattice gas automata model in 1986 [Frisch 1986]. It is assumed that: 1) the FHP lattice is composed of triangles with a unit length between six neighbors. 2) particles of unit mass and unit velocity move along the lattice links. 3) just one particle is allowed at a time and a node with six directions. That is to say, the FHP model is based on a two-dimensional triangular lattice and each node is connected to its six neighbors. As for HPP, let $n_i(x, t)$ denote the Boolean field at the discrete position r and time t with i, i+1, i+2, i+3, i+4, i+5 labeling the six directions of an FHP node and FHP has two-particle collision. Also, it has three-particle and four-particle collisions. First, we present two-particle and four-particle collisions in Figure 3.2 and Figure 3.3, respectively (because they all have two possibilities for each case). Then, we show the two types of three-particle collision in Figure 3.4. As we can see, FHP model is more complex and reasonable. Meanwhile, HPP and FHP have the same evolution equation with different collision function

$$n_i(x + \vec{e}_i, t + 1) = n_i(x, t) + \Delta_i. \tag{3.4}$$

3.2 Lattice Boltzmann method

3.2.1 LBM model

McNamara and Zanetti [McNamara 1988] firstly introduced LBM by using the mean population instead of n_i in order to get rid of the noise from LGA models. The evolution of lattice Boltzmann method can be written as

$$f_i(\vec{x} + \Delta t\vec{e}_i, t + \Delta t) = f_i(\vec{x}, t) + \Omega_i \tag{3.5}$$

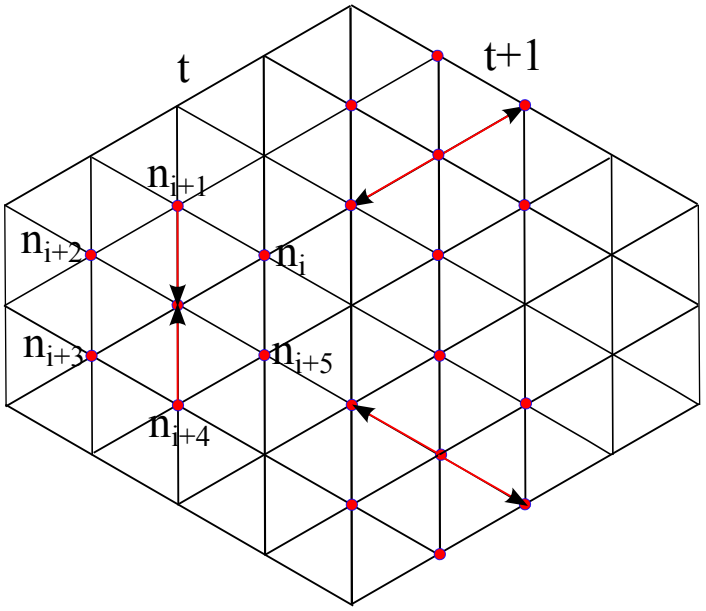

FIGURE 3.2: The possibility of two-particle collision rules for FHP model: with input channels (n_{i+1}, n_{i+4}), the output channels are (n_i, n_{i+3}) or (n_{i+2}, n_{i+5}), which conserve mass and momentum.

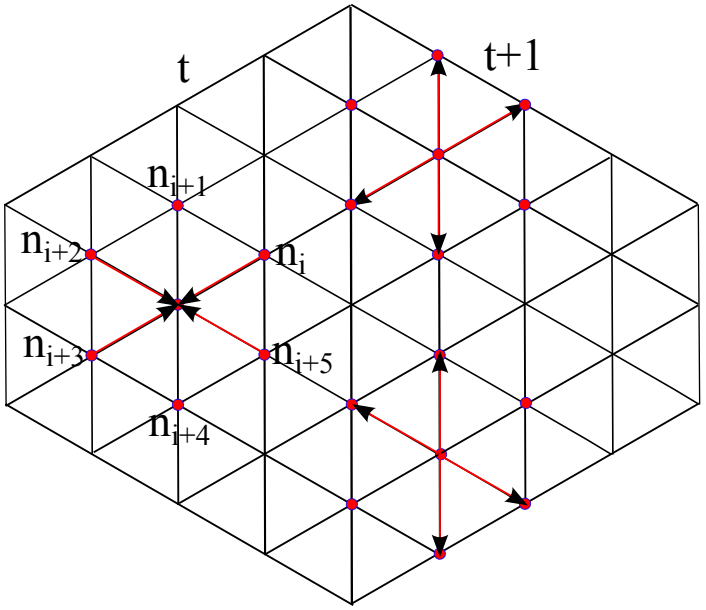

FIGURE 3.3: Two possibility of four-particle collision rules for FHP model and its triangle lattice.

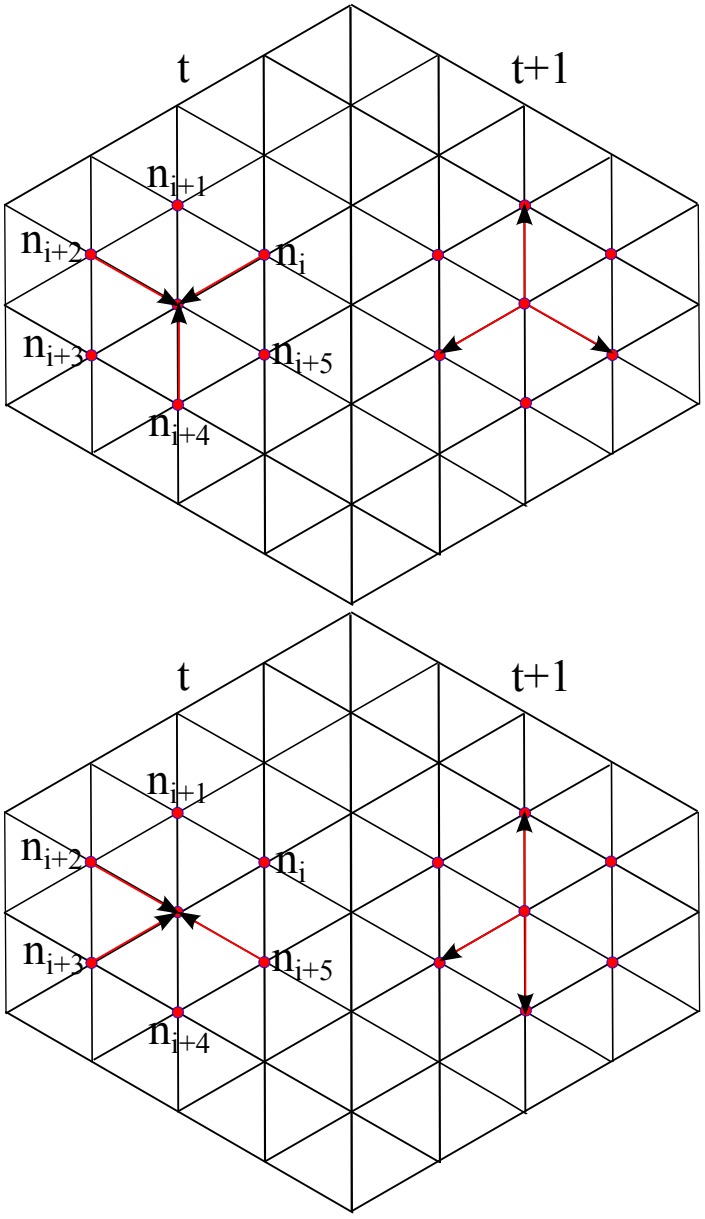

FIGURE 3.4: FHP has two types three-particle collision. Firstly, n_i, n_{i+2}, n_{i+4}) as input channels, and $(n_{i+1}, n_{i+3}, n_{i+5})$ are output channels. Secondly, $(n_{i+2}, n_{i+3}, n_{i+5})$ are input channels, and $(n_{i+1}, n_{i+3}, n_{i+4})$ are output channels.

where $f_i(\vec{x}+\Delta t\vec{c}_i, t+\Delta t)$ is the distribution function at node $\vec{x}+\Delta t\vec{c}_i$, at time $t+\Delta t$, with $\vec{e}_i$ designating lattice velocity and Δt time step; $f_i(\vec{x}, t)$ is the distribution function at node $\vec{x}$ at time t. Ω_i is LBM collision function representing the rate of change of the particle distribution function due to collisions. For each step, the updating of the particle distribution can be split into two sub steps: collision and streaming

$$Collision: \quad f_i'(\vec{x}, t) = f_i(\vec{x}, t) + \Omega_i \tag{3.6}$$

$$Streaming: \quad f_i(\vec{x} + \Delta t\vec{e}_i, t + \Delta t) = f_i'(\vec{x}, t). \tag{3.7}$$

Modern LBM with Boltzmann distribution function, several lattice velocity (use lattice velocity $\vec{e}_i$ instead of unit lattice velocity $\vec{c}_i$) and BGK approximation of the collision function have some advantages. In 1954, [Bhatnagar 1954] proposed a model named lattice BGK (LBGK) model by using Maxwell equilibrium distribution and BGK approximation. The LBGK model can be written as

$$f_i(\vec{x} + \Delta t\vec{e}_i, t + \Delta t) - f_i(\vec{x}, t) = -\frac{1}{\tau}[f_i(\vec{x}, t) - f_i^{eq}(\vec{x}, t)] \tag{3.8}$$

where τ is relaxation time which controls the rate of approaching the equilibrium. $f_i^{eq}(\vec{x}, t)$ is equilibrium function at node $\vec{x}$ at time t

$$f_i^{eq} = \omega_i \rho \left[1 + \frac{\vec{e}_i\vec{u}}{c_s^2} + \frac{(\vec{e}_i\vec{u})^2}{2c_s^4} - \frac{\vec{u}^2}{2c_s^2}\right] \tag{3.9}$$

where ω_i is constant, ρ is mass density, c_s is the sound velocity of lattice, $\vec{e}_i$ is lattice velocity, u is velocity of fluid. Also, we have

$$\rho = \sum_i f_i \tag{3.10}$$

$$\rho\vec{u} = \sum_i \vec{e}_i f_i. \tag{3.11}$$

We would like to explain LBGK by taking D2Q9 model (Figure 3.5) as an example, which contains two dimension with nine directions at each node. Particles can only reside on the nodes and move to their nearest neighbors along links. There are three types of moving particles. Particles of type 1 with lattice velocity $e_i^2 = 0$ stay on the nodes, particles of type 2 move along the axes with lattice velocity $e_i^2 = 1$ and particles of type 3 move along the diagonal directions with lattice velocity $e_i^2 = 2$. Also, we give some lattice velocity models and its corresponding parameters.

D1Q3:

$$e = [0, 1, -1],\ c_s = \frac{1}{\sqrt{3}},\ \omega_i = \begin{cases} 2/3, & e_i^2 = 0 \\ 1/6, & e_i^2 = 1 \end{cases} \tag{3.12}$$

D2Q9:

$$e = \begin{bmatrix} 0 & 1 & 0 & -1 & 0 & 1 & -1 & -1 & 1 \\ 0 & 0 & 1 & 0 & -1 & 1 & 1 & -1 & -1 \end{bmatrix} \tag{3.13}$$

$$c_s = \frac{1}{\sqrt{3}},\ \omega_i = \begin{cases} 4/9, & e_i^2 = 0 \\ 1/9, & e_i^2 = 1 \\ 1/36, & e_i^2 = 2 \end{cases} \tag{3.14}$$

D3Q15:

$$e = \begin{bmatrix} 0 & 1 & -1 & 0 & 0 & 0 & 0 & 1 & -1 & 1 & -1 & 1 & -1 & -1 & 1 \\ 0 & 0 & 0 & 1 & -1 & 0 & 0 & 1 & -1 & 1 & -1 & -1 & 1 & 1 & -1 \\ 0 & 0 & 0 & 0 & 0 & 1 & -1 & 1 & -1 & -1 & 1 & 1 & -1 & 1 & -1 \end{bmatrix} \tag{3.15}$$

$$c_s = \frac{1}{\sqrt{3}},\ \omega_i = \begin{cases} 2/9, & e_i^2 = 0 \\ 1/9, & e_i^2 = 1 \\ 1/72, & e_i^2 = 3 \end{cases} \tag{3.16}$$

D3Q19:

$$e = \begin{bmatrix} 0 & 1 & -1 & 0 & 0 & 0 & 0 & 1 & -1 & 1 & -1 & 1 & -1 & -1 & 1 & 0 & 0 & 0 & 0 \\ 0 & 0 & 0 & 1 & -1 & 0 & 0 & 1 & -1 & -1 & 1 & 0 & 0 & 0 & 0 & 1 & -1 & 1 & -1 \\ 0 & 0 & 0 & 0 & 0 & 1 & -1 & 0 & 0 & 0 & 0 & 1 & -1 & 1 & -1 & 1 & -1 & -1 & 1 \end{bmatrix} \tag{3.17}$$

$$c_s = \frac{1}{\sqrt{3}},\ \omega_i = \begin{cases} 1/3, & e_i^2 = 0 \\ 1/18, & e_i^2 = 1 \\ 1/36, & e_i^2 = 2 \end{cases} \tag{3.18}$$

3.2.2 Boundary conditions

Boundary conditions are an important issue in LBM. Considering the specific use in image processing, here we only give some essential ideas.

3.2.2.1 Bounce-back boundary condition

Bounce-back is the simplest way to deal with a wall and does not require any knowledge of its shape. It is enough to know that a given site is a wall. When particles reach such a solid site, they just bounce back from where they came (see Figure 3.5). The solid lines together with arrow represent the original vectors and the dotted lines are the bounce back vectors. There is always a direction which is valid since particles have just arrived from that direction.

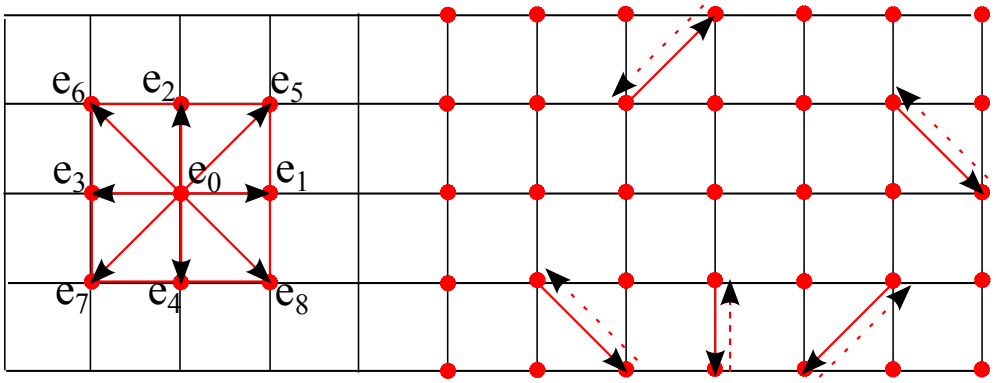

FIGURE 3.5: D2Q9 model with nine directions in left, bounce back boundary condition in right.

3.2.2.2 Zou & He boundary condition

Zou & He Boundary Condition is proposed as follows: take the case of a bottom node, the boundary is aligned with x-direction with f_4, f_7, f_8 pointing into the wall. After propagation, f_0, f_1, f_3, f_4, f_7, f_8 are known. Suppose that u_x, u_y are specified on the wall, we need to determine f_2, f_5, f_6 and ρ from equations (3.10) and (3.11), which can be put into the form

$$f_2 + f_5 + f_6 = \rho - (f_0 + f_1 + f_3 + f_4 + f_7 + f_8) \tag{3.19}$$

$$f_5 - f_6 = \rho u_x - (f_1 - f_3 - f_7 + f_8) \tag{3.20}$$

$$f_2 + f_5 + f_6 = \rho u_y + (f_4 + f_7 + f_8) \tag{3.21}$$

then,

$$\rho = \frac{1}{1 - u_y}[f_0 + f_1 + f_3 + 2(f_4 + f_7 + f_8)]. \tag{3.22}$$

We assume the bounce-back rule is still correct for the non-equilibrium part of the particle distribution normal to the boundary. With f_2 known, f_5, f_6 can be found as

$$f_2 = f_4 + \frac{2}{3}\rho u_y \tag{3.23}$$

$$f_5 = f_7 - \frac{1}{2}(f_1 - f_3) + \frac{1}{2}\rho u_x + \frac{1}{6}\rho u_y \tag{3.24}$$

$$f_6 = f_8 + \frac{1}{2}(f_1 - f_3) - \frac{1}{2}\rho u_x + \frac{1}{6}\rho u_y. \tag{3.25}$$

The collision step is applied to the boundary nodes also.

3.3 Conclusion

Two of the simplest lattice gas automata models (HPP and FHP) are introduced in this chapter. The connection between lattice automata equation and lattice Boltzmann equation gives us a general idea about lattice Boltzmann method. Besides, we present different discrete velocity models and boundary conditions.

Part II

CONTRIBUTIONS

Chapter 4

LBM applied to image processing

Abstract

The LBM has been successfully applied to hydrodynamic simulations. It also has a great interest in the development of algorithms for image processing such as denoising or segmentation. The main problem is the adaptation of the model and its formulation for specific applications.

In this chapter, we propose a class of methods using a model of anisotropic diffusion based on the LBM for image segmentation. Specifically, a "membrane" is added between the nodes of the model, and a diffusion term is added to the traditional Boltzmann equation to adapt it to image segmentation. Then, we introduce the parameters corresponding to D2Q9, D3Q27 and D4Q81 models. Tests are performed on synthetic images, such as a 2D circle, a 3D sphere and a 4D hypersphere. These tests show that the proposed segmentation models are robust to noise and lead to accurate results with high coefficient values Dice .

Résume

La méthode de Boltzmann sur réseau (Lattice Boltzmann method: LBM) a été utilisé avec succès à des simulations en hydrodynamique. Elle présente aussi un grand intérêt pour l'élaboration d'algorithmes de traitement d'image comme le débruitage ou la segmentation. Le problème principal est l'adaptation du modèle et sa formulation pour des applications spécifiques.

Dans ce chapitre, nous proposons une catégorie de méthodes utilisant un modèle de diffusion anisotrope basé sur la méthode de Boltzmann sur réseau pour la segmentation des images. Plus précisément, une "membrane" est ajoutée entre les nœuds du modèle, et un terme de diffusion est ajouté à l'équation de Boltzmann traditionnelle afin de l'adapter à la segmentation d'image. Ensuite, nous introduisons les paramètres correspondant aux modèles D2Q9, D3Q27 et D4Q81. Des tests sont effectués sur les images synthétiques, par exemple un cercle en 2D une sphère en 3D et une hypersphère en 4D. Ces tests montrent que les modèles de segmentation proposés sont robustes au bruit et conduisent à des résultats précis avec des valeurs de coefficients de Dice élevées.

4.1 Introduction

The LBM is nowadays a common and practical mesoscopic mathematical tool devoted to solving macroscopic fluid dynamics problems generally described by partial differential equations (Navier-Stokes equations in case of fluid mechanics problems). The idea of the LBM is to construct a simplified discrete dynamics at mesoscopic scales by implementing particles distributions on a lattice to simulate macroscopic behaviors. In the past of few years, some researchers started to introduce LBM into image processing.

The application of LBM to image processing was reported in the literature. The authors of [Jawerth 1999] firstly applied the LBM to image processing, especially to nonlinear anisotropic diffusion of images. In the paper [Zhao 2008], the authors proposed the GPU-accelerated LBM to solve the diffusion [Wolf-Gladrow 1995] lattice problems including volume smoothing, surface fairing, image editing. Also, a LBM for image denoising was mentioned in [Chang 2009]. [Chen 2008] suggested an anisotropic diffusion model based on the LBM to make medical images smooth. A review of nonlinear diffusion filtering can be found in [Y.Chen 2009]. More recently, [Chen 2014] used LBM as a technique to solve GAC equation. Also, [Wang 2011] proposed a LBM-based anisotropic diffusion model to segment the lumen and the thrombus of aneurysm.

In this chapter, we focus on the segmentation method in 2D, 3D and 4D using LBM. Firstly, the traditional lattice Boltzmann (LB) equation is adapted to image segmentation by using the gray level instead of density of fluid in LBM. Secondly, LBM with g probability of transmission model also named LBM anisotropic diffusion model is presented. Then, the most important model, LBM anisotropic diffusion segmentation model is introduced by integrating a diffusion source term in the LBM anisotropic diffusion formulation. In the end, we give the parameters and models about image segmentation in 2D, 3D and 4D by using LBM. More precisely, the test images like circle, sphere and hypersphere are segmented in this chapter too.

4.2 LBM based image processing model

4.2.1 LBM in image processing

For two dimensional discrete images, the pixels arrangement can be naturally considered to be lattice and the gray level distribution of pixels in image domain is regarded as f_i. That is to say, we will treat the image intensity as the particle density in the LBM.

As we mensioned in chapter 3, the common LBM equation is

$$f_i(\vec{x} + \Delta t\vec{e}_i, t + \Delta t) - f_i(\vec{x}, t) = -\frac{1}{\tau}[f_i(\vec{x}, t) - f_i^{eq}(\vec{x}, t)] \tag{4.1}$$

here, $f_i(\vec{x}, t)$ is the gray level distribution at node x and at time t. $\vec{e}_i$ is lattice velocity which depends on different LBM models and f_i^{eq} is the same as equation (3.9). By taking $\vec{u} = 0$ in consideration, then the equilibrium function can be developed as follows in image processing

$$f_i^{eq} = \omega_i \rho. \tag{4.2}$$

4.2.2 LBM anisotropic model

Then, we introduce a medium in the LBM and the medium has a significant characteristic that it will let only some particles pass and let the others not pass. Assuming that when a particle moves to neighboring nodes, it can pass through the medium with a probability g_i and bounces back with a probability $1 - g_i$. So if there are N particles moving along direction i, $N \cdot g_i$ particles will pass the medium and $N \cdot (1 - g_i)$ particles will be rebounded.

That is to say, the state of the node at the next time is equal to the sum of the particles rebounded back from the medium and the neighboring particles traveling through the medium. Thus, the LBM evolution equation can be modified as

[Y.Chen 2009]

$$\begin{aligned} f_i(\vec{x}+\Delta t\vec{e_i}, t+\Delta t) &= g_i(\vec{x})\{f_i(\vec{x},t)+\frac{1}{\tau}[f_i^{eq}(\vec{x},t)-f_i(\vec{x},t)]\} \\ &+ [1-g_i(\vec{x}+\Delta t\vec{e_i})]\{f_i(\vec{x}+\Delta t\vec{e_i},t) \\ &+ \frac{1}{\tau}[f_i^{eq}(\vec{x}+\Delta t\vec{e_i},t)-f_i(\vec{x}+\Delta t\vec{e_i},t)]\}. \end{aligned} \tag{4.3}$$

where f_i is the gray level of pixels and g_i, which is related with the gray level of pixels, is the probability for particles to pass through the medium. g_i is given in [Y.Chen 2009]

$$g_i(\vec{x}) = \frac{1}{\left[1+\frac{|G*\rho(\vec{x},t)-G*\rho(\vec{x}+\vec{e}_i\Delta t,t)|}{10}\right]^2} \tag{4.4}$$

4.2.3 LBM anisotropic diffusion segmentation model

In order to segment the images, we also need to add a 'extra force term' in the LBM anisotropic diffusion model. The evolution equation in this case is given by

$$\begin{aligned} f_i(\vec{x}+\Delta t\vec{e_i}, t+\Delta t) &= g_i(\vec{x})\{f_i(\vec{x},t)+\frac{1}{\tau}[f_i^{eq}(\vec{x},t)-f_i(\vec{x},t)]\} \\ &+ [1-g_i(\vec{x}+\Delta t\vec{e_i})]\{f_i(\vec{x}+\Delta t\vec{e_i},t) \\ &+ \frac{1}{\tau}[f_i^{eq}(\vec{x}+\Delta x\vec{e_i},t)-f_i(\vec{x}+\Delta t\vec{e_i},t)]\} \\ &+ a\Delta t[\rho(\vec{x})-T] \end{aligned} \tag{4.5}$$

where $a\Delta t[\rho(\vec{x})-T]$ represents the extra force term with constant a and Δt and T is the threshold calculated from the Otsu technique.

The algorithm of image segmentation is given as follows
1) Initialize the equilibrium function as equation (4.2).
2) Set the initial value of f_i with function: $f_i = f_i^{eq}$.
3) Collision and streaming steps with equation (3.6), (3.7) and get new f_i.
4) If it satisfies the convergence condition, do 7), if not, do 5).
5) Update the state of ρ using equation (3.10).
6) Compute the equilibrium function with equation (4.2).
7) End and output.

In step 4), if results of N and N+1 iterations are represented by A and B respectively, and if σ defined in below equation is smaller than 0.5%

$$\sigma = \frac{A - B}{A} \times 100\% \leq 0.5\% \tag{4.6}$$

then we say the convergence condition is satisfied and the segmentation process can be stopped.

Equation (4.5) is our main evaluation equation in the following segmentation work and we will show the values of $\vec{e}_i$ and f_i^{eq} in the rest sections.

The comparison between the general LBM and LBM in image processing is given in Figure 4.1. The first difference is that we replace the particle distribution with gray

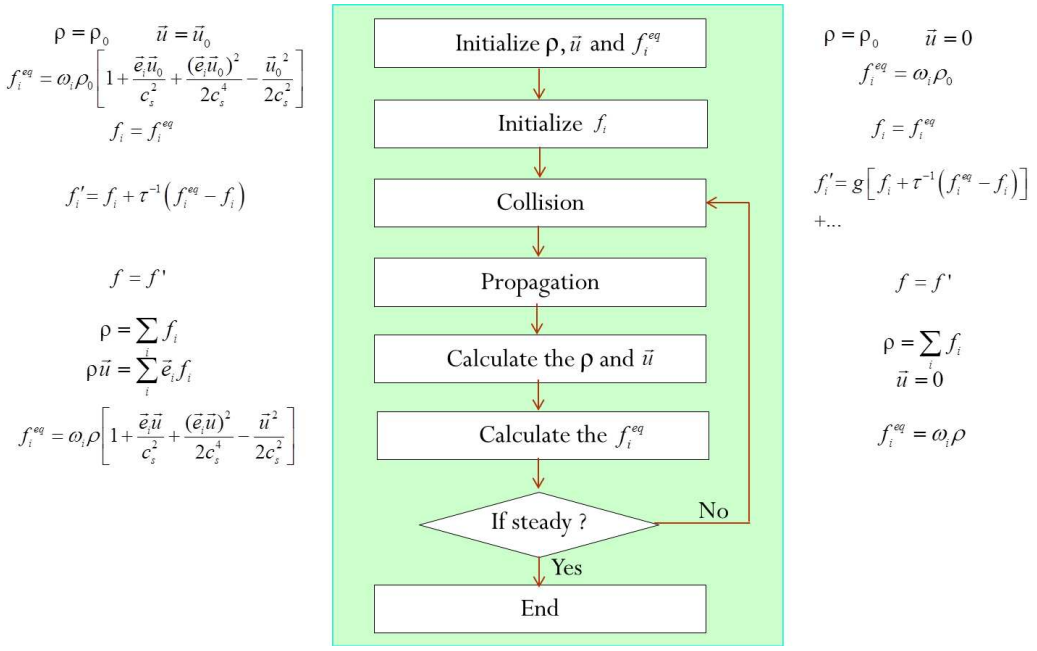

FIGURE 4.1: The general LBM and LBM in image processing.

level distribution. The second difference is that we set $u = 0$ in image processing and it leads a different expression of f_i^{eq}. At last, the evolution equations are different.

4.3 2D model and parameters

4.3.1 2D methodology

There are different LBM models in 2D, such as D2Q5, D2Q7 and D2Q9 models. The D2Q9 model is defined in two dimensions with nine directions per node. Comparing with these models, the numbers of the direction per node are different. D2Q9 has better symmetrical structure, and that is why it is the most common model in 2D cases. Also, in our study we focus on D2Q9 model in 2D image segmentation. For this model, the lattice and its possible directions are show in Figure 4.2.

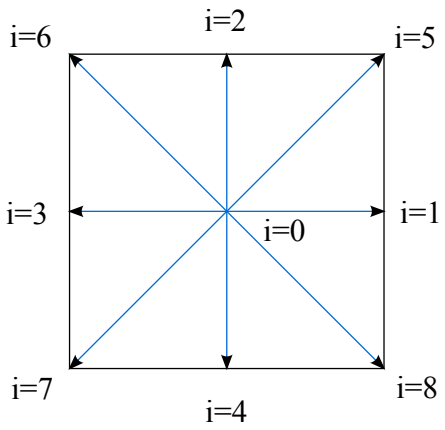

FIGURE 4.2: D2Q9 model.

There are nine directions per node, from $i = 0$ to $i = 8$ in Figure 4.2. In one LBM iteration, particle can move along the directions to its neighbors. Note that the direction i=0 is defined to describe a population $f_i(\vec{x}, t)$ of particles at rest. As we mentioned in 4.2.3, the LBM anisotropic diffusion segmentation model (see Figure 4.3) is used in 2D segmentation.

Figure 4.3 in left is the common D2Q9 model, and in right is the model with medium. The parameters of $\vec{e_i}$ and f_i^{eq} should take in charge in this model.

For this model, each pixel has eight nearest neighbors and itself, the lattice vector defined as $\vec{e_i}$. According to [Wolf-Gladrow 2000], which presented D2Q9 model in

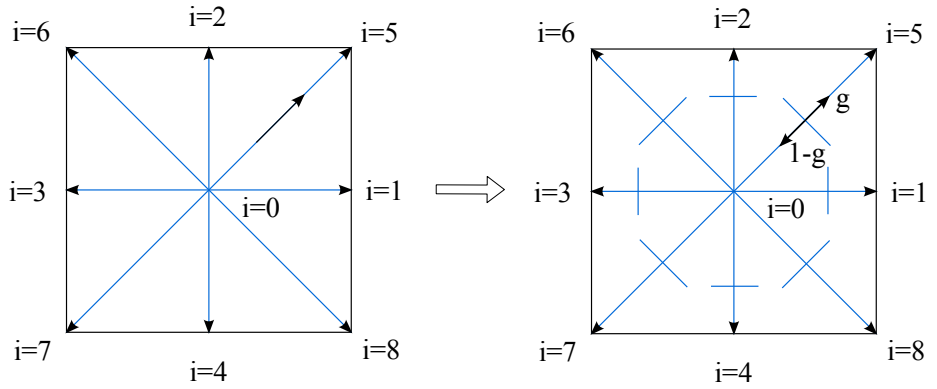

FIGURE 4.3: Principle of streaming and collision in the presence of medium.

detail, we choose $\vec{e}_i$ as follows in this present study

$$\vec{e}_i = \begin{cases} 0 & i = 0 \\ (cos(\pi(i-1)/2), sin(\pi(i-1)/2)) & i = 1,2,3,4 \\ \sqrt{2}(cos(\pi(i-\frac{9}{2})/2)), sin(\pi(i-\frac{9}{2})/2)) & i = 5,6,7,8. \end{cases} \tag{4.7}$$

Also, taking $\vec{u} = 0$ in consideration, the equilibrium function can be developed as follows

$$f_i^{eq} = \begin{cases} \frac{4}{9}\rho(\vec{x},t) & i = 0 \\ \frac{1}{9}\rho(\vec{x},t) & i = 1,2,3,4 \\ \frac{1}{36}\rho(\vec{x},t) & i = 5,6,7,8 \end{cases} \tag{4.8}$$

4.3.2 Experiments and results

The proposed 2D segmentation method was performed on test image of which size is (100, 100). And we define that the range of its gray level is [0, 255]. The main object of this image is a circle of which center is (50, 50) and radius is 30. The gray level of this object is 150 and the gray level of background is 200. Figure 4.4 illustrates the original image and its corresponding result.

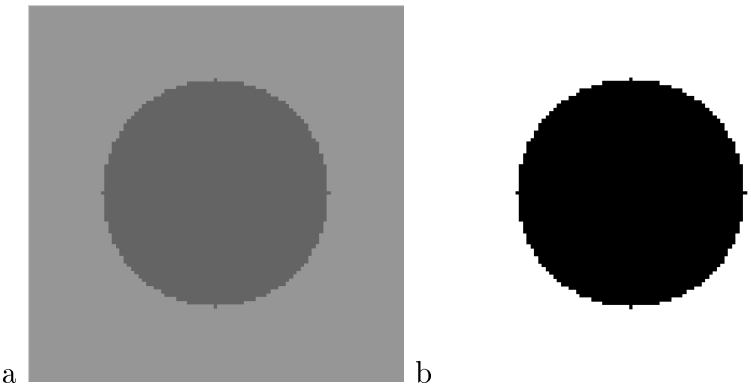

FIGURE 4.4: The original 2D circle image in left and the segmentation result in right.

4.4 3D model and parameters

4.4.1 3D methodology

As the same with 2D model, there are different 3D models. D3Q15, D3Q19 and D3Q27 are most common models in 3D LBM. The difference between them is that the numbers of direction per node of each model are different. Normally, if the LBM model has more directions in one node, it will be more accuracy and also more calculated time will be needed. Specially comparing with fluid simulation, LBM in image processing has less lattice and less iteration steps. That is why D3Q27 is a good choice in our study. For this model, the lattice and its possible directions are show in Figure 4.5.

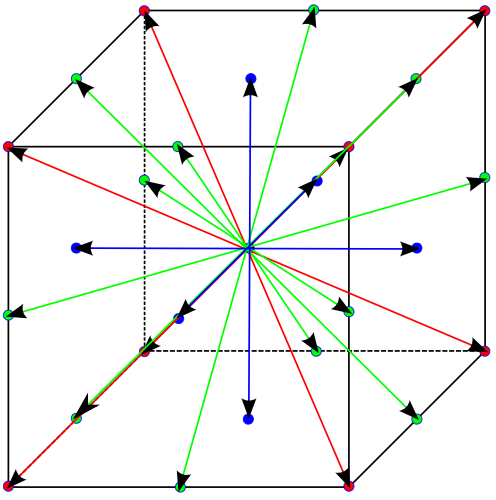

FIGURE 4.5: D3Q27 model.

There are twenty-seven directions per node, which correspond to the arrows showed in Figure 4.5. One direction to describe a population $f_i(\vec{x}, t)$ of particles at rest.

In one LBM iteration, particles can move from one node (along the directions) to its neighbors. Note that the direction i=0 is defined to describe a population $f_i(\vec{x}, t)$ of particles at rest. The parameters of $\vec{e_i}$ and f_i^{eq} are needed in this model. Eight directions showed in red lines connect with angular points and another twelve directions showed in green lines connect with center of each line. The rest six directions in blue lines connect with center of each surface. So, $\vec{e_i}$ is defined as follows

$$\vec{e_i} = \begin{cases} (0,0,0)\ i = 0 \\ (\pm 1,0,0)c, (0,\pm 1,0)c, (0,0,\pm 1)c\ i = 1,2,3,4,5,6 \\ (\pm 1,\pm 1,0)c, (0,\pm 1,\pm 1)c, (\pm 1,0,\pm 1)c\ i = 7,8,9,10,11,12,13,14,15,16,17,18 \\ (\pm 1,\pm 1,\pm 1)c\ i = 19,20,21,22,23,24,25,26. \end{cases} \tag{4.9}$$

According to [Wolf-Gladrow 2000] and $\vec{u} = 0$, the equilibrium function can be developed as

$$f_i^{eq} = \begin{cases} \frac{8}{27}\rho(\vec{x}, t) & i = 0 \\ \frac{2}{27}\rho(\vec{x}, t) & i = 1,2,3,4,5,6 \\ \frac{1}{54}\rho(\vec{x}, t) & i = 7,8,9,10,11,12,13,14,15,16,17,18 \\ \frac{1}{216}\rho(\vec{x}, t) & i = 19,20,21,22,23,24,25,26. \end{cases} \tag{4.10}$$

4.4.2 Experiments and results

The proposed 3D segmentation method was performed on test image of which size is (100, 100, 100). The main object of this image is a sphere of which center is (50, 50, 50) and radius is 30. The gray level of this object is 150 and the gray level of background is 200 too. Figure 4.6 gives the original images in 2D visualization and the results. The first row, the second row and the third row are the original image and its corresponding result at position (:, :, 10), (:, :, 30) and (:, :, 50).

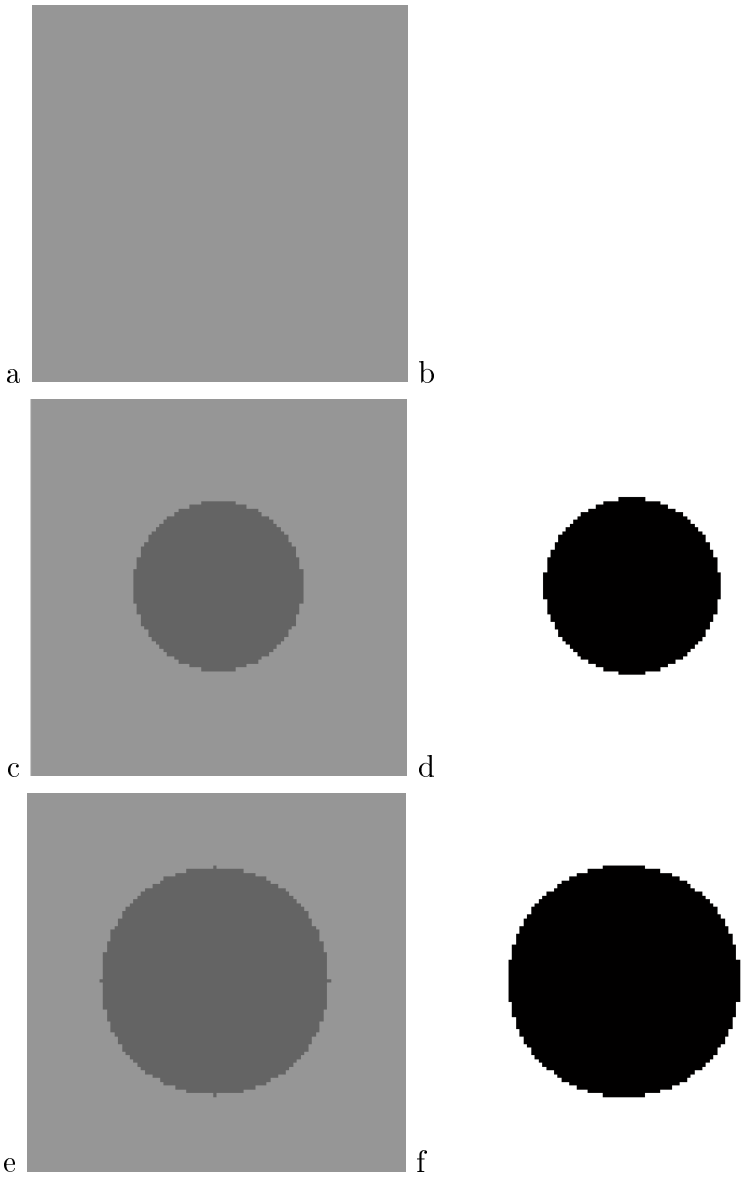

FIGURE 4.6: The original 3D sphere image in 2D visualization in left and its corresponding segmentation results in 2D visualization in right.

4.5 4D model and parameters

4.5.1 The choice of discrete velocity directions

Normally, we implement the LBM with D1Q3 (one dimension and three directions on each node of the lattice); or a square lattice D2Q9 (two dimensions and nine directions on each node of the lattice); or a volume lattice D3Q27 (three dimensions and twenty-seven directions on each node of the lattice).

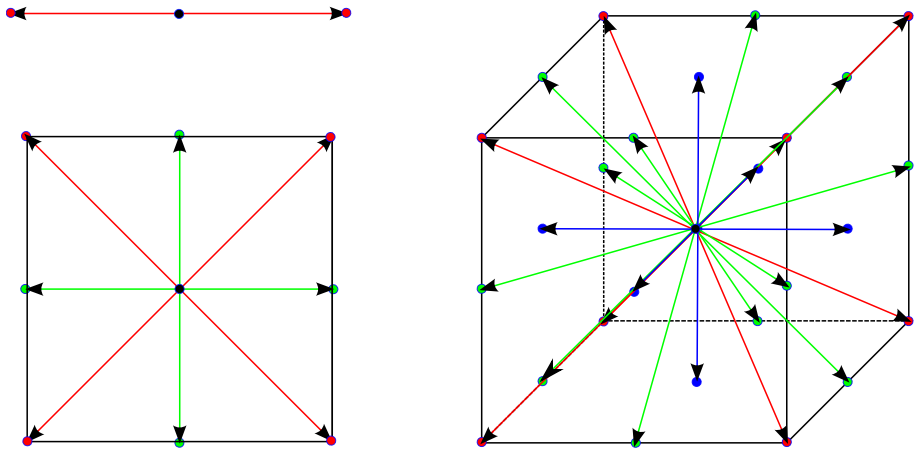

FIGURE 4.7: Geometry of each model and its nodes for D1Q3, D2Q9, D3Q27.

TABLE 4.1: Choice of parameters

Dimension	A	B	C	D	E
1	1	2	0	0	0
2	1	4	4	0	0
3	1	8	12	6	0
4	1	16	32	24	8
N	1	2^n	$C_n^{n-1} \cdot 2^{n-1}$	$C_n^{n-2} \cdot 2^{n-2}$	$C_n^{n-3} \cdot 2^{n-3}$

For D1Q3 model, there are three directions on each node of the lattice. These three directions correspond to three neighborhood nodes: one node is in the center of geometry which has a mark circled in black in Figure 4.7; other two nodes are angular points which have a mark circled in red. D2Q9 model have nine directions on each node corresponding to nine nodes neighborhood: one node is in the center of geometry and has a mark circled in black; other four nodes are angular points which has a mark circled in red; also another four nodes are site in the center of each line which have a mark circled in green in Figure 4.7. For the three dimensional model D3Q27: one node is in the center of geometry and has a mark circled in black too; other eight nodes are angular points which have a mark circled in red; also another 12 nodes are site in the center of each line which have a mark circled in green; besides, six nodes are in the center of the surface and have a mark in blue. As we can see, when we change the geometry from N dimensions to N+1 dimensions, one more type nodes will be needed. The details of LBM model for 1D, 2D, 3D, 4D and nD are shown in table 4.1. A is center of geometry, B is angular points, C is center of line, D is center of surface, E is center of volume.

For 4D segmentation, the LBM model is D4Q81 which contains one node in the center of geometry, 16 nodes in angular, 32 nodes in the center of line, 24 nodes

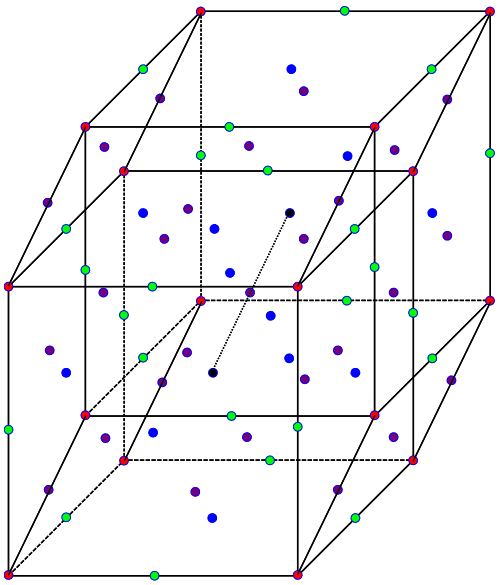

FIGURE 4.8: Four dimension model.

in the center of surface and 8 nodes in the center of volume. In Figure 4.8, the 4D model is formed by two 3D models and the links between these two models. We can see in Figure 4.8, that the two 3D geometries and their mark circles have the same color as shown in Figure 4.7. Between the two 3D models, the purple marks are also need to be added (see the details in Figure 4.8). This D4Q81 model in 4D segmentation with $\vec{e_i}$ is defined as follows

$$\vec{e_i} = \begin{cases} (0,0,0,0)\ i=0 \\ (\pm1,0,0,0)c,(0,\pm1,0,0)c,(0,0,\pm1,0)c,(0,0,0,\pm1)c\ i=1,2,3,4,5,6,7,8 \\ (\pm1,\pm1,0,0)c,(0,\pm1,\pm1,0)c,(\pm1,0,\pm1,0)c,(\pm1,0,0,\pm1)c, \\ (0,\pm1,0,\pm1)c,(0,,0\pm1,\pm1)c \\ i=9,10,11,12,13,14,15,16,17,18,19,20,21,22,23,24,25,26,27,28,29,30,31,32 \\ (\pm1,\pm1,\pm1,0)c,(\pm1,0,\pm1,\pm1)c,(\pm1,\pm1,0,\pm1)c,(0,\pm1,\pm1,\pm1)c \\ i=33,34,35,36,37,38,39,40,41,42,43,44,45,46,47,48, \\ 49,50,51,52,53,54,55,56,57,58,59,60,61,62,63,64 \\ (\pm1,\pm1,\pm1,\pm1)c \\ i=65,66,67,68,69,70,71,72,73,74,75,76,77,78,79,80. \end{cases} \tag{4.11}$$

Meanwhile, the equilibrium function can be developed as follows

$$f_i^{eq} = \begin{cases} \frac{2}{9}\rho(\vec{r},t) & i = 0 \\ \frac{1}{36}\rho(\vec{r},t) & i = 2,3,...,8 \\ \frac{1}{108}\rho(\vec{r},t) & i = 9,10,...,32 \\ \frac{1}{144}\rho(\vec{r},t) & i = 33,34,...,64 \\ \frac{1}{144}\rho(\vec{r},t) & i = 65,66,...,80. \end{cases} \tag{4.12}$$

4.5.2 Evaluation criteria

The results are evaluated by comparing the proposed segmentation with the perfect segmentation. Also, they are calculated by using the "Dice coefficient" defined as the fraction of the intersection of A and B to sum of them [Dice 1945].

$$Dice = \frac{2\,|A \cap B|}{|A| + |B|} \times 100\% \tag{4.13}$$

where A represents the area obtained by using each method and B is the area prescribed by the radiologist. | | denotes the number of pixels in corresponding area. The bigger the Dice coefficient is, the better the segmentation result is. We can see that a value of 1 indicates perfect overlap, and a value of 0 means no overlap at all. Moreover, the coefficient of variation (CV) is calculated, which is a statistical measure of the precision of segmentation.

$$CV = \frac{s}{\mu} \times 100\% \tag{4.14}$$

where s represents standard deviation and μ is mean value.

4.5.3 Experiments and results

The proposed 4D segmentation method was performed on test image of which size is (40, 40, 40, 40). The main object of this image is a hypersphere of which center is (20, 20, 20, 20) and radius is 15. Then, we add 10% random noise in hypersphere image as a new test image. More precisely, we increase the random noise from 30% to 300% in another 8 hypersphere images. Our proposed method was validated on all 10 hypersphere images containing one image without noise

and nine images with different level of random noise. Figure 4.9 illustrates result of segmentation of hypersphere image without noise using the proposed method.

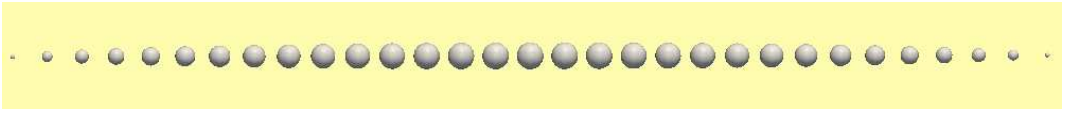

FIGURE 4.9: Result of hypersphere image without noise using the proposed method.

As we can observe, the hypersphere is well segmented by our proposed method. Also, we apply our method on another 9 images are with different random noise, 10%, 30%, 50%, 70%, 100%, 150%, 200%, 250%, 300%, respectively.

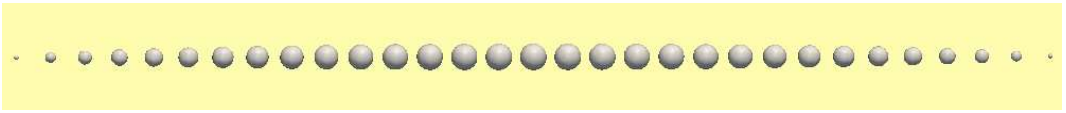

FIGURE 4.10: Result of hypersphere image with 70% random noise using the proposed method.

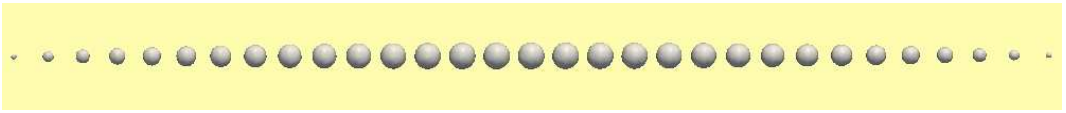

FIGURE 4.11: Result of hypersphere image with 100% random noise using the proposed method.

FIGURE 4.12: Result of hypersphere image with 300% random noise using the proposed method.

Obviously, the obtained results in Figure 4.12 are very similar to Figure 4.10. After we added 70% random noise, the results didn't change a lot. In consequence, the proposed method has a high ability to prevent noise. When the noise came to 300%, the results changed especially in the beginning of Figure 4.12. In order to see the difference clearly, we zoom in this part.

More precisely, we analyzed our results quantitatively. We defined the hypersphere which means we could have the prefect contour. The comparison between our segmentation results and the perfect contour is shown in Figure 4.14. We illustrate the Dice values of ten 4D hypersphere images with different random

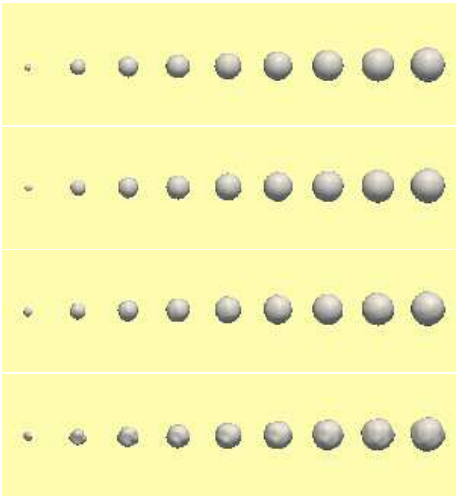

FIGURE 4.13: Part of results without noise and with 50%, 150% and 300% random noise using the proposed method.

noise in red. For each 4D image, we selected several 3D samples from 4D image and we calculated the value of Dice for each 3D sample. With the help of these samples, we obtained the average value of Dice and the value of CV for each 4D image which is shown in Figure 4.14 the green bar-graph and yellow bar-graph. As can be observed, we have better segmentation results with random noise from 0% to 200% than from 200% to 300% since the Dice values are greater. Even we increased the random noise to 300%, the value of Dice and average of Dice are still high. The results show that the proposed 4D segmentation method could generate hypersphere outlines close to the perfect contour even with high level of noise.

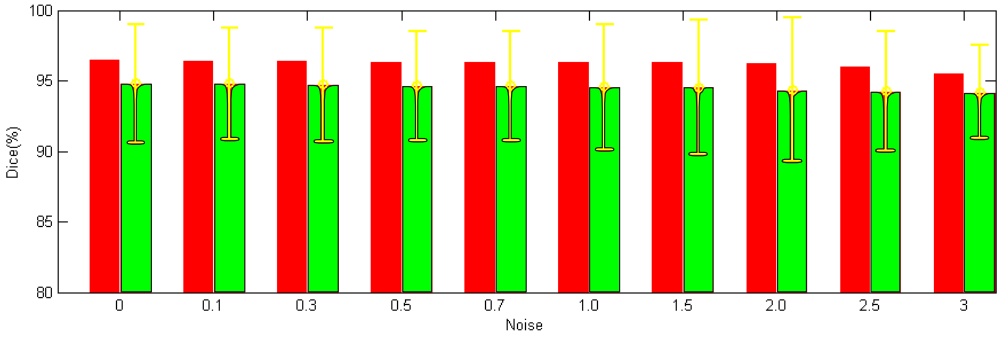

FIGURE 4.14: Dice, average of dice and its corresponding CV of each image. The bar-graph in red, green and yellow represent dice, average of dice and CV.

4.6 Conclusion

A LBM based segmentation method is proposed in this chapter. The contribution of this chapter is that we propose a way using LBM in image processing and LBM anisotropic diffusion model is presented, followed with LBM anisotropic diffusion segmentation model. Also, we give the evolution function and its corresponding parameters in 2D, 3D and 4D. Comparisons between test images like circle, sphere and hypersphere segmentation results and perfect contour prove that the proposed segmentation models are accurate. In the future, we would like to use the proposed models to specific cases and to solve real medical problems.

Chapter 5

Segmentation of giant cerebral aneurysms using LBM

Abstract

The segmentation of giant aneurysms of the brain from computed tomography angiography (CTA) imaging remains a challenge. This is mainly due to the fact that giant aneurysms consist of two parts: the lumen appearing as a focal object and the thrombus which has a low contrast compared to neighboring tissues, which makes it difficult to obtain the manual or automatic segmentation. In this chapter, we propose a segmentation methodology based on the combined use of the LBM and the level set method. The first methodology consists in extracting the group consisting of lumen and thrombus using a procedure in two steps, then refining the shape of the thrombus using the level set method. The experiments are performed on 258 slices of 8 patients CTAs with different types of giant aneurysms. The results on real images showed that the proposed method is comparable to manual segmentation, and quantitatively, the matching factors obtained using the proposed method are high, demonstrating good accuracy of the segmentation .

Résume

La segmentation des anévrismes cérébraux géants à partir d'imagerie scanner angiographique reste un défi. Ceci est principalement du au fait que les anévrismes géants sont constitués de deux parties: la lumière apparaissant comme un objet focal et le thrombus qui possède un faible contraste par rapport aux tissus voisins et qui rend la segmentation manuelle ou automatique difficile. Nous proposons une méthodologie de segmentation basée sur l'utilisation combinée de la méthode de Boltzmann sur réseau et de la méthode des courbes de niveaux. La méthodologie consiste d'abord à extraire l'ensemble constitué de la lumière et du thrombus en utilisant une procédure en deux étapes, puis à affiner la forme du thrombus en utilisant la méthode des courbes de niveaux. Les expériences sont effectuées sur 258 tranches des scanners de 8 patients contenant différents types d'anévrismes géants. Les résultats sur des images réelles ont montré que la méthode proposée est comparable à la segmentation manuelle, et que quantitativement, les facteurs de ressemblance obtenus en utilisant la méthode proposée sont élevés, ce qui démontre une bonne précision de la segmentation.

5.1 Introduction

An aneurysm is an abnormal bulging outward of an artery [Seibert 2011]. Because of certain histopathologic and hemodynamic factors, aneurysms most commonly occur in arteries that supply blood to the brain [Vega 2002]. Cerebral aneurysm is one of the most serious diseases forming part of the stroke, and it is estimated to occur in 1 to 6 percent of the population. Also, up to 85 percent of subarachnoid hemorrhages [Wiebers 2003], which are potentially lethal events with mortality rate as high as 50 percent are caused by the rupture of cerebral aneurysms [Currie 2011, Hop 1997].

Computed tomography angiography (CTA) plays an essential role in the diagnosis, treatment evaluation, and monitoring of cerebral aneurysms. It allows us to detect narrowing or obstruction of blood vessels in time so that corrective therapy can be done, and it can also detect the minest changes in the vessel structure and anatomy. In addition, CTA images may give more precise anatomical details than either ultrasound or magnetic resonance images (MRI), particularly for small blood vessels. Now, CTA is becoming the radiological examination of choice for blood vessels diseases.

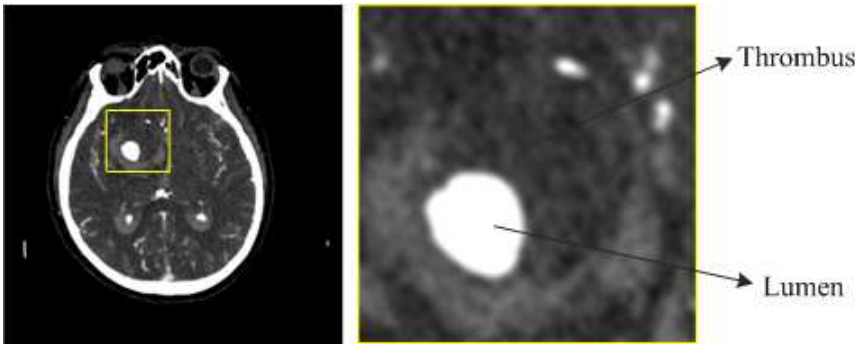

FIGURE 5.1: Example of an aneurysm image: lumen appearing as a focal object, thrombus as a diffuse object.

Segmentation of aneurysm images in CTA is fundamental for the quantitative measurement and assessment of aneurysms. Most CTA images of cerebral aneurysms (see Figure 5.1) exhibit the particularity of presenting not just the lumen (appearing as a focal object), but also its associated thrombus which appears as a diffuse object (with low-contrast with respect to neighboring tissues, which renders their manual or automatic delineation difficult) connected to the lumen. In the past, a number of works have been devoted to the segmentation of CTA images.

[De Bruijne 2003] used an active shape model for segmenting lumen and thrombus in abdominal aortic aneurysms from CTA data. [Olabarriaga 2004] proposed to segment lumen with a simple gray level model and used a gray level modeling approach with a non-parametric pattern classification technique to segment thrombus. In [Dehmeshki 2009], a computer-aided detection system was introduced to detect the lumen and thrombus.

All the methods mentioned above dealing with abdominal aortic aneurysms segmentation and there is some literature about the segmentation of cerebral aneurysms also, which viewed the lumen as a whole aneurysm [Kostopoulos 2007, Lesage 2009, Lauric 2010]. An algorithm segmenting cerebral aneurysm based on implicit deformable models combined with non parametric region-based information was proposed in [Hernandez 2003]. Another cerebral aneurysm segmentation method combining the level set with geodesic active surfaces was addressed in [Firouzian 2011]. More recently, [Chen 2014] proposed to segment cerebral aneurysms by solving the geodesic active contours (GAC) [Caselles 1997] equation using lattice Boltzmann method (LBM); the method is by essence a semi-automatic segmentation method in which a prior contour of the aneurysm is needed for initialization. Despite these works, the segmentation of cerebral aneurysms remains difficult because the objects to be segmented are not just the focal lumen, but also its associated thrombus having irregular and diffuse frontiers. Figure 5.2 shows some examples of segmentation of cerebral aneurysm using conventional methods such as snake model [Kass 1988] and level set model [Osher 1988]. We observe clearly that the wall of the aneurysm is not well segmented because the thrombus is a diffuse region, whose boundary is very difficult to define.

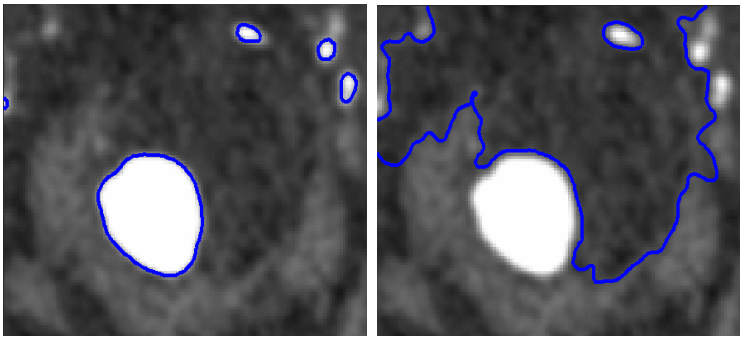

FIGURE 5.2: Left: lumen segmentation with snake model. Right: thrombus segmentation with level set model.

The present chapter focuses on the fully automatic segmentation of both lumen and thrombus of cerebral aneurysms. To this end, we propose a multilevel segmentation

methodology based on the combined use of LBM and level set technique to segment the lumen and the thrombus. In this framework, the LBM anisotropic diffusion segmentation method is used to image segmentation problems. More precisely, we first segment the lumen of the cerebral aneurysm by using the LBM. After the lumen is segmented, we then perform the segmentation of the thrombus with the aid of a different LBM configuration coupled with level set technique to refine the shape of the thrombus.

The rest of this chapter is organized as follows. Firstly, we present the proposed segmentation methodology and the fundamentals of the level set method briefly. Experiments and results are given later, followed by conclusion section.

5.2 Segmentation methodology

The proposed methodology consists in first performing multilevel segmentation of aneurysm (both lumen and thrombus indicated in Figure 5.1) using LBM and then refining the contour of thrombus using level set technique, as schematized in Figure 5.3 and Figure 5.4. More precisely, our proposed method uses LBM to segment lumen part directly from the original image. Then, after gray level replacement, LBM and expanding disc are used to obtain aneurysm presenting a circle contour. After this, we use level set with ellipse by taking the circle contour from last step as the initial contour to obtain the final aneurysm contour. Finally, we implement Boolean operation on final aneurysm contour with lumen part obtained from first step to get our final thrombus contour.

5.2.1 LBM segmentation algorithm

We propose the following segmentation method to segment both lumen and thrombus based on LB equations. By using a parameter T calculated from the Otsu technique [Otsu 1975], we first detect lumen. Then, we take the detected lumen as a mask to paste on the original images. After that, inside the mask region, we replace the gray levels of the original image by the mean value of pixels outside the masked region. This operation discards the lumen of the original image. Then we apply LBM segmentation again on the new image with a different parameter, thus yielding an image region containing the thrombus. At this stage, we cannot

get the thrombus itself since it is a diffuse object, whose boundary is very difficult to define. To cope with this problem, we introduce a disk placed at each pixel of the region of interest (ROI) of the image and expand it. The disk expansion is stopped according to the criterion defined by

$$s = \frac{disk \cap 2^{nd}\ LBM\ image}{disk} \tag{5.1}$$

where 2nd LBM image is the image after the second LBM segmentation (see Figure 5.4).

After that, we take the obtained biggest region circled by the expanding disk as the region containing both lumen and thrombus. Finally, the results obtained by subtracting the segmentation calculated by LBM from the expanding disk give an estimation of the shape of the thrombus and allow us to estimate the original geometry of the aneurysm.

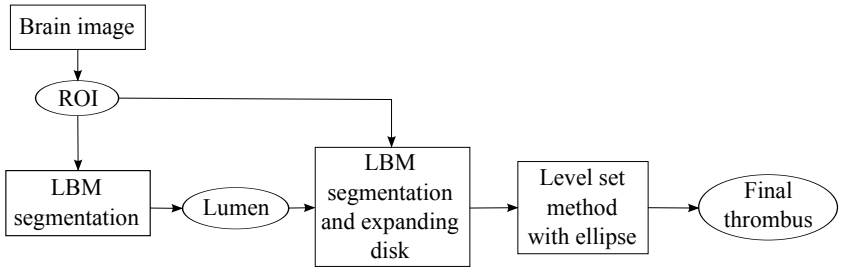

FIGURE 5.3: Overview of the proposed multilevel segmentation scheme.

Now, we use level set model with ellipse to refine the results calculated above by LBM. The edges obtained by "expanding disk" are chosen to be the initial contours for level set model and then we evolve equation (5.3) on the 2nd LBM image (see Figure 5.4) to get the final contours. The detailed flow is shown in Figure 5.4.

5.2.2 Level set segmentation

We can segment the lumen and part of boundary of thrombus after LBM segmentation. Then we use "expanding disk" to get the whole aneurysm which is a circle-like contour.

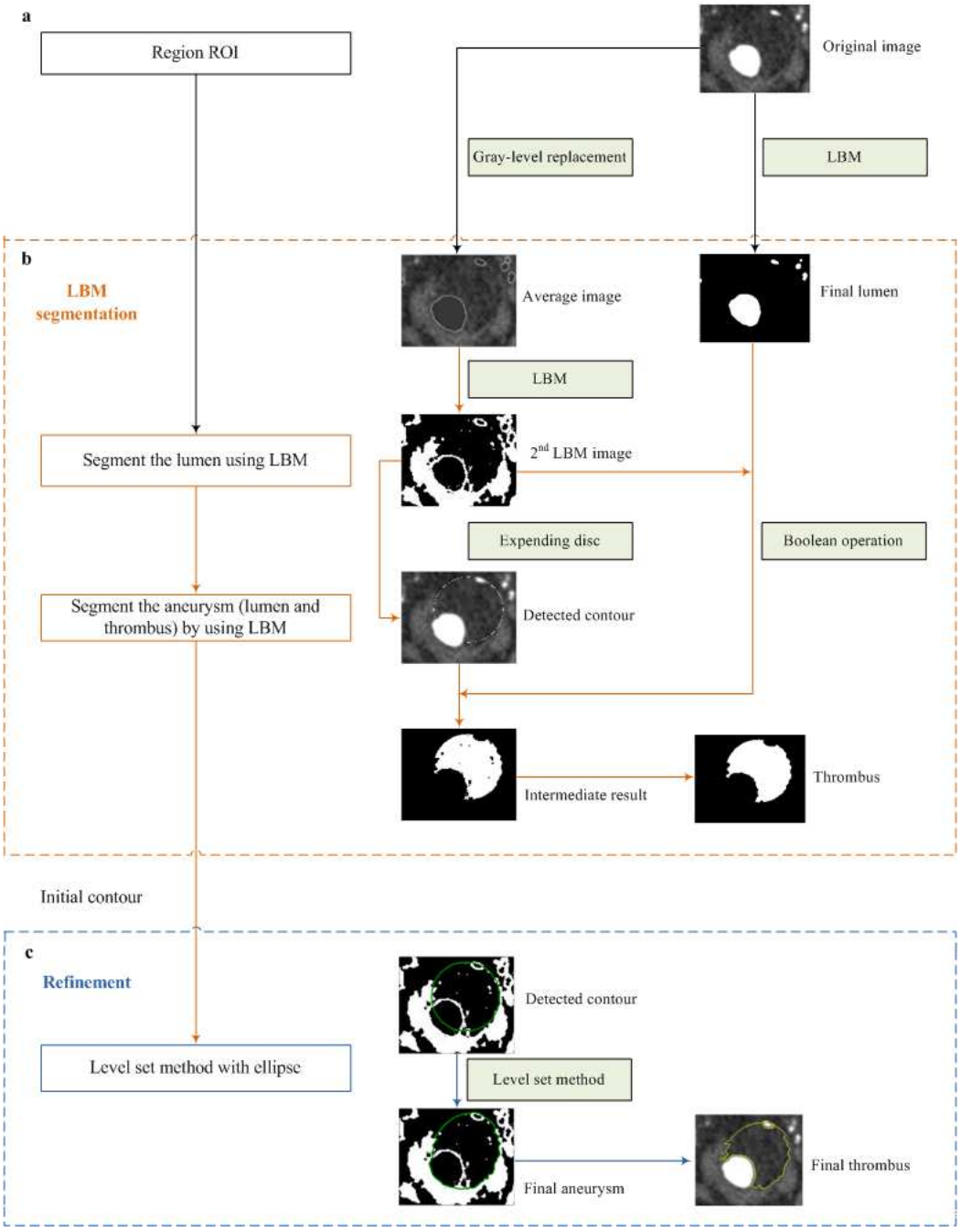

FIGURE 5.4: Lumen and thrombus multilevel segmentation scheme. The scheme consists of three blocks: a. ROI region choice; b. LBM segmentation of the entire aneurysm step by step as shown by the yellow frame; c. Thrombus contour refinement using level set technique.

5.2.2.1 General level set formulation with shape priors

Since we are addressing the segmentation of aneurysm, which is bounded by ellipse-like contours, we are led to use the level set with shape priors to refine our segmentation. Introducing shape priors in the level set formulation is an

interesting idea; a number of techniques have been reported in the literature [Bernard 2009, Delgado-Gonzalo 2012]. As in [Alessandrini 2011] we adopt the following general expression for the energy function

$$E = E_{data} + \alpha E_{shape} \tag{5.2}$$

where E_{data} represents the chosen data attachment term and E_{shape} embeds the shape prior. The weight α corresponds to a positive hyper-parameter that balances the influence between the two terms. The expression for the two energy terms adopted for the segmentation task is presented as follows.

In order to perform segmentation with shape priors, the level set evolves according to the equation [Osher 1988]

$$\frac{\partial \phi(\vec{x})}{\partial \tau} = \delta(\phi(\vec{x}))[f(x) + \alpha g(\vec{x}, \lambda)] \tag{5.3}$$

where ϕ is a Lipschitz-continuous function, $f(\vec{x})$ the data attachment term given in (5.15), δ the Dirac delta function and $g(\vec{x}, \lambda)$ the shape prior term defined in (5.21). The choice of the weight coefficient α depends on the specific application. In general, a higher α value is chosen in order to put more importance on the shape prior term when the quality of image is poor, and the result will be closer to an ellipse. In the present study, we have chosen $\alpha = 0.7$ which gives the best segmentation result.

5.2.2.2 Basic level set formula

The moving fronts of level set formulation, denoted by C, are represented by the zero level set $z = \{\vec{x} | \phi(\vec{x}) = 0\}$ of a level set function $\phi(\vec{x}) = 0$. Let Ω be a given d-dimensional image and C is represented as the zero level set of a Lipschitz-continuous function $\phi(\vec{x})$ of dimension d+1 that satisfies as follows

$$\begin{cases} \phi(\vec{x}) < 0 & \vec{x} \in \Omega^-, \\ \phi(\vec{x}) = 0 & \vec{x} \in C, \\ \phi(\vec{x}) > 0 & \vec{x} \in \Omega^+. \end{cases} \tag{5.4}$$

where $\phi(\vec{x})$ Lipschitz-continuous function, $\vec{x}$ the position in the given image. Ω^- is the region inside of C and Ω^+ is the region outside of C. C is the zero level set

of $\phi(\vec{x})$. This relationship can be described in Figure 5.5. The curve of $z = 0$ is the zero level set of $\phi(\vec{x})$ function.

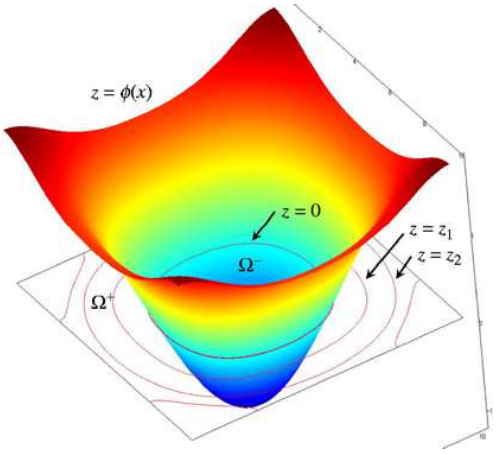

FIGURE 5.5: Example of level set function. The zero level is represented as $z = 0$.

If the curve C moves with a speed $\phi(\vec{x})$, the evolution equation of the level set function can be written in the following

$$\frac{\partial \phi}{\partial \tau}(\vec{x}) = f(\vec{x})\delta(\phi(\vec{x})) \tag{5.5}$$

The problem of segmenting one object from the background is handled by the evolution of one level set driven by minimization of a specific energy criterion. Its steady state partitions the image into two regions that delimit the boundaries of the object to be segmented. At this stage, E_{data} could be any of the data attachment terms, and we adopt as data attachment term the localized version of the Chan-vese model [Chan 2000]. The minimization of E_{data} with respect to ϕ leads to the level set equation (5.5) with $f(\vec{x})$ given by

$$f(\vec{x}) = \int_{\Omega} B(\vec{x}, \vec{y})\delta(\phi(\vec{y}))[(I(\vec{y}) - u_x)^2 - (I(\vec{x}) - v_x)^2]d\vec{y} \tag{5.6}$$

$$B(\vec{x}, \vec{y}) = \begin{cases} 1 & if\ \vec{y} \in N(\vec{x}) \\ 0 & otherwise \end{cases} \tag{5.7}$$

where $\vec{y}$ is a spatial variable and $N(\vec{x})$ corresponds to a user-defined neighborhood at point $\vec{x}$. The quantities u_x and v_x correspond to the localized version of the inside and outside average intensity values measured in the window $N(\vec{x})$.

5.2.2.3 Annular shape with ellipse

We introduce an annular shape constraint into our level set framework by minimizing the following energy criterion

$$E_{shape}(\phi, \lambda) = \int_{\Omega} (\phi(\vec{x}) - \phi_e(\vec{x}, \lambda))^2 \delta(\phi(\vec{x})) d\vec{x} \tag{5.8}$$

$$\phi_e(\vec{x}, \lambda) = \frac{F(\vec{x}, \lambda)}{[\bigtriangledown F(\vec{x}, \lambda)]} \tag{5.9}$$

$$F(\vec{x}, \lambda) = \lambda_1 x^2 + \lambda_2 xy + \lambda_3 y^2 + \lambda_4 x + \lambda_5 y + \lambda_6 \qquad with \lambda_2 < 4\lambda_1\lambda_3 \tag{5.10}$$

where $\phi_e(\vec{x})$ is Sampson distance function representing the Sampson distance of a point $\vec{x}$ from the annular shape defined by the parameter λ [Alessandrini 2011]. The function $F(\vec{x}, \lambda)$ corresponds to the algebraic distance of a point $\vec{x} = (x, y)$ to an ellipse, and is represented by the standard quadratic equation for conic sections. The following equations are obtained based on the fact that we can get the minimization of energy by finding the geodesic zero level set

$$\frac{\partial \phi}{\partial \tau} = g(\vec{x}, \lambda)\delta(\phi(\vec{x})) \tag{5.11}$$

$$g(\vec{x}, \lambda) = -2(\phi(\vec{x}) - \phi_e(\vec{x}, \lambda)). \tag{5.12}$$

The results obtained by level set with a shape prior method are presented in Figure 5.6. We can see that Figure 5.6b is not yet segmented since the initial contour is not very similar to aneurysm. It implies that, choosing appropriately the initial points is an important aspect of this method. Accounting for such feature, we propose to tackle segmentation problems using the LBM and level set methods.

5.3 Experiments and results

5.3.1 Patient data

The proposed aneurysm segmentation method was performed on 258 slices of the 3D CTA scans of 8 patients from the Montpellier CHU (data base of the Thrombus project $N°$ FP7-ICT-2009-6-269966). These eight cases can be divided into three kinds: aneurysms with big thrombus, aneurysms with small thrombus and aneurysms having no thrombus. Figure 5.7 shows the three types of aneurysms

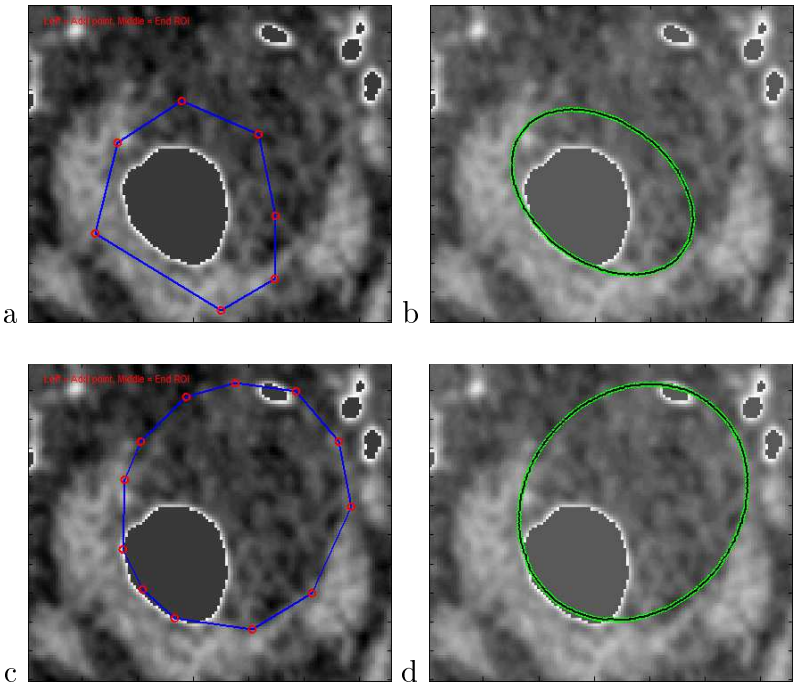

FIGURE 5.6: Example of aneurysm segmentation using level set with shape priors. a. Initial points arbitrarily chosen. b. The obtained aneurysm contour. c. Initial contour chosen to be similar to the aneurysm contour. d. A better aneurysm contour obtained.

and the white box is the ROI chosen by clinical doctors. The brightest part in white box is the aneurysm lumen and the darkest part is its associated thrombus. After that, our proposed method was validated on all 35 slices from patient 5 and another 19 slices arbitrarily chosen among the 223 slices from the remaining patients.

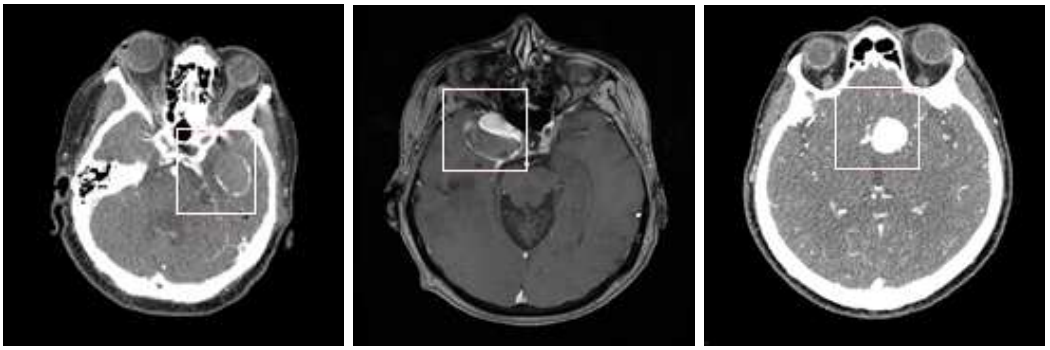

FIGURE 5.7: Three kinds of aneurysms. Left: Aneurysm with big thrombus; middle: aneurysm with small thrombus; right: aneurysm formed no thrombus.

5.3.2 Evaluation criteria

The accuracy of the proposed segmentation was assessed using the segmentation matching factor (SMF) defined as the ratio of the intersection of A and A_{rad} to union of them [Betal 1997]:

$$SMF = \frac{A \cap A_{rad}}{A \cup A_{rad}} \times 100\% \tag{5.13}$$

where A represents the area obtained using our method and A_{rad} is the area prescribed by the clinical doctors. The bigger the SMF value, the better the segmentation. Moreover, the coefficient of variation (CV) was also calculated, which is a statistical measure of the precision of segmentation.

$$CV = \frac{d}{\mu} \times 100\% \tag{5.14}$$

where d represents standard deviation and μ is mean value.

5.3.3 Results

Figure 5.8 illustrates the intermediate results of the proposed multilevel segmentation. As observed, after the first LBM segmentation, an unwanted small object is present in addition to the segmented lumen (Figure 5.8b). In the 2nd LBM segmentation (Figure 5.8d), as a whole entity, the object "lumen and thrombus" which represents the aneurysm is well brought out, especially for its bottom left part. We also remark that some parts of the aneurysm are missing due to the fact that the gray levels of the thrombus are very close to those of its neighboring tissues in these regions. We see that the aneurysm, superimposed on the original image, was fairly delineated after disk expanding but that the circle-like contour is somewhat too idealized with respect to the reality. Moreover, the circle-like contour does not cover the whole darker region representing the aneurysm.

In these computations, the parameter T was 153, which was obtained by using Otsu technique. The result in Figure 5.8b was obtained from Figure 5.8a after LBM iterations. The result in Figure 5.8d was obtained from Figure 5.8c after LBM iterations. A threshold value of 0.94 for the disc expansion criterion s was used, which is a good choice to integrate both the lumen and the thrombus. Details about the choice of other parameters are given in Table 5.1.

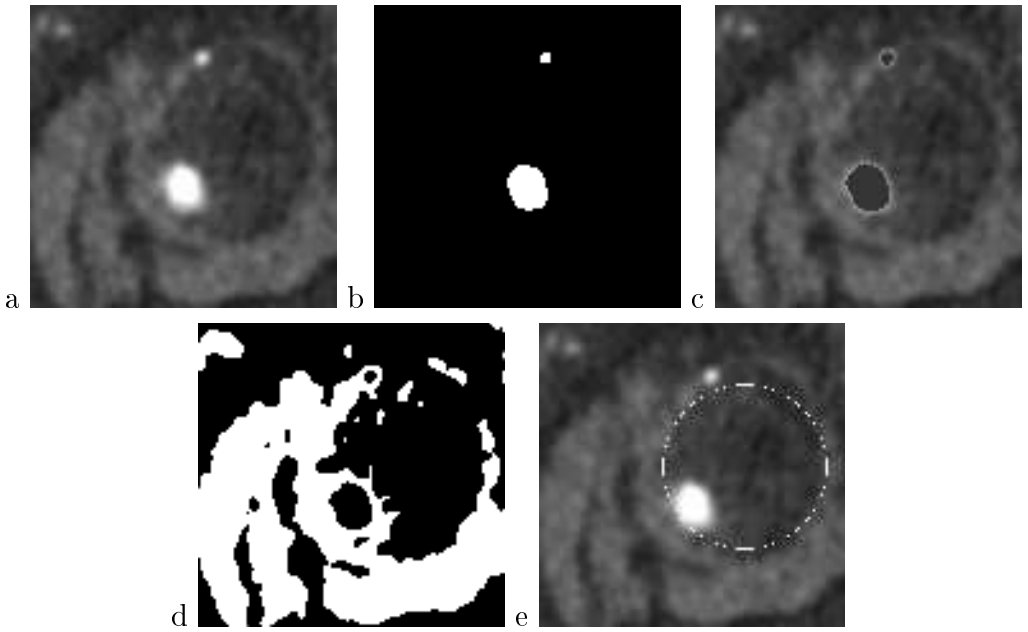

FIGURE 5.8: Results from each step of the proposed multilevel segmentation scheme. a. Original image; b. First segmentation of the lumen; c. Average image; d. 2^{nd} LBM image; e. Detected contour.

TABLE 5.1: Choice of LBM parameters

$g_i(\vec{x}) = \frac{1}{\left[1+\frac{\lvert G*\rho(\vec{x},t)-G*\rho(\vec{x}+\vec{e}_i\Delta t,t)\rvert}{10}\right]^2}$
$G\ is\ gaussian\ function:\ G(0,1)\ \tau = 1$
$T\ for\ lumen\ segmentation\ T = 153$
$T\ for\ aneurysm\ segmentation\ T = 72$
$Centre\ and\ radius\ of\ circle:\ (57,81),\ r = 32$

Using the circle-like contour as initial contour of the level set segmentation with ellipse, we obtain more realistic contours of the aneurysm (Figure 5.9). Figure 5.9a represents the result obtained with $\alpha = 0$, which amounts to using the traditional level set segmentation. Obviously, the obtained contour deviates far from the aneurysm contour by the presence of multiple contours and contour leakage in the upper right black area. Generally, when $\alpha < 0.6$, the influence of "ellipse factor" becomes smaller, which makes the final contour not so smooth and leads to contour leakage. In another extreme case with $\alpha \geq 0.9$ (Figure 5.9b), the contour becomes a very regular ellipse which does not fit well the actual contour of the aneurysm. The best contour was obtained with intermediate α values (Figure 5.9c), where the approximate elliptical contour of aneurysms was well segmented. By superimposing the final contour on the original image (Figure 5.9d), we clearly

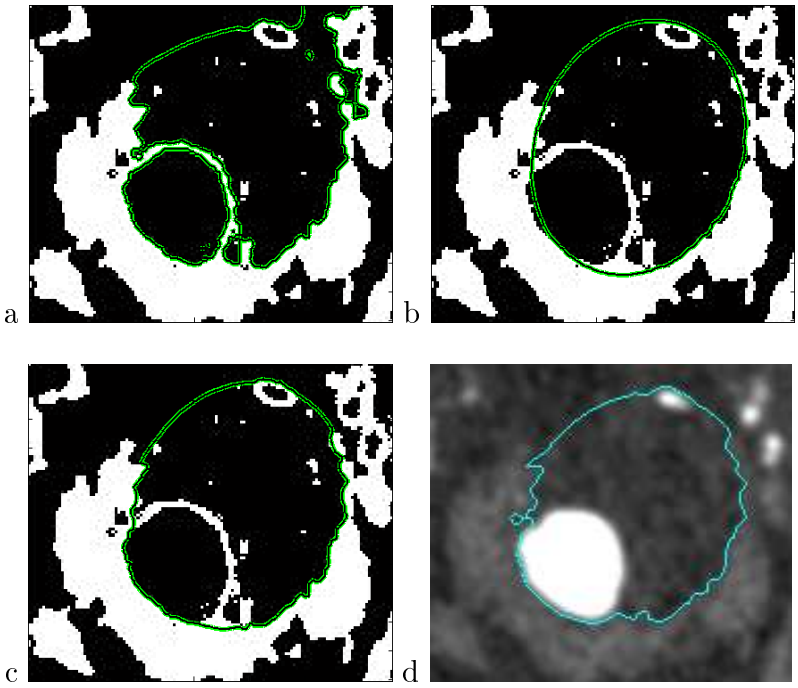

FIGURE 5.9: Refinement of aneurysm contours using level set method with ellipse. a. Using $\alpha = 0$. b. Using $\alpha = 1$. c. Using $\alpha = 0.7$. d. The final aneurysm contour superimposed on the original image.

see that the final contour follows the irregular variation of the actual contour of the aneurysm, and occupies the whole darker region corresponding to the aneurysm, without any false multiple contours and contour leakage phenomenon. After segmenting the lumen contour (Figure 5.10, first row) and aneurysm contour (Figure 5.10, middle row) using the above-explained method, the thrombus contour is obtained through a Boolean operation (Figure 5.10, bottom row).

Then, we applied the above-illustrated segmentation algorithm to 35 slices containing the ROI shown in Figure 5.7 from patient 5. To evaluate the multilevel segmentation method, all the 35 slices were manually segmented by clinical doctors. The comparison between automatic and manual segmentation is shown in Figure 5.11. In Figure 5.11, we illustrate the SMF values of 35 ROIs. As can be observed, we have greater SMF values in the middle of the slices than in the top and bottom. From 11th to 23th slices, the aneurysm was better segmented since their SMF values are greater than the average SMF (the average SMF value of the 35 slices is 88.05%). For slices in the top and bottom, the aneurysm was also well segmented since SMF values are still high and the contours of aneurysms are close to manual results. The results showed that the automatic multilevel segmentation method could generate aneurysm outlines close to those given by the manual

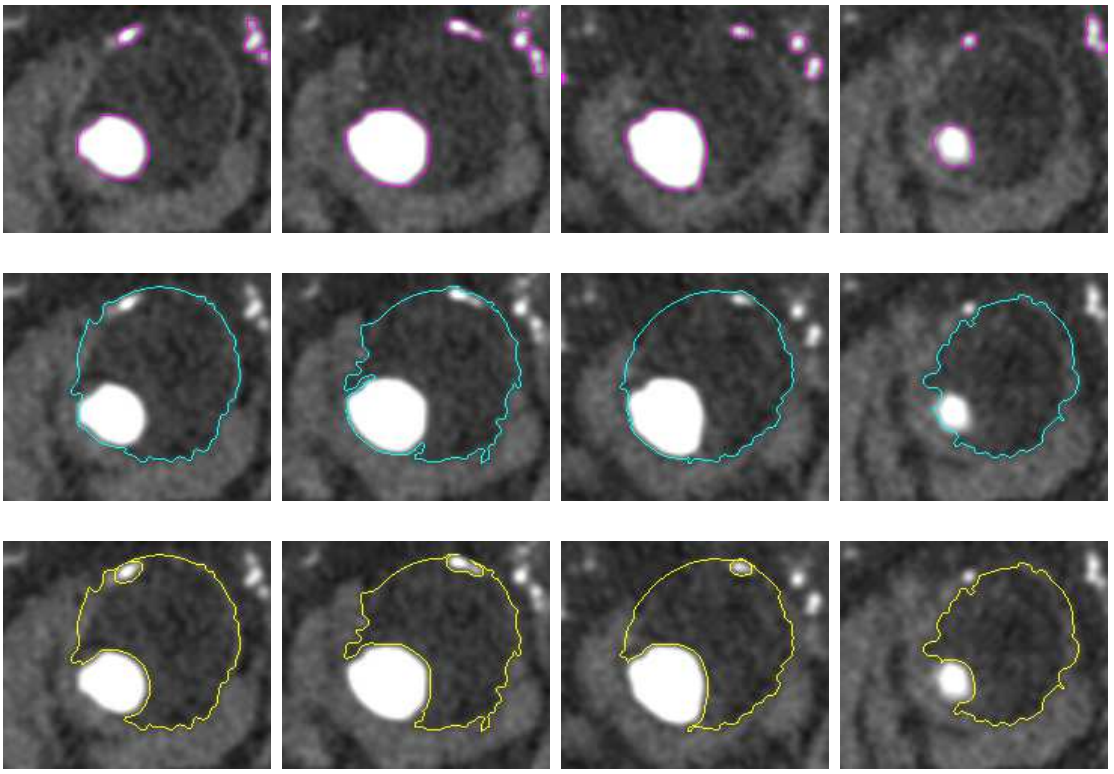

FIGURE 5.10: Comparison of the lumen contours obtained using the LBM, the refined aneurysm contour using the level set method, and the so-derived thrombus contours. First row: lumen contours. Middle row: Aneurysm contours. Bottom row: Thrombus contours. The columns from left to right represent respectively the 95^{th}, 99^{th}, 106^{th} and 110^{th} slices in patient 5.

delineation.

More precisely, we applied the proposed segmentation algorithm to the other 223 images corresponding to the other 7 patients. To evaluate the automatic segmentation, 19 slices were arbitrarily chosen among the 223 slices for manual segmentation by clinical doctors and 2 slices were arbitrarily chosen among the 35 slices in Figure 5.11. Examples of automatic and manual segmentation are shown in Figure 5.12. As can be observed (Figure 5.12a to Figure 5.12d), the aneurysms were well segmented since the contours of the segmented aneurysms are very close to manual results. The automatic segmentation of the images shown in Figure 5.12e to Figure 5.12h were more difficult, but the results are acceptable for clinical doctors since the lumen has been segmented in the first step of the algorithm, the thrombus is segmented by Boolean operation between the aneurysm and lumen, which makes that the inaccuracy in Figure 5.12e to Figure 5.12h was discarded. Indeed, for instance in the case of Figure 5.12e to Figure 5.12h, the automatic results are still close to the manual results. This can be observed from the quantitative results

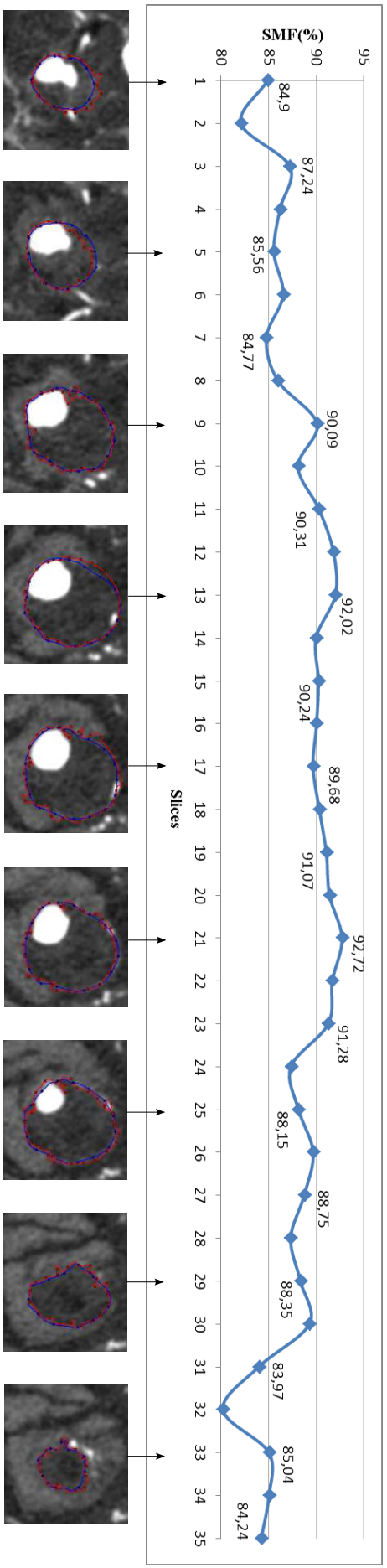

FIGURE 5.11: Comparison of SMF values of 35 slices. The red contour correspond to the proposed automatic segmentation and the blue contour correspond to the manual segmentation.

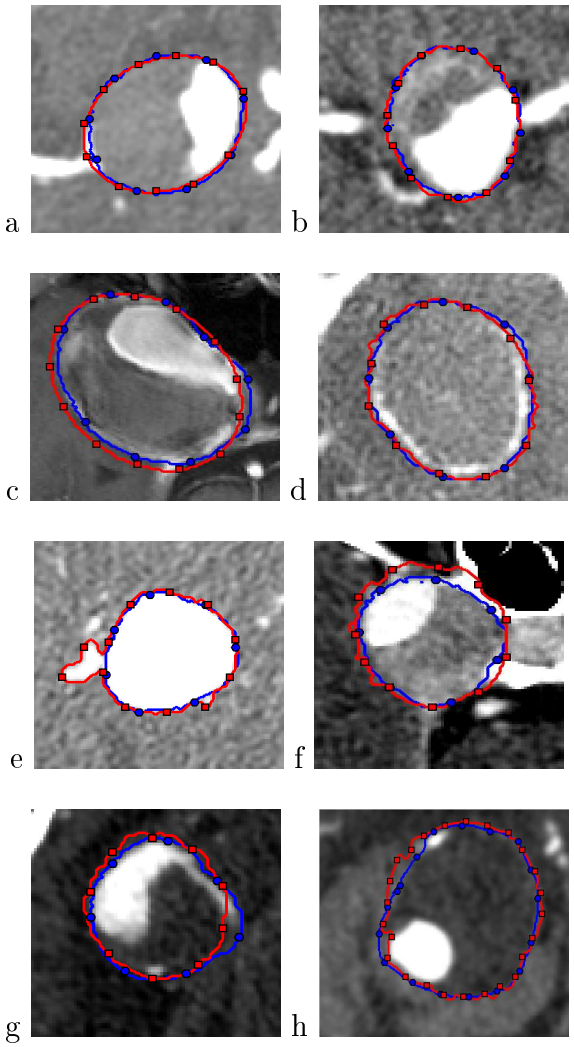

FIGURE 5.12: Results of segmentation of aneurysms. The red contour (with small squares) correspond to the proposed automatic segmentation and the blue contour (with small circles) to the manual segmentation.

given in Table 5.2. The SMF values in Figure 5.12e to Figure 5.12h are still high in comparison with the cases of Figure 5.12a to Figure 5.12d. With respect to the manual segmentation, the over-estimation in Figure 5.12e and Figure 5.12f (SMF=83.89%) and the under-estimation in Figure 5.12g (SMF=82.48%) of the aneurysm lead to a SMF value of 88.37%.

In short, the results showed that the automatic multilevel segmentation method generates the aneurysms outlines close to those given by the manual delineation (SMF = 88.37%). To quantitatively assess the accuracy and reproducibility of each method, the CV of SMF values were calculated. The proposed method gave a good result since it exhibited the smallest variability in segmentation.

TABLE 5.2: SMF values calculated from 21 images arbitrarily chosen among the 258 images corresponding to the 8 patients.

Image	**SMF%**	**Image**	**SMF%**
1	83.38	**2**	88.72
3	87.39	**4**	89.57
5	80.83	**6**	81.44
7	93.95	**8**	85.30
9	79.66	**10**	85.28
11	89.47	**12**	94.44
13	92.33	**14**	92.23
15	91.22	**16**	91.28
17	91.96	**18**	84.46
19	92.43	**20**	93.75
21	86.64		
Mean Value		88.37	
Deviation		4.473	
CV %		5.062	

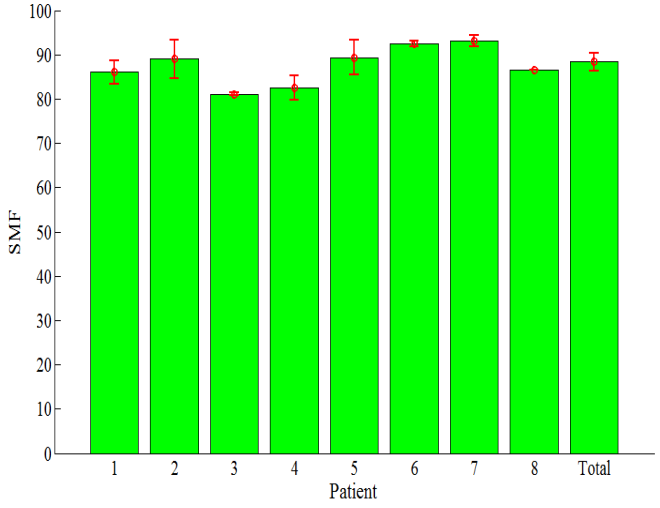

FIGURE 5.13: Mean and standard deviation of SMFs of each of the 8 patients. The bar-graph represents the mean and standard deviation of the 8 patients.

In Table 5.3, we show the comparison of mean, standard deviation and CV of SMF values between the 8 patients. Our method gives results very close to the manual segmentation for the patients 2, 5, 6 and 7 (SMF $\geq$ 89%). For the other patients, the proposed method also generated great SMF values (SMF $\geq$ 79.60%). Figure 5.13 shows more visually the segmentation performance of the proposed method

TABLE 5.3: Comparison of mean, standard deviation, and CV of SMF values between the 8 patients.

Patient	Mean Value	Deviation	CV%	Figure 5.12
1	86.05	2.670	3.103	c
2	89.05	3.205	3.599	a
3	81.14	0.300	0.370	f
4	82.48	2.820	3.419	g
5	89.39	3.024	3.383	h
6	92.46	1.200	1.298	b
7	93.09	0.660	0.709	d
8	86.64	0	0	e

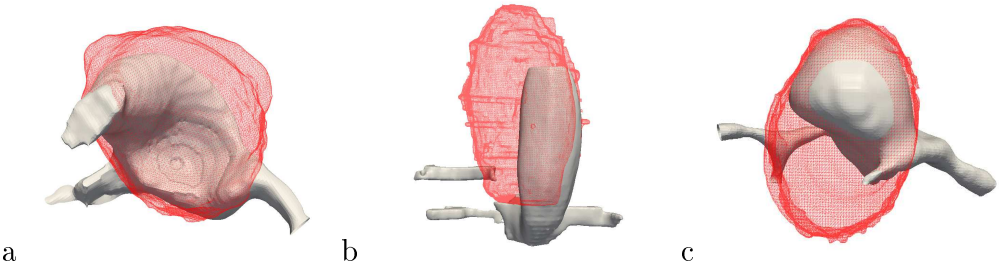

a b c

FIGURE 5.14: Examples of 3D visualization using our multilevel segmentation method for patient 2 in Figure 5.14a, patient 5 in Figure 5.14b, patient 6 in Figure 5.14c: lumen part and vessels in gray, thrombus in red.

on the 8 patients in terms of mean and standard deviation of SMFs.

Now in Figure 5.14, we give a 3D visualization of 2D slices segmented using the proposed method. The segmented aneurysms in this figure correspond to 3 patients. For the patient 5 (Figure 5.14b), there are 35 images of size 944x944 pixels; the in-plane resolution is 0.245mm; the slice gap is 1.500mm. For the patient 2 (Figure 5.14a) and patient 6 (Figure 5.14c), they have the same number of images (32) and the same image size (512x512 pixels). But they have different in-plane resolutions (0.410mm and 0.398mm, respectively) and different slice gaps (0.625mm and 1.500mm, respectively).

5.4 Conclusions and perspectives

We have proposed a multilevel segmentation method based on lattice Boltzmann and level set model. The use of lattice Boltzmann technique has allowed us to

bring out the lumen and thrombus, and the level set method with shape prior has refined the contour of the thrombus. The results on CTA images showed that the proposed method allows both lumen and thrombus to be well segmented. Visually, the segmented aneurysms are close to those given by medical experts. Quantitatively, the SMFs obtained by the proposed segmentation have a value of 88.37%, demonstrating good segmentation accuracy. In our future work, we would like to perform the noninvasive study of the evolution of cerebral aneurysms, with the objective to estimate the movement of the wall of aneurysms.

Chapter 6

Aneurysm segmentation in 3D

Abstract

The goal of this chapter is to introduce the use of LBM for the segmentation of 2D+t and 3D images. Automatic segmentation of 3D medical images remains a difficult task due to noise and inhomogeneity in the images. Although LBM is a common mathematical tool in fluid dynamic simulation, its use for segmenting 3D medical images is still new and is a challenge. In this chapter, we introduce the LBM D3Q27 model for segmenting 2D+t vessel (without and with noise) images and 3D aneurysm RA and DSA images. The experiments and results show the segmentation and high robustness to noise achieved by the proposed method.

Résume

Le but de ce chapitre est d'introduire l'utilisation de LBM pour la segmentation des images 2D+t et 3D. La segmentation automatique des images médicales en 3D ou 2D+t reste une tâche difficile en raison du bruit et de l'inhomogénéité dans l'image. Bien que le LBM soit un outil mathématique performant pour résoudre des problèmes de mécanique des fluides, son utilisation pour segmenter des images médicales est nouvelle et reste un défi. Dans ce chapitre, nous introduisons le LBM modèle D3Q27 pour segmenter les vaisseaux 2D+t (avec et sans bruit) et les anévrismes 3D. Les expériences et les résultats montrent les bon résultats de segmentation et la bonne robustesse au bruit obtenus par la méthode proposée.

6.1 Introduction

3D DSA (digital subtraction angiography with three dimensional reconstruction) images and 3D RA (rotation angiography with three dimensional reconstruction) images allow the acquisition of high quality images of cerebral vessels. Specially, 3D DSA images have higher quality than 3D RA images in representing cerebral aneurysm.

There is some literature on the segmentation of cerebral aneurysm in 3D RA images. [Hernandez 2007] proposed a technique of geometric deformable model with associated energy function to segment cerebral aneurysm in 3D RA and CTA images. The authors of [Bogunović 2010] improved a geodesic active region method and evaluated it on images containing cerebral aneurysms. [Hentschke 2012] introduced a system to automatically detect cerebral aneurysms in 3D RA, MRA and CTA images. To the best of our knowledge, there is no work on the use of LBM for 3D aneurysm segmentation.

In chapter 4, we have proposed a LBM anisotropic diffusion segmentation model for 2D, 3D and 4D data. In this chapter, we present the details about the use of the model for the 3D segmentation of aneurysm, including the experiments, results and conclusion.

6.2 Experiments and results

6.2.1 Data

The proposed segmentation method was performed on 2D+t images and 3D images. The 2D+t images concern 2 dataset from 1 patient and the 3D images concern 5 dataset of 5 patients from the Montpellier CHU (data base of the Thrombus project $N°$ FP7-ICT-2009-6-269966). For 2D+t image cases, they (without and with noise) are shown in Figure 6.1 and 6.2 and for 3D image cases, we have different types of images like 3D RA and 3D DSA and they are illustrated in Figure 6.3.

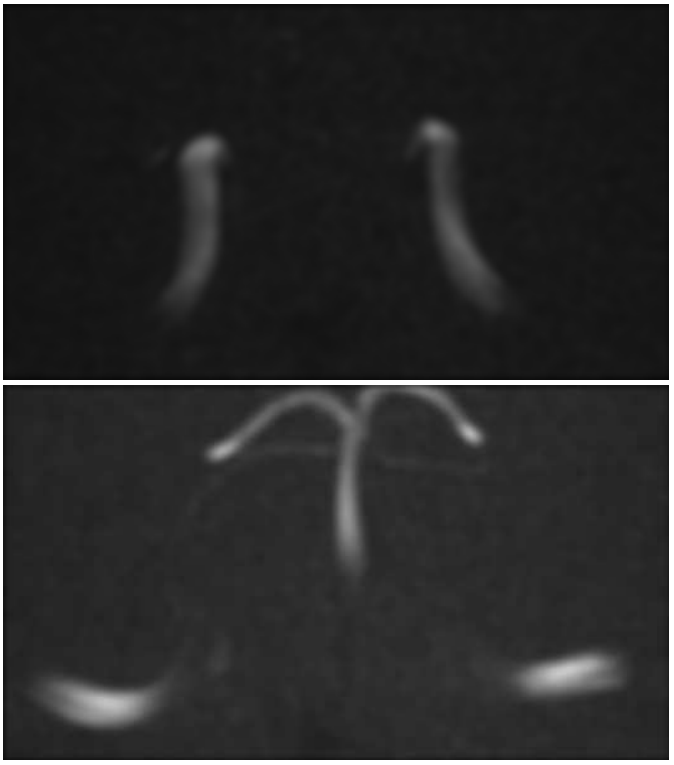

FIGURE 6.1: 2D images from 2D+t image (without noise).

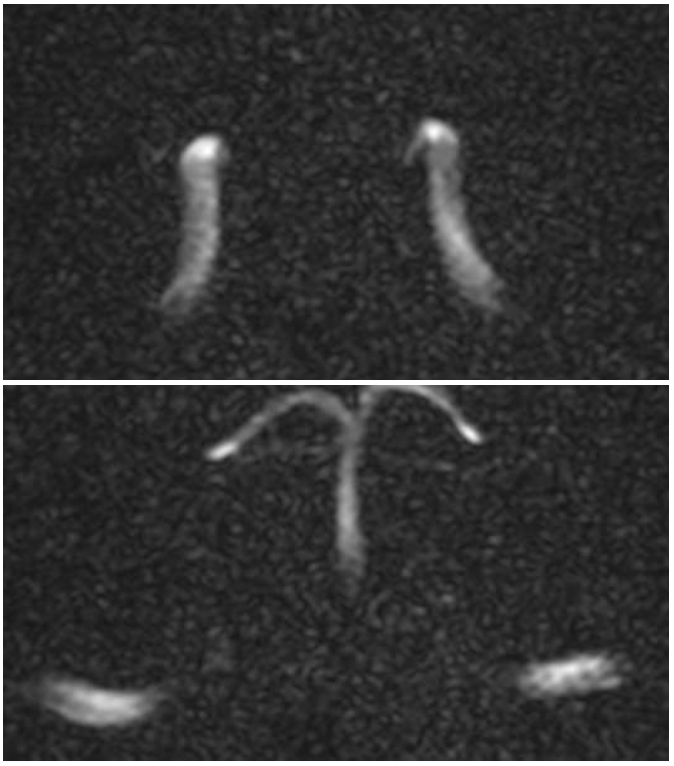

FIGURE 6.2: 2D images from 2D+t image (with noise).

6.2.2 Results

Firstly, the proposed segmentation method was tested on two 2D+t images. In such case, we can view time t as the third dimension. In consequence, we treat 2D+t images as a whole to process it by LBM. Figure 6.3 and Figure 6.4 give us some results from 2D+t(1) (Figure 6.1) and 2D+t(2) images (Figure 6.2) by different views. The value of parameter T and the corresponding patients are shown in table 6.1.

Secondly, the segmentation method was tested on 5 patients corresponding to three 3D DSA images and two 3D RA images. Figure 6.5 shows some examples; a 3D DSA image is shown in left of first row and a 3D RA image in left of second row. We can see clearly that the 3D RA image has more noise and less contrast with background.

Figure 6.5 gives us the 3D original images in left and its corresponding segmentation results in right. Then, we preform our method on other cases and Figure 6.6 shows other three 3D segmentation results. Other parameters are the same as those in 2D LBM, but T is different for each patient. Also, the value of the parameter T and the corresponding patients are shown in table 6.1.

TABLE 6.1: Choice of parameters

Patients	**T**	**Images**
RAS3	125	Figure 6.3 first row
RA1	156	Figure 6.3 second row
RAS4	123	Figure 6.4 left
RA2	156	Figure 6.4 middle
RAS1	118	Figure 6.4 right
2D+t(1)	71	Figure 6.5
2D+t(2)	81	Figure 6.5

As we can observe, the target objects were well segmented in both with and without noise 2D+t cases (shown in Figure 6.3 and 6.4). Meanwhile, for the 3D DSA and RA images shown in the left row of Figure 6.5, the segmentation results (in right row of Figure 6.5) are accurate too. All these above demonstrate that the proposed method has good segmentation accuracy and promising application to image denoising.

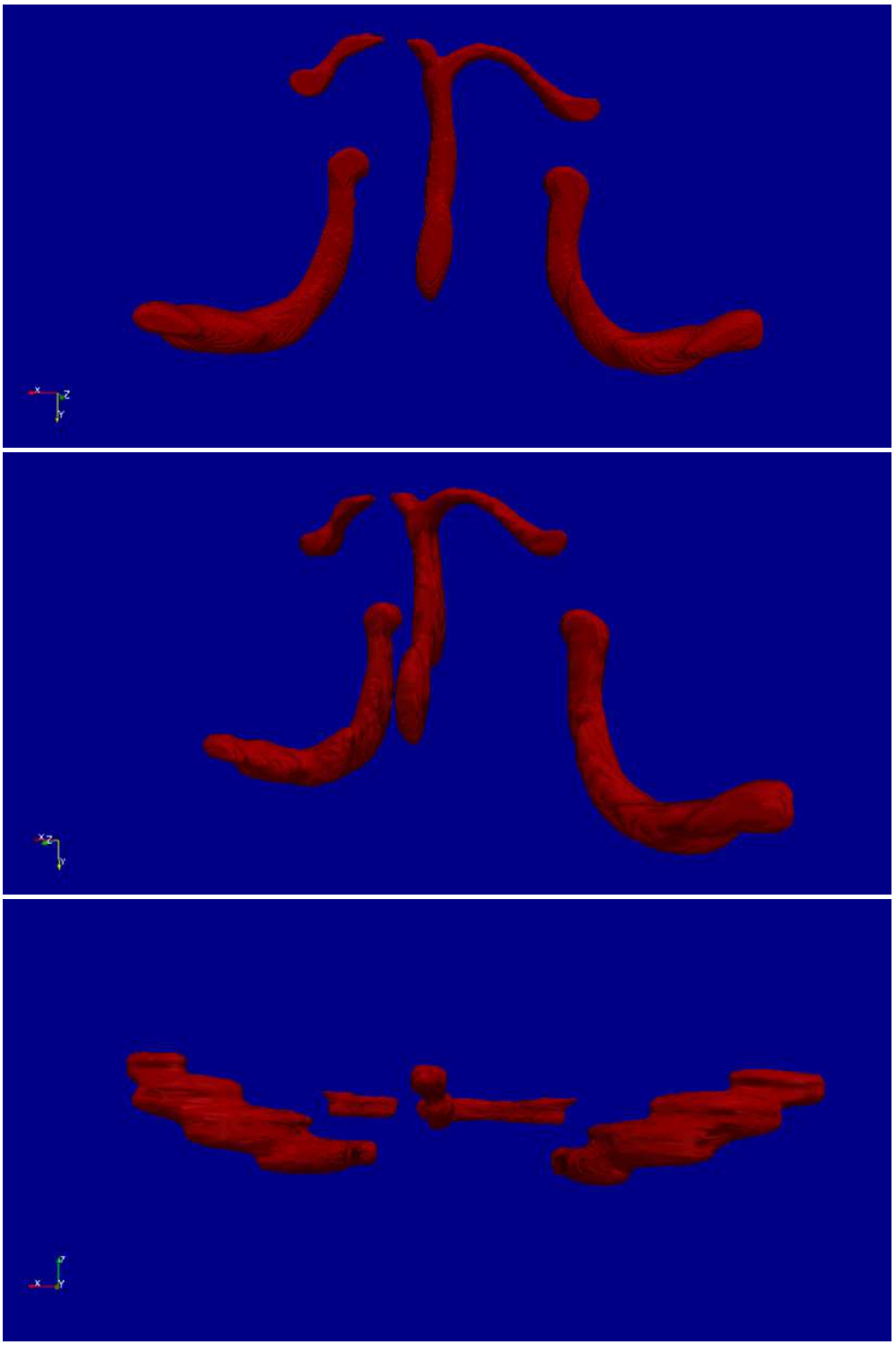

FIGURE 6.3: Results from 2D+t image sequence (without noise).

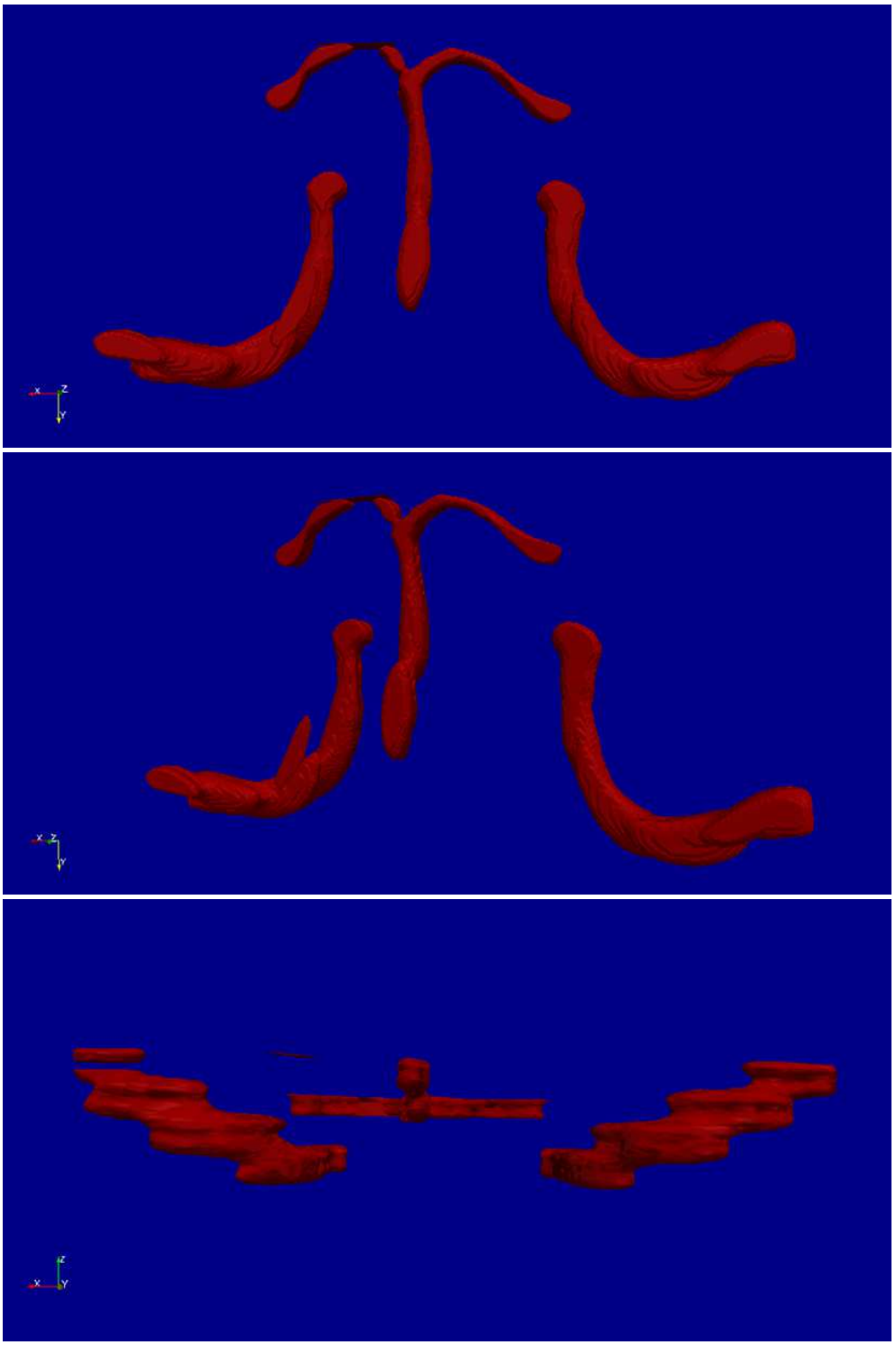

FIGURE 6.4: Results from 2D+t image sequence (with noise).

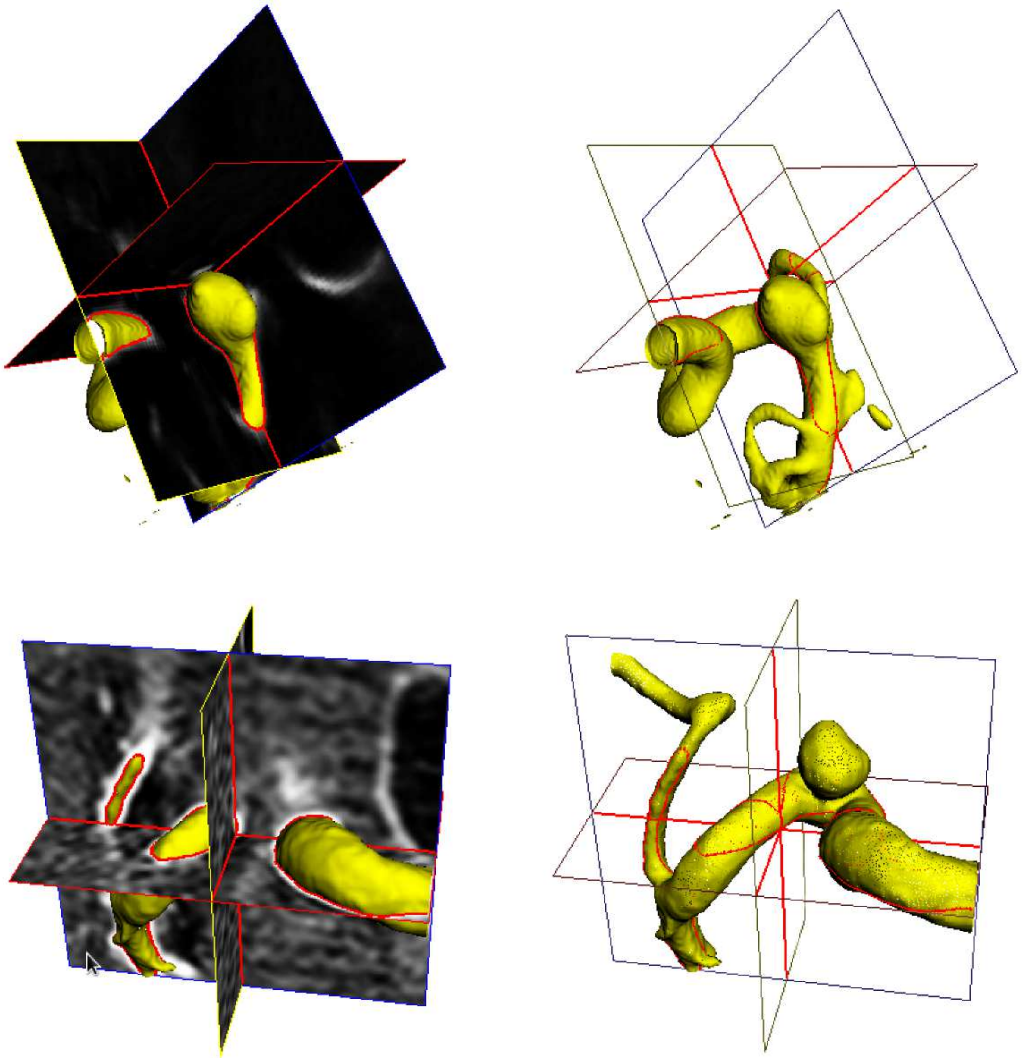

FIGURE 6.5: The 3D original images in left and its corresponding results in right.

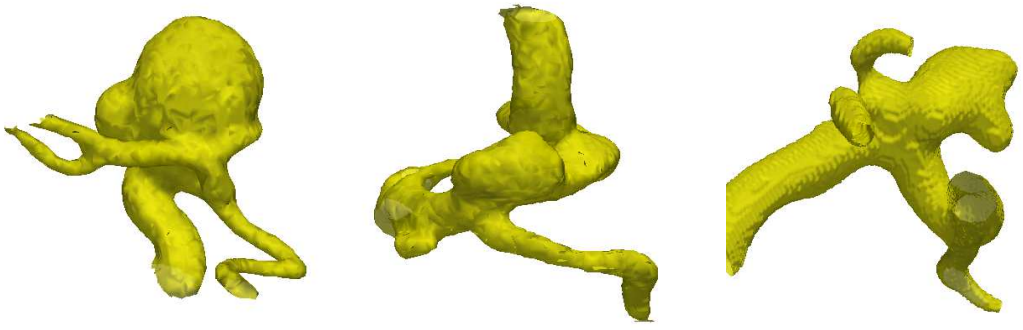

FIGURE 6.6: Examples of 3D visualization using the 3D LBM segmentation method.

6.3 The advantage of 3D segmentation model

There are two general groups of 3D image segmentation methods. One group firstly views a 3D data base as several 2D slices and then uses the 2D methods to segment each slice. In this case, a reconstruction step is needed after 2D segmentation. The other group would perform a 3D segmentation directly on the 3D data. In aneurysm segmentation studies, there is some literature about both of these methods. [Zohios 2012] proposed a level set based method to extract thrombus from 2D slices of a 3D image data set. A 2D lattice Boltzmann geodesic active contour method for aneurysm segmentation in CTA images was introduced by [Chen 2014]. Also, [Law 2007, Hernandez 2007, Firouzian 2011, Zhang 2012] proposed 3D cerebral aneurysm segmentation methods for 3D medical images. However, there is few research working on the comparisons between these two groups. In this section, we will perform our 2D and 3D LBM segmentation on the same cerebral aneurysm case in order to study the difference between the two models.

The original image for the patient in the right of Figure 6.6 is used for our test. The parameter T is from Otsu method and it equals 118 for both 2D and 3D models. For this patient, the size of 3D image is (201, 201, 101). That is to say, there are 101 2D slices and the size of each slice is (201, 201). Figure 6.7 shows the results from 2D model in left and from 3D model in right.

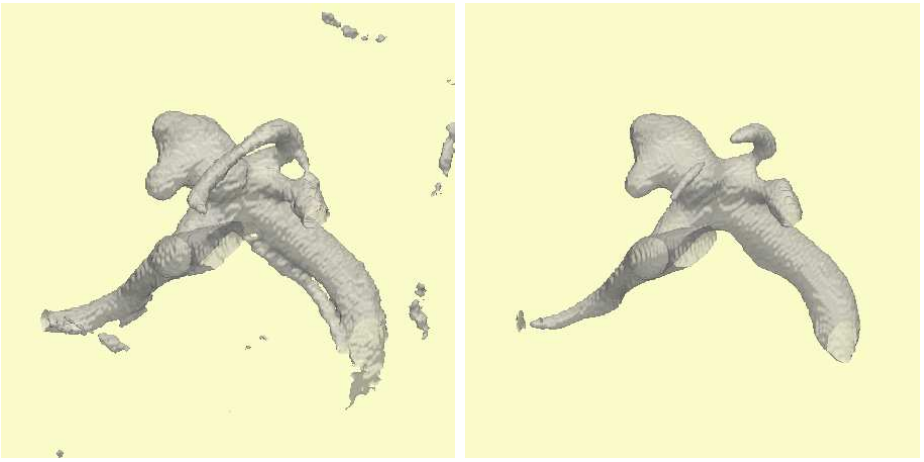

FIGURE 6.7: Aneurysm segmentation results based on 2D (left) and 3D (right) models.

In left of Figure 6.7, we reconstructed the 3D geometries from 2D segmentation based on 2D slices. As we can see, there are some unexpected small parts appearing

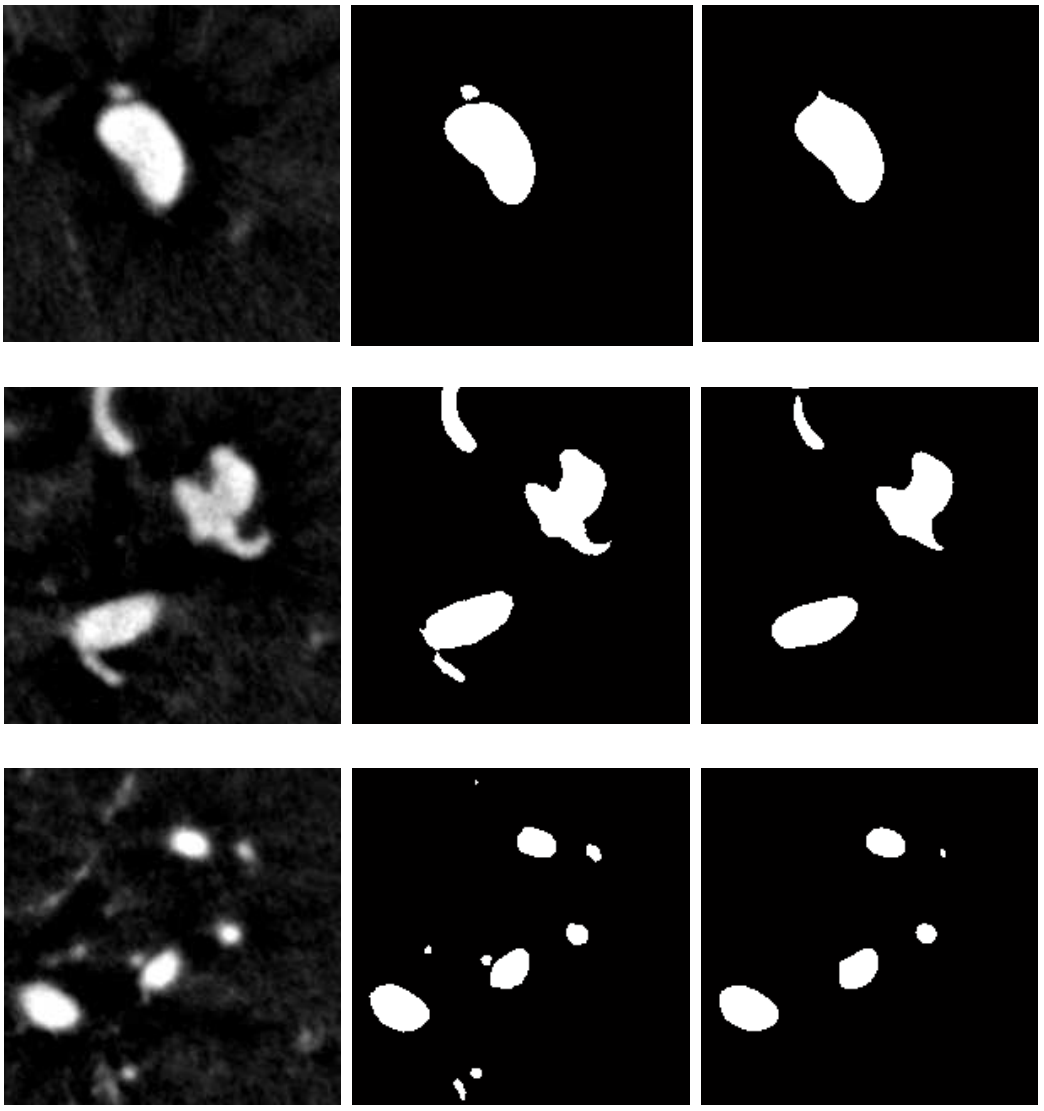

FIGURE 6.8: The original images and the corresponding segmentation results.

in this case. Normally, they are brighter parts in the original images such as small vessels, special tissues or some parts produced by imaging devices. On the contrary, in right of Figure 6.7, the results obtained by 3D method are much cleaner.

To be more precise, we worked on the comparison between the results from 2D and 3D segmentation methods in 2D cases. Figure 6.8 shows the 20^{th}, 50^{th} and 80^{th} original images in left and the corresponding results obtained by 2D and 3D segmentation methods in middle and in right, respectively.

Unlike 2D models, for each pixel, 3D segmentation methods would take its three dimensional neighboring pixels in consideration. Some specific pixels may get connected with the target object in 2D view but not in 3D view. These pixels,

which don't make part of the target object in 3D perspective, will not be included in final segmentation results with 3D methods. That's why the results from 3D method are cleaner.

6.4 Conclusion

We have proposed a 3D image segmentation method based on LBM with anisotropic diffusion term. The results showed that the proposed method is robust to noise and it has considerable advantage over 2D segmentation methods. In the following work, we will extend this model to 4D segmentation and apply it to aneurysm wall motion detection.

Chapter 7

Aneurysm wall motion detected using D4Q81 model

Abstract

4D images formed of 3D+t become more and more popular. Conventional segmentation methods for 4D data consist in the segmentation of a series of 3D data. We propose a true 4D segmentation model by considering the 3D+t data as a 4D hyper volume and using a D4Q81 lattice in LBM where time is considered in the same manner as for other three dimensions for the definition of particle moving directions in the LBM model. The proposed method consists in segmenting a hyper object defined on a mathematical 4D space. The Dice coefficient obtained using the proposed method reaches an average value of 94.81%, demonstrating good segmentation accuracy. In addition, the proposed method has promising application to 4D image denoising.

Résume

Des images 4D sous forme de 3D+t deviennent de plus en plus populaires. Des méthodes classiques de segmentation pour ces images 4D consistent souvent en la segmentation d'une série d'images 3D. Nous proposons ici une 'vraie' segmentation 4D en considérant les images 3D+t comme un hyper volume 4D et en utilisant un réseau LBM D4Q81, dans lequel le temps est considéré de la même manière que les trois autres dimension pour la définition des directions de mouvement des particules dans LBM. La méthode proposée consiste à segmenter l'hyper objet défini dans un espace mathématique 4D. Les résultats montrent que le coefficient Dice obtenu en utilisant la méthode proposée atteint une valeur moyenne de 94.81%, démontrant ainsi une bonne précision de segmentation. En même temps, la méthode proposée a promis l'application de débruitage d'images 4D.

7.1 Introduction

In modern physics, space and time are unified under the term spacetime, and the time is usually treated differently from the other three spatial dimensions. In mathematics, four-dimensional space (4D) is an abstract concept derived by generalizing the properties of three-dimensional space to higher dimensions. For image processing, the advantage of 4D algorithms is that segmentation occurs in both space and time simultaneously, which allows to improve accuracy and robustness over existing 2D and 3D segmentation methods. In the past, a number of works have been devoted to 4D segmentation. [Montagnat 2005] extended the deformable surface framework by introducing time-dependent constraints to take the 4D (3D+t) nature of those images into account. The authors of [Montagnat 2003] presented a 4D (3D+t) echocardiographic image anisotropic filtering and a 3D model-based segmentation system. In [Cousty 2007], a new automated and fast procedure to segment the left ventricular myocardium in 4D (3D+t) cine-MRI sequences based on discrete mathematical morphology was proposed. Another 4D segmentation method on congenital aortic disease was addressed in [Zhao 2009]. In these articles, time is considered as linear and deterministic, which means it normally only has two directions: forward and afterward. Unlike previous methods, we propose a true 4D method taking time as same as the other three dimensions and more different directions could exist in the time dimension due to LBM.

Four-dimensional algorithms have their advantages in cerebral aneurysms segmentation, as the movement of aneurysm plays an important role in the thrombosis phenomena. Multiple imaging techniques–transcranial power Doppler ultrasonography (PD-US), phase-contrast magnetic resonance angiography (PC-MRA), dynamic computed tomographic angiography (4D-CTA) and three-dimensional rotational angiography (3D-RA) – have been used to detect and quantify wall motion but no standardized method exists [Wardlaw 1996], [Kato 2004], [Firouzian 2013], [Karmonik 2010], [Oubel 2010], [Zhang 2011]. Among these imaging modalities, the first two methods have a lower spatial resolution and are more susceptible to flow artifacts [Karmonik 2010], [Hoskins 1998] and 3D-RA is the most invasive technique. Therefore, 4D-CTA could be the best compromise between high spatial resolution and low invasiveness. In this paper, we used an phantom model to obtain 4D CTA images for our study on 4D segmentation method. And we also believe that in the foreseeable future, with the development of imaging technology,

the 4D segmentation will play an essential role in medical imaging and treatment evaluation.

LBM has its advantages for image processing. Firstly, for two-dimensional discrete images, the pixels arrangement can be naturally considered to be a lattice. Secondly, based on previously reported research [Chang 2009], we know that LBM has intrinsic ability of denoising, which can avoid adding supplementary preprocessing step. Thirdly, LBM allows for highly parallel processing. Specifically, we could easily prolong LBM into high dimension and define its corresponding parameters.

In this chapter, we use a LBM based framework for the 4D cerebral aneurysm images segmentation and the movement detection. We first segment a hypercube by using the proposed framework, and secondly we obtain the segmentation of a phantom aneurysm with the help of our proposed method. The most important contribution of this part is that we provide a 4D LBM model (see more details in chapter 4) and detect the aneurysm movement.

The rest of the chapter is organized as follows. Experiments and results on a synthetic hypercube and a phantom are given in next section, followed by conclusions and perspectives.

7.2 Experiments and results

7.2.1 Data

The proposed 4D segmentation method was first applied on a 4D test image of size (40, 40, 40, 40) and center (20, 20, 20, 20). We defined that the range of its gray level is [0, 1]. The main object of this image is a hypercube of which length of side is 30. Then, we added 10% random noise in hypercube image as a new test image, and we increased the random noise from 30% to 300% in other 8 hypercube images. Our proposed method was validated on all 10 hypercube images containing 1 image without noise and 9 images with different level of random noise, respectively.

Then, another test image containing six hyper objects was performed by the proposed method. This hyper image is generated from one 2D test image shown in Figure 7.1. First we combined 8 same slices to create a 3D image. Then we produced the hyper image by using these 3D images. This hyper image is shown by

3D images with different time in Figure 7.2. Furthermore, considering the size of memory is still a problem in 4D segmentation processing, the size of this hyper image is only [94, 67, 10, 10].

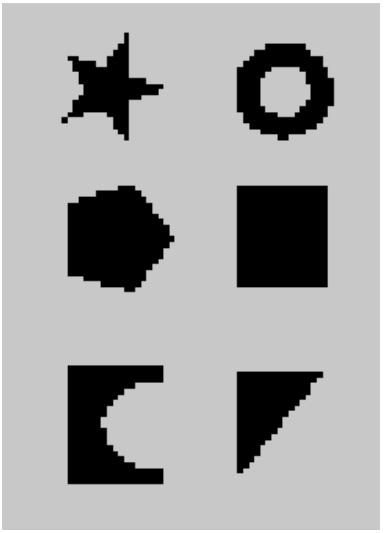

FIGURE 7.1: A slice of 4D hyper objects image.

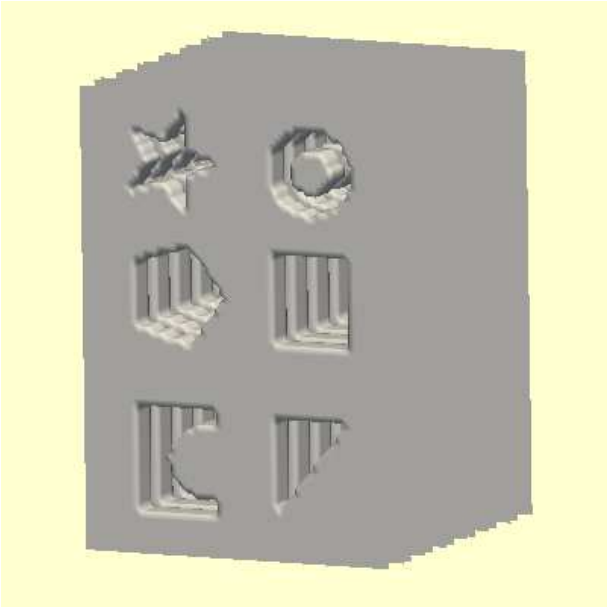

FIGURE 7.2: A view of 4D hyper objects image.

At last, we applied our method on a Computed Tomography Angiography (CTA) image of a phantom of an aneurysm synthetic model which was designed by Charleroi CHU (data base of the Thrombus project $N°$ FP7-ICT-2009-6-269966). As we mentioned, 4D-CTA could be the best option for our 4D segmentation study. In this section we first used a flexible plastic to manufacture a sphere together with a cylinder which are similar to artery and its bulging aneurysm. The

diameter of sphere and cylinder corresponding to artery and aneurysm are about 5mm and 10mm. We named it aneurysm model. Then, we injected real blood into this aneurysm model with velocity and pressure parameters mimicking real data present in human body. With the help of CTA scans like Figure 7.3 in the up, we can obtain 4D data. Figure 7.3 in the up is the experimental facility: the frame, the skull model and the aneurysm model. We can observe in figure 7.3, that inside the skull there is only an aneurysm model. Actually, in the brain, there are lots of different kinds of tissues and organs. The image obtained by CTA can not be so clear and pure. Accordingly, we tested our method on the data without noise and the data with different level of random noise. As the range of phantom images [0, 255] is different of hypercube images, we added X random noise on phantom image using

$$I_{noise} = I_{original} + X \cdot randn \cdot 255 \tag{7.1}$$

where I_{noise} is the new image with noise, $I_{original}$ the original image without noise, X the quantity of random noise and $randn$ the function of random noise.

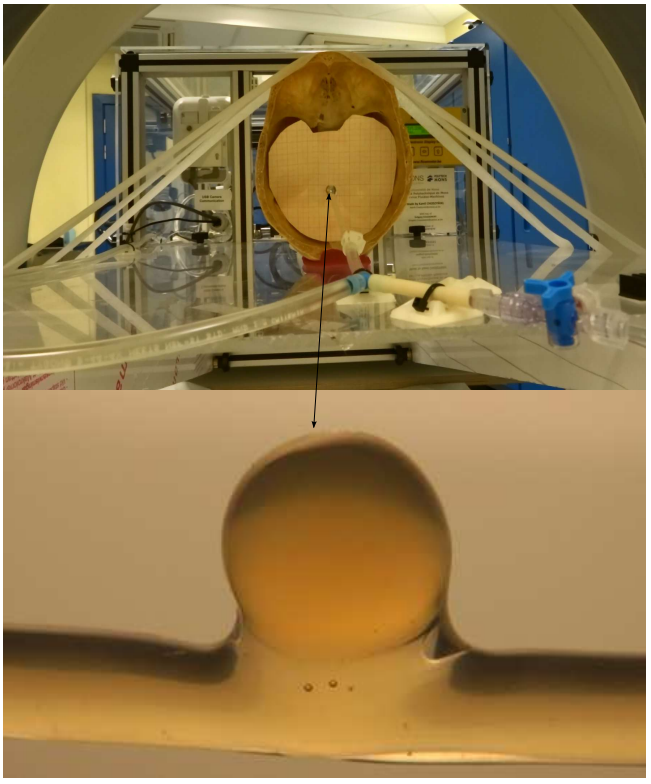

FIGURE 7.3: The experimental facility and the aneurysm model are designed by Charleroi CHU.

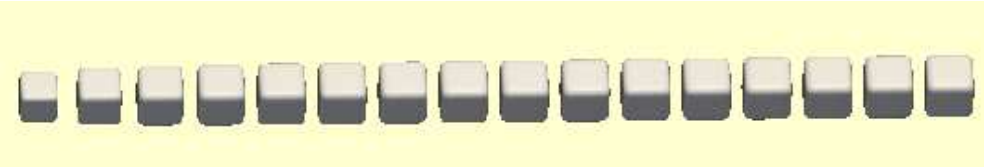

FIGURE 7.4: Result of hypercube image without noise using the proposed method.

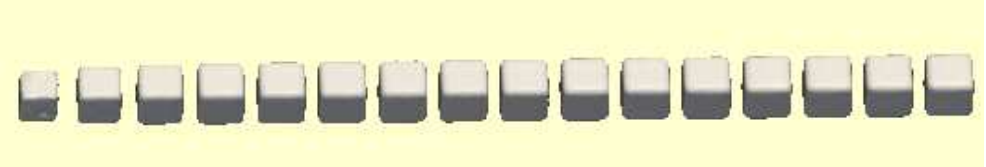

FIGURE 7.5: Result of hypercube image with 100% random noise using the proposed method.

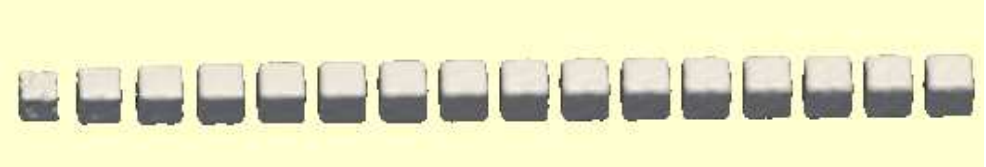

FIGURE 7.6: Result of hypercube image with 200% random noise using the proposed method.

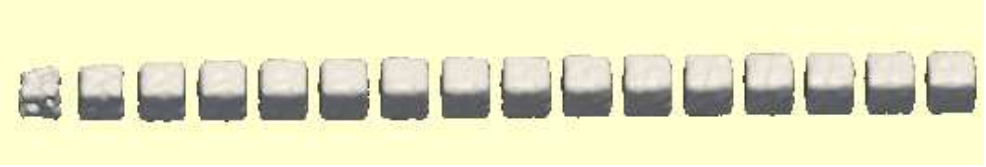

FIGURE 7.7: Result of hypercube image with 300% random noise using the proposed method.

7.2.2 Results

7.2.2.1 Hypercube

The proposed 4D segmentation method performed on 10 hypercube images at first. These 10 images contain 1 image without noise and 9 images with random noise, 10%, 30%, 50%, 70%, 100%, 150%, 200%, 250%, 300% random noise respectively. Figure 7.4 illustrates result of segmentation of hypercube image using the proposed method with 30 iterations.

As we can observe, the hypercube is well segmented by our proposed method. Also, we apply our method on other 9 hypersphere images and we give part of

results from these 9 images. Results of hypercube images with different random noise are shown from Figure 7.5 to Figure 7.7.

Obviously, the obtained results from Figure 7.5 to Figure 7.7 are similar to Figure 7.4, which demonstrates that the proposed method has promising application to 4D image denoising. Quantitatively, the comparison between our segmentation results and the perfect contour is shown in Figure 7.8. We illustrate the Dice values of 10 hypersphere from chapter 4 and 10 hypercube images with 0% to 300% random noise in red and in green. We selected several 3D samples from each 4D image and calculated the value of Dice for each 3D sample. We obtained the average value of Dice and the value of CV for each 4D image which is shown in Figure 7.8 the blue bar-graph and the purple bar-graph. As can be observed, we have better segmentation results with random noise from 0% to 200% than from 200% to 300% since the Dice values are greater. Even we increased the random noise to 300%, the value of Dice and average of Dice are still high. The results show that the proposed 4D segmentation method could generate hypersphere and hypercube outlines close to the perfect contour even with high level of noise.

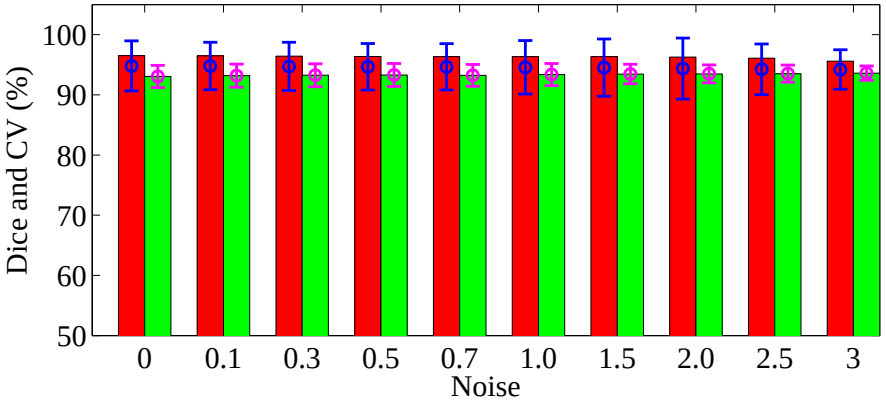

FIGURE 7.8: Dice, average of dice and its corresponding CV of each image. For hypersphere, the bar-graph in red and blue; for hypercube, the bar-graph in green and purple.

To test the behavior of the proposed model, it applied to hyper objects images as shown in Figure 7.1 and Figure 7.2. In order to see the results clearly, we give a cross section which was shown in Figure 7.2.

FIGURE 7.9: A cross section of 4D hyper objects image.

7.2.2.2 Phantom

The movement in aneurysm is due to heart pump and it is really small. We used the same condition to our artificial aneurysm model which means we could only observe very small movement. In our experiments, with a bigger iterations number our method has a better denoising ability but it also leads to the problem in less movement detection (the small movement will be discarded because of the denoising). So, choosing a reasonable iteration N is obviously important.

The 1^{st} row in Figure 7.10 represents values of Dice by choosing iterations from 1 to 35. The values of Dice are rising from 1 iteration to 5 iteration and going down from 5 iteration to 35 iteration. The rising part means the numbers of iteration is not enough from 1 to 4 and the 4D image might be not segmented fully. The declining part means the numbers of iteration is excessive and with the increase of iteration number, the values of Dice are smaller and smaller.

Meanwhile, we selected several 3D samples from each 4D image and calculated the value of Dice. Also, we calculated the average value of Dice and the values of CV for each 4D image which are shown in the 2^{nd} row and the 3^{rd} row of Figure 7.10. The average of Dice is almost the same with Dice which is shown in the 1^{st} row of Figure 7.10. We can say that the 3D samples are similar to each other, in other words, the movements in such images are extremely small. The values of CV fall down at first and rise after 7 iteration and CV has least value when the iterations number is 6.

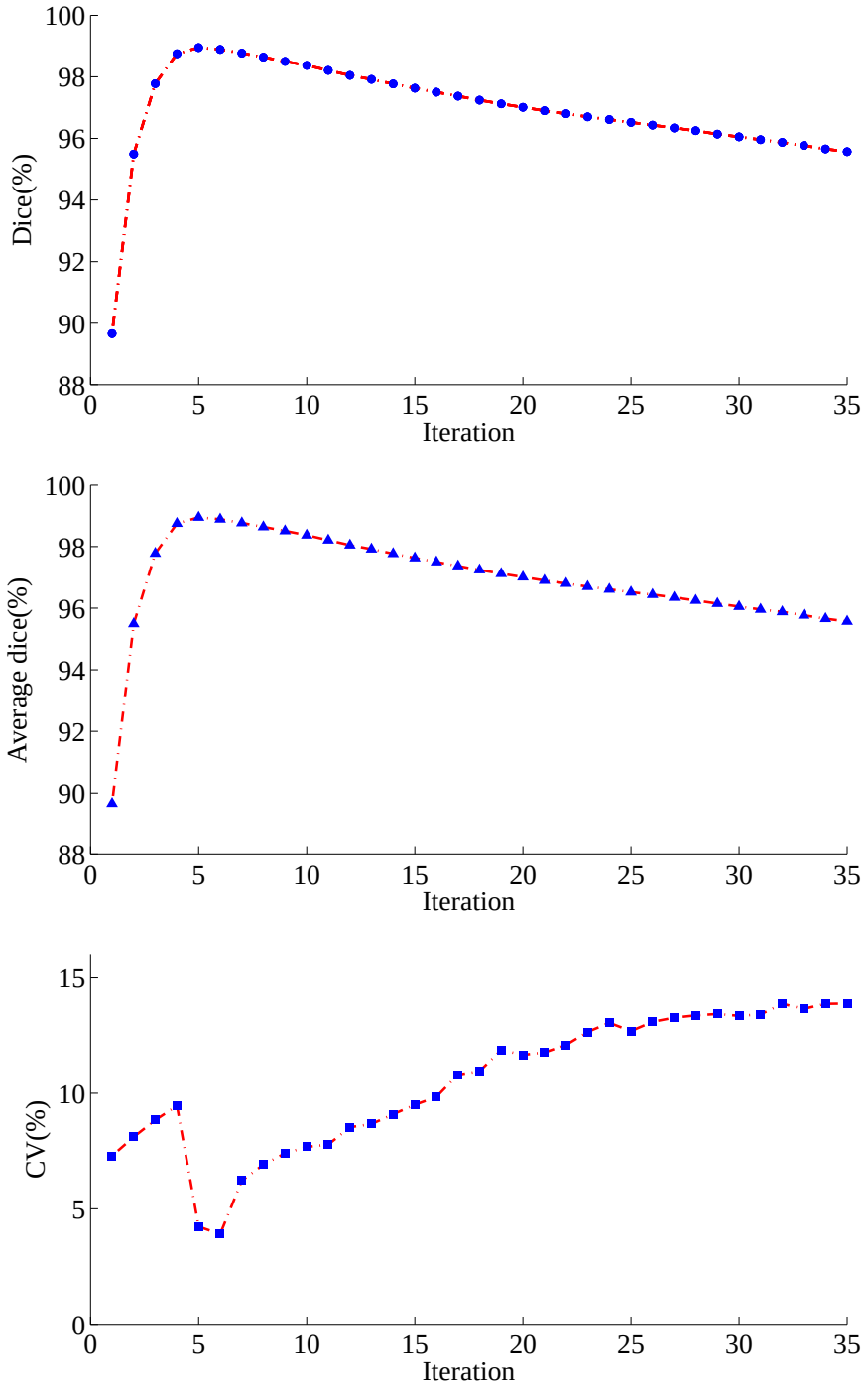

FIGURE 7.10: The corresponding value of dice, average of dice and CV by choosing different iteration.

TABLE 7.1: Value of Dice, average of Dice and CV.

Iteration	Dice	Average of Dice	CV
5	98.95	98.95	4.23
6	98.89	98.89	3.90
10	98.37	98.37	7.68

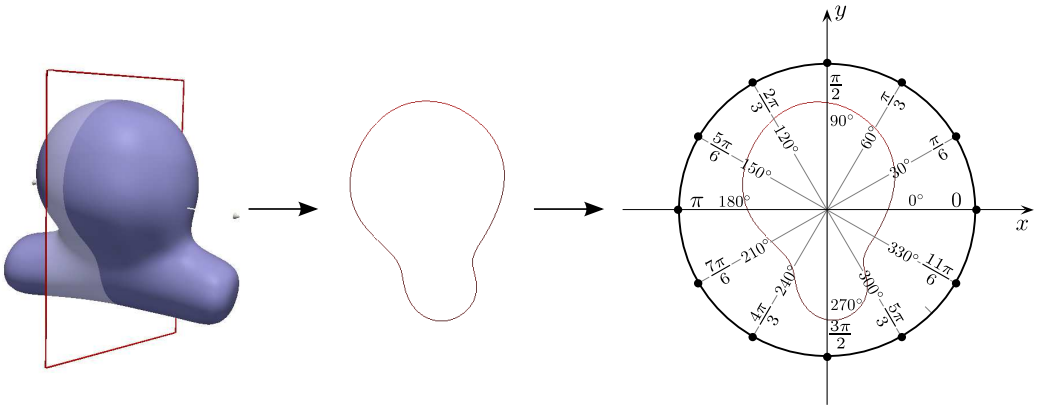

FIGURE 7.11: The 3D contour in left, the 2D cross section in middle, the circle and its special 12 angular points which we used to measure the distance in right.

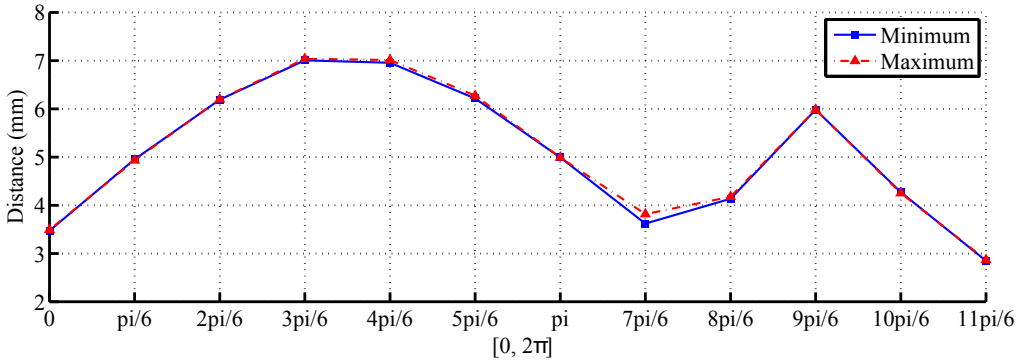

FIGURE 7.12: The distance corresponding to the maximum and minimum contours.

As we know, a better result has greater value of Dice and smaller value of CV. In Figure 7.10, we have greatest value of Dice with iterations number of 5 and smallest value of CV with 6 iteration number. So when the iterations number is around 5 or 6, we will obtain better results. As we mentioned before, the medical images might be more complex than we used and we should take the denoising ability into consideration. So we choose 10 as the iteration number, because of high value of Dice, low value of CV and denoising ability. We provide the details in table 7.2.

Then, we applied the proposed LBM segmentation algorithm to the phantom

image with 10 iterations. The 3D contours is shown in purple in Figure 7.11. We cut the image to obtain the 2D cross section. The contour of the cross section is shown in Figure 7.11 in red line. After that, we calculated the distance between the center and the 12 contour points shown in right in figure 7.11. We can observe two lines in figure 7.12 and the red one represents the distance corresponding to the maximum contour and the the blue one represents the distance corresponding to the minimum contour.

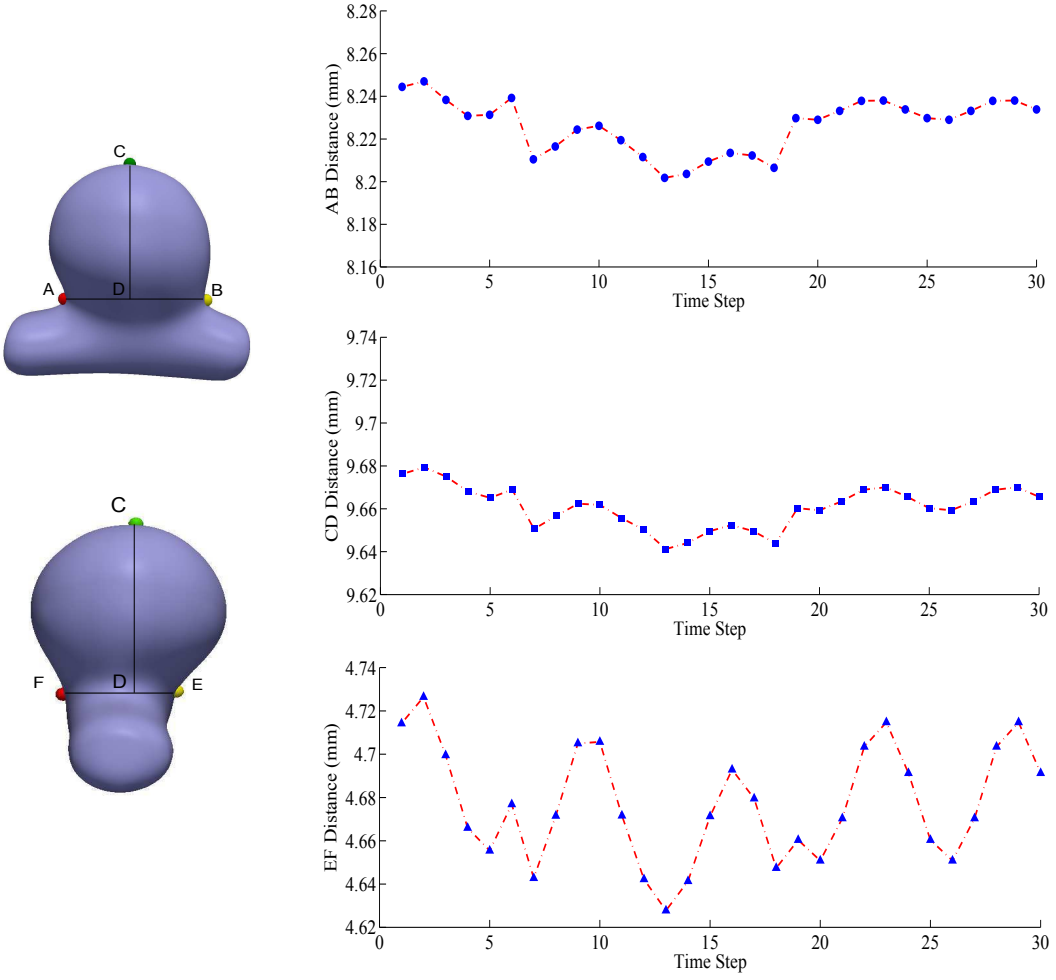

FIGURE 7.13: Estimation the movement.

More precisely, we would like to calculate the movement quantitatively. According to [Oubel 2010], they chose four points in the top, the end, the left and the right of aneurysm in x axis. We chose six points with specific characters: two are from top and end of aneurysm, four other are the intersecting points of aneurysm and artery in x and y axes. We marked these six points as C, D, A, B, E and F in Figure 7.13. As mentioned in [Ujiie 1999], the aspect ratio is an important parameter

which determines the state of aneurysm (whether it is going to rupture or not).

$$Aspect\ ratio\ \% = \frac{Depth\ of\ aneurysm}{Neck\ of\ aneurysm} = \frac{CD}{AB}\ or\ \frac{CD}{EF} \tag{7.2}$$

where AB, CD and EF represent the distance between point A and B, C and D, E and F. The points A, B, C, D, E, F are shown in Figure 7.13 in left. In right of Figure 7.13, the horizontal axis is time and the vertical axis is distance. For AB and EF, the movement during time is bigger than CD. Comparing AB with EF, AB has smaller movement. That is to say, in this case the EF direction has biggest movement. After that, we studied the minimum and maximum distance of AB, CD and EF. Also, 0.0987mm shows that EF has the biggest movement. For the change of aspect ration, $\frac{CD}{EF}$ is bigger than $\frac{CD}{AB}$. In the end, the average value provides us a normal way to measure this aneurysm.

TABLE 7.2: Parameters of aneurysm.

Value(mm)	**AB**	**CD**	**EF**	$\frac{CD}{AB}$	$\frac{CD}{EF}$
Minimum	8.2018	9.6412	4.6278	1.1735	2.0479
Maximum	8.2470	9.6793	4.7265	1.1756	2.0833
Movement	0.0452	0.0381	0.0987	0.0021	0.0354
Average	8.2263	9.6609	4.6773	1.1744	2.0655

At last, we added random noise with different level from 10% to 100% in phantom image. Figure 7.14 shows the comparison between our proposed segmentation method with 10 iteration and threshold method. We view the results from threshold method in 4D phantom image without any noise as the prefect result (Dice=100%). The corresponding Dice value from our proposed method is 98.37%. After that, we added random noise (10%) in phantom image. The Dice values from threshold method and our method are 94.85% and 98.33%. Even with 10% noise, we can see the obvious advantage for our LBM segmentation method. With 100% noise, the Dice values are 44.58% and 96.64%respectively. The results from threshold method change a lot when we add noise, meanwhile the proposed method has stable results.

7.3 Conclusions and perspective

We have proposed a true 4D segmentation method based on lattice Boltzmann model. The method has been evaluated on both a synthetic hypercube and 4D

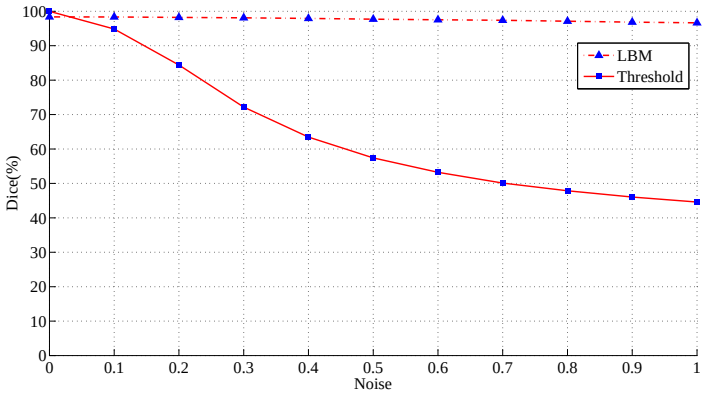

FIGURE 7.14: The comparison between our proposed segmentation method and threshold method.

images of a physical aneurysm phantom made of plastic components. The results showed that despite the strong noise in the hypercube image, the hypercube is segmented efficiently. Also, the use of LBM has allowed the aneurysms to be well segmented, with the value of Dice is 94.81%. In our future work, we would like to implement the proposed method on a cluster for highly parallel processing in order to reduce computation time.

Part III

CONCLUSIONS

Chapter 8

Conclusion and perspectives

8.1 Conclusion

The central theme of this thesis is the study of lattice Boltzmann method for cerebral aneurysm segmentation.

The main contributions are in the following domains

1) Aneurysm segmentation method based on LBM

CTA images of intracranial aneurysms exhibit the particularity of presenting not just the lumen (appearing as a focal object), but also thrombus with low-contrast with respect to neighboring tissues, which renders their manual or automatic delineation difficult. We propose a multilevel segmentation methodology based on the combined use of LBM and level set technique to segment the lumen and the thrombus. In this framework, the traditional lattice Boltzmann (LB) equation is adapted to image segmentation problems by integrating a diffusion source term in the LB formulation. More precisely, we first segment the lumen of intracranial aneurysms by using the LBM. After that, we perform the segmentation of the thrombus with the aid of a different LBM configuration coupled with level set technique to refine the shape of the thrombus.

2) Movement detection of aneurysm

A ruptured aneurysm releases blood into the spaces around the brain, which is called subarachnoid hemorrhage. The cause of aneurysm rupture is the size, the

form, the aspect ratio and the change of aneurysm by heart pumps. We propose a true 4D segmentation model by considering the 3D+t data as a 4D hyper volume and using a D4Q81 lattice in LBM where time is considered in the same manner as for other three dimensions for the definition of particle moving directions in the LBM model. The proposed method can segment the aneurysm in 3D+t, after that we calculate the size, the aspect ratio and the change of aneurysm in order to evaluate the influence of heart pumps.

8.2 Perspectives

In this thesis, we present different aneurysm segmentation methods and develop the segmentation method based on LBM. Our work is an important part for the preparation of endovascular treatments. In the future, it would be interesting to develop deeper LBM 4D not only for segmentation but also for other processing in 3D+t images.

In our case, the LBM has been applied to image processing, but the link between numerical simulation and image processing is not clear. Another perspective is considering other segmentation techniques, coupling with numerical simulation, giving the capabilities of the LBM in the field of hydrodynamic simulations.

8.3 Author's publications

8.3.1 Journals

Yan Wang, Laurent Navarro, Omer Eker, Yue Zhang, Ricardo A. Corredor Jerez, Yu Chen, Yuemin Zhu, Guy Courbebaisse, "Automatic multilevel segmentation of intracranial aneurysms in ct angiography images", Physics in medicine and biology. Revised.

Yan Wang, Laurent Navarro, Yue Zhang, Ricardo A. Corredor Jerez, Yuemin Zhu, Guy Courbebaisse, "4D image segmentation based on LBGK method",Image and vision computing. Submitted.

Yu Chen, Laurent Navarro, Yan Wang, Guy Courbebaisse,"Segmentation of the thrombus of giant intracranial aneurysms from CT angiography scans with lattice Boltzmann method", Volume 8, Issue 1, Pages 1-8, Medical image analysis, January 2014.

Yan Wang, Y. M. Zhu, G. Courbebaisse, and L. Ding, "Detection and Extraction of Feature Points in Robot Vision Using Lattice Boltzmann Method", Science Technology and Engineering, vol. 11, no. 32, pp. 8045-8048, 2011.

8.3.2 Conference Proceedings

Yan Wang, Guy Courbebaisse, Yue Min Zhu, "Segmentation of giant cerebral aneurysms using a multilevel object detection scheme based on lattice Boltzmann method", ICSPCC 2011, IEEE International Conference on Signal Processing, Communications and Computing, Xian, China, September 2011.

Yan Wang, Guy Courbebaisse, "Automatic segmentation of cerebral aneurysms from CTA", ElyT Workshop, Sendai, Japan, February 2013.

Conclusion

Le thème central de cette thèse est l'étude de la méthode de Boltzmann sur réseau pour la segmentation des images d'anévrismes cérébraux.

Cette thèse a d'abord brièvement présenté la problématique des anévrismes et de l'imagerie des anévrismes, ainsi qu'un état de l'art des méthodes de segmentation. Cette étude bibliographique a permis de mettre en place le cadre nécessaire au développement de nouvelles méthodes de segmentation des anévrismes. Dans le développement de ces nouvelles méthodes, il est nécessaire de bien prendre en compte deux aspects. D'une part, le volume, la hauteur, le diamètre maximal, la surface d'un anévrisme sont utiles pour prédire le risque de rupture. D'autre part, des méthodes de segmentation des anévrismes cérébraux jouent un rôle important pour analyser le mouvement des anévrismes.

Les contributions principales se situent dans les domaines suivants:

1) Nouvelle méthode de segmentation des anévrismes

Une méthode de segmentation des anévrismes est proposée basée sur la méthode de Boltzmann sur réseau (LBM). Dans ce cadre, LBM est adaptée aux problèmes de segmentation d'image en intégrant un terme source de diffusion dans la formulation. Plus précisément, nous avons d'abord segmenté la lumière de l'anévrisme intracrânien en utilisant LBM dans une configuration de diffusion simple. Après que la lumière soit segmentée, nous effectuons la segmentation du thrombus à l'aide d'une configuration différente LBM, en la couplant la méthode des courbes de niveaux pour affiner la forme du thrombus.

2) Segmentation des anévrismes basée sur une formulation 4D LBM

Nous avons étudié les avantages de la description 4D pour la segmentation. Nous avons proposé un cadre basé sur LBM 4D pour la segmentation des images d'anévrismes

intracrâniens. Le modèle proposé est une véritable méthode de segmentation en 4D. Le point le plus important est que nous fournissons un modèle LBM 4D et ses directions de vitesse discrètes correspondantes sont dérivés de modèles LBM en 1D, 2D et 3D. Pour illustrer la méthode, nous avons d'abord segmenté une hypersphère et un hypercube en utilisant le cadre proposé et nous avons obtenu une bonne segmentation de l'anévrisme.

Dans cette thèse, nous avons présenté différentes méthodes pour la segmentation des anévrismes. Nous nous sommes efforcés de développer nos idées concernant la segmentation à l'aide de la LBM autant que nous le pouvions. Notre travail est une aide importante pour la préparation des traitements endovasculaires. Dans le futur, il serait intéressant de développer plus profondément la LBM 4D, non seulement pour la segmentation mais aussi pour d'autres opérations de traitement des images 3D+t.

Une autre perspective des méthodes développées dans cette thèse serait d'envisager d'autres techniques de segmentation, couplées à la simulation numérique, étant donné les capacités de la LBM dans le domaine des simulations en hydrodynamique. Dans notre thèse, la LBM a été appliquée au traitement d'image, mais le lien entre simulation numérique et traitement d'image est ténu et l'unification dans le cadre de la LBM est envisageable.

Bibliography

[Alessandrini 2011] M. Alessandrini, T. Dietenbeck, O. Basset, D. Friboulet and O. Bernard. *Using a geometric formulation of annular-like shape priors for constraining variational level-sets.* Pattern Recognition Letters, vol. 32, no. 9, pages 1240–1249, 2011.

[Aoyama 2003] Masahito Aoyama, Ikuo Kawashita, Yoko Naruse, Naoki Asada and Kazuo Awai. *Automated Cerebral Arteries Segmentation and Diameter Measurement of Aneurysm from MR Angiograms.* In Knowledge-Based Intelligent Information and Engineering Systems, pages 402–409. Springer, 2003.

[Bernard 2009] O. Bernard, D. Friboulet, P. Thévenaz and M. Unser. *Variational B-spline level-set: a linear filtering approach for fast deformable model evolution.* Image Processing, IEEE Transactions on, vol. 18, no. 6, pages 1179–1191, 2009.

[Betal 1997] D. Betal, N. Roberts and GH Whitehouse. *Segmentation and numerical analysis of microcalcifications on mammograms using mathematical morphology.* British journal of radiology, vol. 70, no. 837, pages 903–917, 1997.

[Bhatnagar 1954] Prabhu Lal Bhatnagar, Eugene P Gross and Max Krook. *A model for collision processes in gases. I. Small amplitude processes in charged and neutral one-component systems.* Physical review, vol. 94, no. 3, page 511, 1954.

[Bogunović 2010] Hrvoje Bogunović, José María Pozo, María Cruz Villa-Uriol, Charles BLM Majoie, Rene van den Berg, Hugo AF Gratama van Andel, Juan M Macho, Jordi Blasco, Luis San Román and Alejandro F Frangi. *Automated segmentation of cerebral vasculature with aneurysms in 3DRA*

and TOF-MRA using geodesic active regions: An evaluation study. Medical physics, vol. 38, no. 1, pages 210–222, 2010.

[Caselles 1997] Vicent Caselles, Ron Kimmel and Guillermo Sapiro. *Geodesic active contours.* International journal of computer vision, vol. 22, no. 1, pages 61–79, 1997.

[Chan 2000] T.F. Chan, B.Y. Sandberg and L.A. Vese. *Active contours without edges for vector-valued images.* Journal of Visual Communication and Image Representation, vol. 11, no. 2, pages 130–141, 2000.

[Chan 2001] Tony F Chan and Luminita A Vese. *Active contours without edges.* Image Processing, IEEE Transactions on, vol. 10, no. 2, pages 266–277, 2001.

[Chang 2009] Q. Chang and T. Yang. *A lattice Boltzmann method for image denoising.* Image Processing, IEEE Transactions on, vol. 18, no. 12, pages 2797–2802, 2009.

[Chen 2008] Y. Chen, Z. Yan and Y.H. Qian. *An anisotropic diffusion model for medical image smoothing by using the Lattice Boltzmann method.* In 7th Asian-Pacific Conference on Medical and Biological Engineering, pages 255–259. Springer, 2008.

[Chen 2014] Yu Chen, Laurent Navarro, Yan Wang and Guy Courbebaisse. *Segmentation of the thrombus of giant intracranial aneurysms from CT angiography scans with lattice Boltzmann method.* Medical image analysis, vol. 18, no. 1, pages 1–8, 2014.

[Cousty 2007] Jean Cousty, Laurent Najman, Michel Couprie, Stéphanie Clément-Guinaudeau, Thomas Goissen and Jerôme Garot. *Automated, accurate and fast segmentation of 4D cardiac MR images.* In Functional Imaging and Modeling of the Heart, pages 474–483. Springer, 2007.

[Currie 2011] S. Currie, K. Mankad and A. Goddard. *Endovascular treatment of intracranial aneurysms: review of current practice.* Postgraduate medical journal, vol. 87, no. 1023, pages 41–50, 2011.

[De Bruijne 2003] M. De Bruijne, B. Van Ginneken, W.J. Niessen, M. Loog and M.A. Viergever. *Model-based segmentation of abdominal aortic aneurysms*

in CTA images. In Proceedings of SPIE, volume 5032, pages 1560–1571. Citeseer, 2003.

[Dehmeshki 2009] J. Dehmeshki, H. Amin, M. Ebadian-Dehkordi, A. Jouannic and S. Qanadli. *Computer aided detection and measurement of abdominal aortic aneurysm using computed tomography digital images.* In Digital Society, 2009. ICDS'09. Third International Conference on, pages 339–342. IEEE, 2009.

[Delgado-Gonzalo 2012] R. Delgado-Gonzalo, P. Thevenaz, C.S. Seelamantula and M. Unser. *Snakes With an Ellipse-Reproducing Property.* Image Processing, IEEE Transactions on, vol. 21, no. 3, pages 1258–1271, 2012.

[Dervieux 1980] Alain Dervieux and François Thomasset. *A finite element method for the simulation of a Rayleigh-Taylor instability.* In Approximation methods for Navier-Stokes problems, pages 145–158. Springer, 1980.

[Dice 1945] Lee R Dice. *Measures of the amount of ecologic association between species.* Ecology, vol. 26, no. 3, pages 297–302, 1945.

[Egmont-Petersen 2002] Michael Egmont-Petersen, Dick de Ridder and Heinz Handels. *Image processing with neural networks—a review.* Pattern recognition, vol. 35, no. 10, pages 2279–2301, 2002.

[Firouzian 2011] A. Firouzian, R. Manniesing, Z.H. Flach, R. Risselada, F. van Kooten, M.C.J.M. Sturkenboom, A. van der Lugt and W.J. Niessen. *Intracranial aneurysm segmentation in 3D CT angiography: Method and quantitative validation with and without prior noise filtering.* European journal of radiology, vol. 79, no. 2, pages 299–304, 2011.

[Firouzian 2013] Azadeh Firouzian, Rashindra Manniesing, Coert T Metz, Roelof Risselada, Stefan Klein, Fop van Kooten, Miriam CJM Sturkenboom, Aad van der Lugt and Wiro J Niessen. *Quantification of intracranial aneurysm morphodynamics from ECG-gated CT angiography.* Academic radiology, vol. 20, no. 1, pages 52–58, 2013.

[Frisch 1986] Uriel Frisch, Brosl Hasslacher and Yves Pomeau. *Lattice-gas automata for the Navier-Stokes equation.* Physical review letters, vol. 56, pages 1505–1508, 1986.

[Hardy 1973] J Hardy, Yv Pomeau and O De Pazzis. *Time evolution of a two-dimensional classical lattice system.* Physical Review Letters, vol. 31, no. 5, page 276, 1973.

[Hentschke 2012] Clemens M Hentschke, Oliver Beuing, Rosa Nickl and Klaus D Tönnies. *Detection of cerebral aneurysms in MRA, CTA and 3D-RA data sets.* In SPIE Medical Imaging, pages 83151I–83151I. International Society for Optics and Photonics, 2012.

[Hernandez 2003] M. Hernandez, A. Frangi and G. Sapiro. *Three-dimensional segmentation of brain aneurysms in CTA using non-parametric region-based information and implicit deformable models: Method and evaluation.* Medical Image Computing and Computer-Assisted Intervention-MICCAI 2003, pages 594–602, 2003.

[Hernandez 2007] Monica Hernandez and Alejandro F Frangi. *Non-parametric geodesic active regions: method and evaluation for cerebral aneurysms segmentation in 3DRA and CTA.* Medical image analysis, vol. 11, no. 3, pages 224–241, 2007.

[Hochmuth 2002] Albrecht Hochmuth, Uwe Spetzger and Martin Schumacher. *Comparison of three-dimensional rotational angiography with digital subtraction angiography in the assessment of ruptured cerebral aneurysms.* American journal of neuroradiology, vol. 23, no. 7, pages 1199–1205, 2002.

[Hojjatoleslami 1998] SA Hojjatoleslami and Josef Kittler. *Region growing: a new approach.* IEEE Transactions on Image processing, vol. 7, no. 7, pages 1079–1084, 1998.

[Hop 1997] J.W. Hop, G.J.E. Rinkel, A. Algra and J. van Gijn. *Case-fatality rates and functional outcome after subarachnoid hemorrhage: a systematic review.* Stroke, vol. 28, no. 3, pages 660–664, 1997.

[Hoskins 1998] PR Hoskins, J Prattis and J Wardlaw. *A flow model of cerebral aneurysms for use with power Doppler studies.* The British journal of radiology, vol. 71, no. 841, pages 76–80, 1998.

[Jawerth 1999] B. Jawerth, P. Lin and E. Sinzinger. *Lattice Boltzmann models for anisotropic diffusion of images.* Journal of Mathematical Imaging and Vision, vol. 11, no. 3, pages 231–237, 1999.

[Karmonik 2010] C Karmonik, O Diaz, R Grossman and R Klucznik. *In-vivo quantification of wall motion in cerebral aneurysms from 2D cine phase contrast magnetic resonance images.* Rofo, vol. 182, no. 2, page 140, 2010.

[Kass 1988] M. Kass, A. Witkin and D. Terzopoulos. *Snakes: Active contour models.* International journal of computer vision, vol. 1, no. 4, pages 321–331, 1988.

[Kato 2004] Y Kato, M Hayakawa, H Sano, MV Sunil, S Imizu, M Yoneda, S Watanabe, M Abe and T Kanno. *Prediction of impending rupture in aneurysms using 4D-CTA: Histopathological verification of a real-time minimally invasive tool in unruptured aneurysms.* min-Minimally Invasive Neurosurgery, vol. 47, no. 03, pages 131–135, 2004.

[Kostopoulos 2007] S. Kostopoulos, D. Glotsos, GC Kagadis, A. Daskalakis, P. Spyridonos, I. Kalatzis, M. Karamessini, T. Petsas, D. Cavouras and G. Nikiforidis. *A hybrid pixel-based classification method for blood vessel segmentation and aneurysm detection on CTA.* Computers & Graphics, vol. 31, no. 3, pages 493–500, 2007.

[Lauric 2010] A. Lauric, E. Miller, S. Frisken and A.M. Malek. *Automated detection of intracranial aneurysms based on parent vessel 3D analysis.* Medical image analysis, vol. 14, no. 2, pages 149–159, 2010.

[Law 2007] Max WK Law and Albert CS Chung. *Vessel and intracranial aneurysm segmentation using multi-range filters and local variances.* In Medical Image Computing and Computer-Assisted Intervention–MICCAI 2007, pages 866–874. Springer, 2007.

[Lesage 2009] D. Lesage, E.D. Angelini, I. Bloch and G. Funka-Lea. *A review of 3D vessel lumen segmentation techniques: Models, features and extraction schemes.* Medical Image Analysis, vol. 13, no. 6, pages 819–845, 2009.

[Li 1995] Stan Z Li. Markov random field modeling in computer vision. Springer-Verlag New York, Inc., 1995.

[Li 2010] Chunming Li, Chenyang Xu, Changfeng Gui and Martin D Fox. *Distance regularized level set evolution and its application to image segmentation.* Image Processing, IEEE Transactions on, vol. 19, no. 12, pages 3243–3254, 2010.

[McNamara 1988] Guy R McNamara and Gianluigi Zanetti. *Use of the Boltzmann equation to simulate lattice-gas automata.* Physical Review Letters, vol. 61, no. 20, page 2332, 1988.

[Montagnat 2003] Johan Montagnat, Maxime Sermesant, Hervé Delingette, Grégoire Malandain and Nicholas Ayache. *Anisotropic filtering for model-based segmentation of 4D cylindrical echocardiographic images.* Pattern Recognition Letters, vol. 24, no. 4, pages 815–828, 2003.

[Montagnat 2005] Johan Montagnat and Hervé Delingette. *4D deformable models with temporal constraints: application to 4D cardiac image segmentation.* Medical Image Analysis, vol. 9, no. 1, pages 87–100, 2005.

[Olabarriaga 2004] S. Olabarriaga, M. Breeuwer and W. Niessen. *Segmentation of abdominal aortic aneurysms with a non-parametric appearance model.* Computer Vision and Mathematical Methods in Medical and Biomedical Image Analysis, pages 257–268, 2004.

[Osher 1988] S. Osher and J.A. Sethian. *Fronts propagating with curvature-dependent speed: algorithms based on Hamilton-Jacobi formulations.* Journal of computational physics, vol. 79, no. 1, pages 12–49, 1988.

[Otsu 1975] N. Otsu. *A threshold selection method from gray-level histograms.* Automatica, vol. 11, no. 285-296, pages 23–27, 1975.

[Oubel 2010] E Oubel, JR Cebral, Mathieu De Craene, R Blanc, Jordi Blasco, J Macho, CM Putman and AF Frangi. *Wall motion estimation in intracranial aneurysms.* Physiological measurement, vol. 31, no. 9, page 1119, 2010.

[Pal 1993] Nikhil R Pal and Sankar K Pal. *A review on image segmentation techniques.* Pattern recognition, vol. 26, no. 9, pages 1277–1294, 1993.

[Petitjean 2011] Caroline Petitjean and Jean-Nicolas Dacher. *A review of segmentation methods in short axis cardiac MR images.* Medical image analysis, vol. 15, no. 2, pages 169–184, 2011.

[Pham 2000] Dzung L Pham, Chenyang Xu and Jerry L Prince. *Current methods in medical image segmentation 1.* Annual review of biomedical engineering, vol. 2, no. 1, pages 315–337, 2000.

[Rinkel 1998] Gabriel JE Rinkel, Mamuka Djibuti, Ale Algra and J Van Gijn. *Prevalence and risk of rupture of intracranial aneurysms a systematic review.* Stroke, vol. 29, no. 1, pages 251–256, 1998.

[Sahoo 1988] Prasanna K Sahoo, SAKC Soltani and AKC Wong. *A survey of thresholding techniques.* Computer vision, graphics, and image processing, vol. 41, no. 2, pages 233–260, 1988.

[Seibert 2011] Brad Seibert, Ramachandra P Tummala, Ricky Chow, Alireza Faridar, Seyed A Mousavi and Afshin A Divani. *Intracranial aneurysms: review of current treatment options and outcomes.* Frontiers in neurology, vol. 2, 2011.

[Tortora 1976] Gerard J Tortora and Nicholas Peter Anagnostakos. *Principles of anatomy and physiology.* 1976.

[Ujiie 1999] Hiroshi Ujiie, Hiroyuki Tachibana, Osamu Hiramatsu, Andrew L Hazel, Takeshi Matsumoto, Yasuo Ogasawara, Hiroshi Nakajima, Tomokatsu Hori, Kintomo Takakura and Fumihiko Kajiya. *Effects of size and shape (aspect ratio) on the hemodynamics of saccular aneurysms: a possible index for surgical treatment of intracranial aneurysms.* Neurosurgery, vol. 45, no. 1, page 119, 1999.

[Vega 2002] C. Vega, J.V. Kwoon, S.D. Lavine*et al. Intracranial aneurysms: current evidence and clinical practice.* American family physician, vol. 66, no. 4, pages 601–610, 2002.

[Wang 2011] Y. Wang, G. Courbebaisse and Y.M. Zhu. *Segmentation of giant cerebral aneurysms using a multilevel object detection scheme based on lattice Boltzmann method.* In Signal Processing, Communications and Computing (ICSPCC), 2011 IEEE International Conference on, pages 1–4. IEEE, 2011.

[Wardlaw 1996] Joanna M Wardlaw and James C Cannon. *Color transcranial "power" Doppler ultrasound of intracranial aneurysms.* Journal of neurosurgery, vol. 84, no. 3, pages 459–461, 1996.

[Wiebers 2003] D.O. Wiebers. *Unruptured intracranial aneurysms: natural history, clinical outcome, and risks of surgical and endovascular treatment.* The Lancet, vol. 362, no. 9378, pages 103–110, 2003.

[Wilson 1999] Dale L. Wilson and J. Alison Noble. *An adaptive segmentation algorithm for time-of-flight MRA data.* Medical Imaging, IEEE Transactions on, vol. 18, no. 10, pages 938–945, 1999.

[Wolf-Gladrow 1995] D. Wolf-Gladrow. *A lattice Boltzmann equation for diffusion.* Journal of statistical physics, vol. 79, no. 5, pages 1023–1032, 1995.

[Wolf-Gladrow 2000] Dieter A Wolf-Gladrow. Lattice-gas cellular automata and lattice boltzmann models: An introduction. Numeéro 1725. Springer, 2000.

[Y.Chen 2009] Y.Chen. *Lattice Boltzmann Method Based Medical Image Segmentation.* In Image and Signal Processing, 2009 IEEE International Conference on, pages 1–5. IEEE, 2009.

[Yoon 2007] DY Yoon, KJ Lim, CS Choi, BM Cho, SM Oh and SK Chang. *Detection and characterization of intracranial aneurysms with 16-channel multidetector row CT angiography: a prospective comparison of volume-rendered images and digital subtraction angiography.* American journal of neuroradiology, vol. 28, no. 1, pages 60–67, 2007.

[Zhang 2001] Yu Jin Zhang. *A review of recent evaluation methods for image segmentation.* In Signal Processing and its Applications, Sixth International, Symposium on. 2001, volume 1, pages 148–151. IEEE, 2001.

[Zhang 2011] Chong Zhang, Maria-Cruz Villa-Uriol, Mathieu De Craene, José María Pozo, Juan M Macho and Alejandro F Frangi. *Dynamic estimation of three-dimensional cerebrovascular deformation from rotational angiography.* Medical physics, vol. 38, no. 3, pages 1294–1306, 2011.

[Zhang 2012] Hong Zhang, Yuanfeng Jiao, Yongjie Zhang and Kenji Shimada. *Automated segmentation of cerebral aneurysms based on conditional random field and gentle adaboost.* In Mesh Processing in Medical Image Analysis 2012, pages 59–69. Springer, 2012.

[Zhao 2008] Y. Zhao. *Lattice Boltzmann based PDE solver on the GPU.* The Visual Computer, vol. 24, no. 5, pages 323–333, 2008.

[Zhao 2009] Fei Zhao, Honghai Zhang, Andreas Wahle, Matthew T Thomas, Alan H Stolpen, Thomas D Scholz and Milan Sonka. *Congenital aortic disease: 4D magnetic resonance segmentation and quantitative analysis.* Medical image analysis, vol. 13, no. 3, pages 483–493, 2009.

[Zohios 2012] Christos Zohios, Georgios Kossioris and Yannis Papaharilaou. *Geometrical methods for level set based abdominal aortic aneurysm thrombus and outer wall 2D image segmentation.* Computer methods and programs in biomedicine, vol. 107, no. 2, pages 202–217, 2012.

FOLIO ADMINISTRATIF

THESE SOUTENUE DEVANT L'INSTITUT NATIONAL DES SCIENCES APPLIQUEES DE LYON

NOM : WANG **DATE de SOUTENANCE :** 25/07/2014

Prénom : Yan

TITRE : Etude de la method de Boltzmann sur réseau pour la segmentation d'anévrismes cérébraux

NATURE : Doctorat **Numéro d'ordre :**

École doctorale : École Doctorale Électronique, Électrotechnique, Automatique

Spécialité : Image et System

RESUME :

L'anévrisme cérébral est une région fragile de la paroi d'un vaisseau sanguin dans le cerveau, qui peut se rompre et provoquer des saignements importants et des accidents vasculaires cérébraux. La segmentation de l'anévrisme cérébral est une étape primordiale pour l'aide au diagnostic, le traitement et la planification chirurgicale. Malheureusement, la segmentation manuelle prend encore une part importante dans l'angiographie clinique et elle est devenue couteuse en temps de traitement étant donné la gigantesque quantité de données générées par les systèmes d'imagerie médicale. Les méthodes de segmentation automatique d'image constituent un moyen essentiel pour faciliter et accélérer l'examen clinique et pour réduire l'interaction manuelle et la variabilité inter-opérateurs.

L'objectif principal de ce travail de thèse est de développer des méthodes automatiques pour la segmentation et la mesure des anévrismes. Le présent travail de thèse est constitué de trois parties principales. La première partie concerne la segmentation des anévrismes géants qui contiennent à la fois la lumière et le thrombus. La méthode consiste d'abord à extraire la lumière et le thrombus en utilisant une procédure en deux étapes, puis à affiner la forme du thrombus à l'aide de la méthode des courbes de niveaux. Dans cette partie, la méthode proposée est également comparée à la segmentation manuelle, démontrant sa bonne précision. La deuxième partie concerne une approche LBM pour la segmentation des vaisseaux dans des images 2D+t et de l'anévrisme cérébral dans les images en 3D. La dernière partie étudie un modèle de segmentation 4D en considérant les images 3D+t comme un hypervolume 4D et en utilisant un réseau LBM D4Q81, dans lequel le temps est considéré de la même manière que les trois autres dimensions pour la définition des directions de mouvement des particules dans la LBM, considérant les données 3D+t comme un hypervolume 4D et en utilisant un réseau LBM D4Q81. Des expériences sont réalisées sur des images synthétiques d'hypercube 4D et d'hypersphere 4D. La valeur de Dice sur l'image de l'hypercube avec et sans bruit montre que la méthode proposée est prometteuse pour la segmentation 4D et le débruitage.

MOTS-CLES :

Segmentation du thrombus, méthode de Boltzmann sur réseau, anévrisme cérébral, détection du mouvement, segmentation 4D.

Laboratoire (s) de recherche: Creatis (CNRS UMR 5520, INSERM U1044)

Directeur de thèse : COURBEBAISSE Guy

Président de jury :

Composition du jury : CHOPARD Bastien, THIRAN Jean-Philippe, BONAFE Alain, FOURNEL Thierry, CLARYSSE Patrick, COURBEBAISSE Guy, ZHU Yue-Min, NAVARRO Laurent.